Numerical modeling of solidification process during continuous casting including the effects of interface heat flux

by Nikhil Lingaji Gawas

A thesis submitted in partial fulfillment of the requirements for the degree of Master of Science in Mechanical Engineering

Montana State University

Abstract:

Multiphase fluid flow involving solidification is common in many industrial processes like extrusion, continuous casting, drawing, etc. Thus, thermal transport is significant in these cases. The present study concentrates on the study of air gap formation on the metal-mold interfacial heat transfer of a continuous casting mold. The numerical modeling of continuous casting has attained a sophisticated level by including other phenonmenon which take place during the process. Solidification models include metal-mold interfacial heat transfer, mold distortion, macrosegregation, turbulence and argon gas injection to name a few.

The present method takes into account the shrinkage of the metal when it undergoes cooling in the metal mold by losing latent heat as well as sensible heat. The formulation for the air gap formation was assumed one-dimensional with conduction as the only mode of transfer in the air gap. The metal-mold interfacial air gap was converted into an effective heat resistance which is incorporated on the outer surface of the mold by changing the convective heat transfer coefficient.

Initially, an algorithm was developed and validated to simulate the basic process. This algorithm was modified to include the effect of air gap based on the shrinkage formulation. The parameters were studied to comprehend the effect of air gap heat resistance on different aspects of the process. Basic process variables were the superheat temperature or the inlet temperature, withdrawal velocity and the mold/post mold cooling rates. The results were non-dimensionalized to generalize them for comparison. Results were plotted in terms of solidification front, average and local heat flux, mold wall temperature, centerline temperature, velocity vector and fractional heat extracted in the mold.

A few cases were also run with and without air gap modeling and their results compared. It was noted that a small value of air gap width significantly affected the heat transfer. The air gap width was critical, as in some cases the gap was too small to affect the total heat flux. The current study shows that there exists a limiting value of withdrawal speed (Pe) and superheat ($\theta 0$) above which the effect of air gap formation on the overall heat transfer is negligible. A critical value of mold cooling rate (Bi2) also exists for a given set of parameters, which gives the maximum heat extraction rate. The effect of post mold cooling rate (Bi3) on the overall heat transfer was negligible.

NUMERICAL MODELING OF SOLIDIFICATION PROCESS DURING CONTINUOUS CASTING INCLUDING THE EFFECTS OF INTERFACE HEAT FLUX

by

Nikhil Lingaji Gawas

A thesis submitted in partial fulfillment
of the requirements for the degree

of

Master of Science

in

Mechanical Engineering

MONTANA STATE UNIVERSITY
Bozeman, Montana

March 2001

APPROVAL

of a thesis submitted by

Nikhil Gawas

This thesis has been read by each member of the thesis committee and has been found to be satisfactory regarding content, English usage, format, citations, bibliographic style, and consistency, and is ready for submission to the College of Graduate Studies.

Dr. Ruhul Amin _____ (Signature) 8 March 2001 Date

Approved for the Department of Mechanical and Industrial Engineering

Dr. Vic Cundy _____ (Signature) 3/9/01 Date

Approved for the College of Graduate Studies

Dr. Bruce R. McLeod _____ (Signature) 3-9-01 Date

STATEMENT OF PERMISSION TO USE

In presenting this thesis in partial fulfillment of the requirements for a master's degree at Montana State University, I agree that the Library shall make it available to borrowers under rules of the Library.

If I have indicated my intention to copyright this thesis by including a copyright notice page, copying is allowable only for scholarly purposes, consistent with "fair use" as prescribed in the U.S. Copyright Law. Requests for permission for extended quotation from or reproduction of this thesis in whole or in parts may be granted only by the copyright holder.

Signature N Gavras

Date March 09, 2001

ACKNOWLEDGMENTS

I would like to thank Dr. Ruhul Amin for his guidance in my research and thesis work. I would also like to thank Dr. Alan George and Dr. Thomas Reihman for their work as committee members.

Dr. Ladean McKittrick deserves a special mention for helping me out with the computing resources. I also appreciate the Department of Mechanical and Industrial Engineering and my parents for providing me with financial assistance.

Finally, my appreciation goes out to all the staff of the Department of Mechanical and Industrial Engineering and my fellow graduate students for their continued support.

TABLE OF CONTENTS

TABLE OF CONTENTS - Continued

LIST OF TABLES

LIST OF FIGURES

LIST OF FIGURES – continued

LIST OF FIGURES – continued

LIST OF FIGURES – continued

LIST OF FIGURES – continued

NOMENCLATURE

Symbol	Description
Ar	Aspect ratio of cast material, L / W
Bi	Biot number
Bi_1	Pre-mold region Biot number
Bi_2	Mold Biot number $= h_2 W / k_{Cu}$
Bi_3	Post-mold Biot number $= h_3 W / k_{Cu}$
C	Specific heat
C_ϕ	Diffusion coefficient
g	constant of gravity.
h	Heat transfer coefficient
h_2	Dimensional mold convective heat transfer coefficient
h_3	Dimensional post-mold convective heat transfer coefficient
H^*	Non-dimensional effective heat transfer coefficient
H_{eff}	Effective heat transfer coefficient
k	Thermal conductivity
L	Length of the cast material
L_h	Latent heat of fusion
L_1	Length of pre-mold region
L_2	Length of mold region
L_3	Length of post-mold region
P	Pressure

NOMENCLATURE – continued

Pe	Peclet number = U_0W / α_s
q	Local heat flux
q^*	Non-dimensional local heat flux
Q^*	Average dimensionless heat flux
R	Resistance
r^2	Variance of data
Ste	Stefan number = $C_s (T-T_\infty) / L_h$
t	time
t_m	thickness of the copper mold
T	Temperature
T_0	Temperature at the inlet
T_s	Solidification temperature of Aluminum
T_∞	Ambient temperature
U_0	Withdrawal speed.
V_x	X component of velocity
V_y	Y component of velocity
W	Half thickness of the cast material
W^e	Weighting function
X_{gap}	Air gap width

Greek Symbols

α	Thermal diffusivity (also coefficient of linear expansion where stated)

NOMENCLATURE – continued

β	Coefficient of volumetric expansion
δ	Dirac-delta-function (also temperature difference wherever mentioned)
μ	Dynamic viscosity
ρ	Density
θ	Non-dimensional temperature = $(T-T_\infty)/(T_s - T_\infty)$
ϕ	Degree of freedom variable (DOF)
Γ	Diffussion Coefficient
τ	Stress tensor
λ	Second coefficient of viscosity
Δ	Mathematical operator for difference

Subscripts and Superscripts

avg	Average value
Al	Aluminum
Cu	Copper
d	downwind nodes
e	element property
eff	effective value
gap	air gap property
l	liquid phase
m	mold property
s	solid property

NOMENCLATURE – continued

u	upwind nodes
0	condition at the inlet

Ansys commands nomenclature

FLDATA	Specifies various fluid properties
MAT	Specifies material properties
MP	Specifies material properties table
MPDATA	Specifies data for material properties table
KEYOPT(1)	Activates multiple species transport
KEYOPT(3)	Specifies the coordinate system

ABSTRACT

Multiphase fluid flow involving solidification is common in many industrial processes like extrusion, continuous casting, drawing, etc. Thus, thermal transport is significant in these cases. The present study concentrates on the study of air gap formation on the metal-mold interfacial heat transfer of a continuous casting mold. The numerical modeling of continuous casting has attained a sophisticated level by including other phenonmenon which take place during the process. Solidification models include metal-mold interfacial heat transfer, mold distortion, macrosegregation, turbulence and argon gas injection to name a few.

The present method takes into account the shrinkage of the metal when it undergoes cooling in the metal mold by losing latent heat as well as sensible heat. The formulation for the air gap formation was assumed one-dimensional with conduction as the only mode of transfer in the air gap. The metal-mold interfacial air gap was converted into an effective heat resistance which is incorporated on the outer surface of the mold by changing the convective heat transfer coefficient.

Initially, an algorithm was developed and validated to simulate the basic process. This algorithm was modified to include the effect of air gap based on the shrinkage formulation. The parameters were studied to comprehend the effect of air gap heat resistance on different aspects of the process. Basic process variables were the superheat temperature or the inlet temperature, withdrawal velocity and the mold/post mold cooling rates. The results were non-dimensionalized to generalize them for comparison. Results were plotted in terms of solidification front, average and local heat flux, mold wall temperature, centerline temperature, velocity vector and fractional heat extracted in the mold.

A few cases were also run with and without air gap modeling and their results compared. It was noted that a small value of air gap width significantly affected the heat transfer. The air gap width was critical, as in some cases the gap was too small to affect the total heat flux. The current study shows that there exists a limiting value of withdrawal speed (Pe) and superheat (θ_0) above which the effect of air gap formation on the overall heat transfer is negligible. A critical value of mold cooling rate (Bi_2) also exists for a given set of parameters, which gives the maximum heat extraction rate. The effect of post mold cooling rate (Bi_3) on the overall heat transfer was negligible.

CHAPTER 1

INTRODUCTION

Thermal transport phenomenon plays an important role in engineering applications especially in manufacturing processes such as continuous casting, optical fiber drawing, hot rolling and metal wire drawing.

Continuous casting is a rapidly developing field and has gained prime importance in the manufacturing of ferrous and non-ferrous slabs. A substantial amount of steel produced every year is by way of continuous casting. Figure 1 shows a typical setup of a continuous casting mill.

Superheated metal enters a metal mold, which is open ended, via a tundish and a nozzle. The metal is cooled due to heat exchange with the mold, which is water-cooled. As the metal shell forms, it is continuously withdrawn from the exit of the mold with the help of pinch rollers. Lubrication is provided with the help of mold flux, which prevents the liquid metal from sticking to the mold wall. On exit, the metal shell is subjected to spray cooling before finally being cut off by a gas torch.

Serious problems are encountered during continuous casting if the process parameters are not carefully monitored and controlled. The heat extraction rate and the withdrawal speed are particularly critical, for if they are not controlled, it can lead to breakout. Breakout is a serious condition where the metal shell formed cannot withstand the ferrostatic pressure of the liquid core, and due to insufficient shell thickness, the solid metal breaks spilling out hot liquid metal. This leads to formidable damages and repairs. Other defects include air-gap formation at the metal-mold interface due to thermal

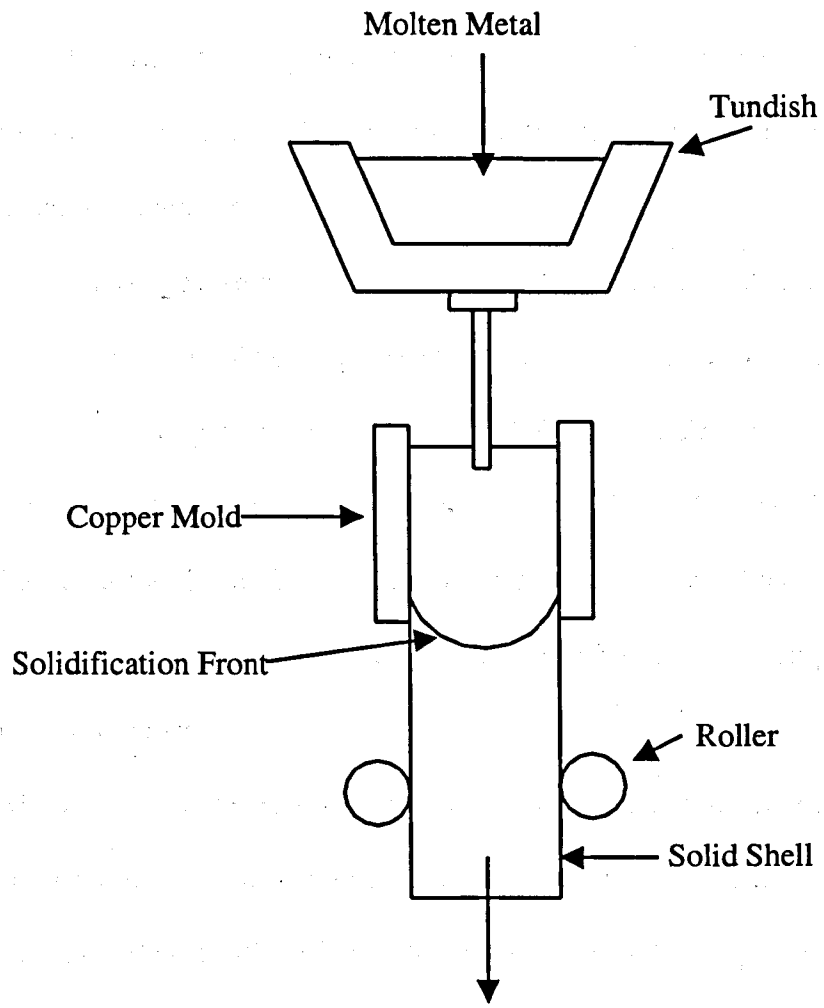

Figure 1. Continuous Casting Setup.

shrinkage, rhombodity and corner cracks due to mold distortion as reported by Samarasekara and Brimacombe (1979,1984), residual stresses due to uneven cooling and surface depressions.

Motivation

Optimization and process control are of prime importance to reduce defects and increase productivity. Correspondingly, numerical modeling of continuous casting has received more attention, complemented by the fact that it is less expensive compared to experimental investigation.

Parameters governing the process need to be studied carefully in order to streamline the process. Typical parameters include superheat temperature, withdrawal velocity, mold cooling rate and post-mold cooling rate. Present research is primarily focused on the effects of air gap formation on the mold-metal interfacial heat transfer. Air gap at the metal-mold interface leads to decreased contact conductance, thus decreasing the overall effective heat transfer thereby leading to higher mold temperatures and lower heat transfer efficiency.

Mold heat transfer is governed by the size of the gap separating the solidifying shell from the wall of the cooling mold and the properties of the flux which infiltrates the gap. Biloni and Prates (1977) have shown that even when liquid metal makes contact with the mold wall, there is some contact resistance. Irwing (1967) has studied interfacial heat transfer in the case of ingot molds. He has seen that for air gap values up to 100μm, heat transfer takes place mainly due to conduction through air and radiation was negligible. For air gaps above 100μm, radiation becomes appreciable only when casting surface temperatures are above 800°C. The gap width and mold heat extraction are also dependent on the characteristics of the oscillation marks present on the slab surface. An

oscillation mark locally increases the gap, reduces heat transfer to the mold, and retards shell growth. Deep oscillation marks can be deleterious for surface quality because they are frequently the site of transverse cracks. Thus, understanding interfacial heat transfer is highly desirable in the event of air-gap formation.

It is important to predict quantitatively and understand qualitatively various phenomena involved in continuous casting process. Air gap formation is a hindrance to the process and understanding how and where it forms is an important step towards its prevention. Although information is available on the metal-mold interface heat transfer for metal ingot castings, hardly any data could be found regarding the same in continuous castings for pure metals. Hence, aluminum was chosen for modeling, although steel remains the major material manufactured by continuous casting process.

Background

Numerical modeling of thermo-fluid applications has been in the cynosure due to rapid development in computing. Faster computing and large memory space gives an opportunity to do analyses previously thought to be time consuming and practically impossible. Finite difference methods, finite volume methods and finite element methods are commonly used to tackle any computational fluid dynamics (CFD) problem.

Phase change problems are highly non-linear due to the presence of a boundary (solidification front) across which the properties vary like Dirac-δ-type behavior (especially for pure substances). The class of problems usually referred to as 'isothermal phase change' problems pose greater computational difficulties. In such problems, the numerical simulations for the temperature history and/or the location of the solidification front result in some sort of overprediction / underprediction as well as numerical oscillations about the true response as pointed out by Namburu and Tamma (1990). Finite difference methods were traditionally employed for analyzing the phase change problems. Currently, numerical analysts are focusing more on finite element analysis (FEA) due to their inherent advantages in handling the evolution of latent heat. By employing finite elements in conjunction with numerical integration, a reasonable accuracy can be obtained for sufficiently smooth variations of the effective heat transfer capacity as reported by Namburu and Tamma (1990). In this research the enthalpy method has been employed and will be discussed in the following chapters.

Numerical modeling of continuous casting dates back almost five decades. Many researchers have contributed to the mathematical modeling of continuous casting process. Primarily two approaches have been adopted to solve this problem numerically; one is the moving grid technique and the second is the fixed grid technique. The fixed grid technique handles the latent heat evolution by introducing non-linearities in the specific heat or enthalpy of the material, whereas, the moving grid technique involves the change of grid points with time.

Jaluria (1992) has presented detailed work on the thermal transport of continuously moving material. The work was focused on the conjugate problem of heat transfer and fluid flow in moving material. Boundary layer formulation and the solution to the full governing equations were devised. Several other phenomena like thermal buoyancy, transient effects and forced flow were also considered. The results were generalized and interpreted for various thermal transport processes like extrusion, fiber drawing, electric furnace heating, thermal processing of glass and continuous casting.

Kang and Jaluria (1993) have developed a thermal model of the continuous casting process. One-dimensional three-zone model and two-dimensional enthalpy model were presented. The one-dimensional model was fairly idealized and can be used for the validation of multi-dimensional models that may be employed for more complicated situations. The enthalpy model solved the equations by finite difference methods using the alternating direction implicit (ADI) scheme. It was shown that varying the governing parameters could control the shape of the solidification front. Results followed the

expected trend of the process. (i.e. the solidification front moved downstream as superheat / withdrawal speed was increased or as the cooling rates were decreased.)

Choudary and Mazumdar (1994) proposed a steady state, two-dimensional model for continuous casting. The model also included turbulence, fluid flow and thermal transport within the mushy zone and the bulk motion of the descending strand on liquid steel. The mushy zone was modeled considering the enhanced resistance offered by the dendrites by increasing the viscosity of the liquid steel. A constant apparent viscosity equal to twenty times the molecular viscosity of steel was taken. The numerical scheme employed a control volume based finite difference procedure and incorporated the SIMPLE algorithm of Patankar and Spalding (1972). The numerical results were compared with three different billet-casting operations. Shell thickness values were in good agreement with the experimental data. The comparison of results also displayed the inadequacy of the effective thermal conductivity model presented by Choudary et al. (1993).

Simulation of solidification in continuous casting of steel billets using the non-linear heat conduction equation was presented by Vanaparthy and Srinivasan (1994). A numerical method was used which employed the two-time level Crank Nicholson scheme to start the simulation, whereas Gauss-integration was used to compute the element matrices numerically. The initial conditions provided the values for generating temperatures for the first time step. The model calculated the solid shell temperatures in a transverse cross section of the billet at discrete time intervals. The influence of spray

water flux (post-mold cooling) on the amount of reheat at the corner of the billet was particularly interesting. It was shown that reheating could be minimized by decreasing the amount of water gradually from 170 GPM to 50 GPM for the given set of process parameters.

Thomas et al. (1990, 1996) investigated the effect of superheat on the fluid flow and temperature distribution in a continuous slab-casting process. The models developed included two-dimensional as well as three-dimensional domains. The solidification model was not coupled with the fluid flow and heat transfer within the caster. Instead, the velocity vector field and the temperature distribution was first obtained and then the heat flux at the wall was used in the one-dimensional solidification model to give the growth rate of the solidifying shell.

Seyedein and Hasan (1997) have presented a comprehensive three-dimensional model which couples turbulent flow and macroscopic solidification heat transfer for a continuous slab caster. The turbulence modeling involved the implementation of the standard two-equation k-ε model whereas solidification was formulated using the enthalpy method. The mushy zone was accounted for by applying the D'arcy laws for a porous media. An important conclusion drawn was that, due to wide variations of turbulent viscosity within the caster, the approach of applying an artificially enhanced melt viscosity was not acceptable. It was also found that the inlet superheat has minimal effect on the growth rate of the solid shell and the mushy zone except for the vicinity of the jet impingement region.

As our understanding of the continuous casting process increases, mathematical models are becoming more sophisticated so more of the known phenomenon can be included in the models. Various process defects have been implemented in conjunction with the basic models as well as other complex models to simulate the process aptly.

Royzman (1997) has studied the friction between strand and mold during continuous casting. He developed a mathematical model to compute the friction coefficient between the slab and the mold based on the process parameters and the properties of the mold lubricating powder in liquid and solid states. It was found that the coefficient of friction increases with an increase in casting speed whereas it decreases with increase in the mold oscillation frequency and the depth of the liquid slag layer. The atomic mass of the lubricating powder was found to have profound effect on the mold friction. Smaller atomic mass of the powder lead to lower frictional resistance.

Nakato et al. (1984) investigated the formation of shell and longitudinal cracks in mold during high speed continuous casting of slabs. The probability of occurrence of breakout as well as surface defects is high in the case of high speed casting as more liquid is flowing through the core of the solid shell. Extensive experimentation was carried out and the results were interpreted to countermeasure the formation of cracks. The measured shell profiles and those calculated mathematically were found to be in good agreement. Casting speed and powder properties had the greatest influence on the mean heat flux in the mold.

One of the significant defects that have been addressed is the air gap formation at the metal mold interface. Metal shrinkage leads to the development of an air gap at the metal mold interface leading to a considerable decrease in the heat transfer. Many researchers have attempted to characterize this phenomenon. Application of inverse techniques was one of the common methods used to quantify the contact conductance. Inverse techniques are usually used where the temperature profile is known and it is used to back calculate the heat transfer coefficient. Brimacombe et al. (1992) have used a sequential algorithm for the solution of inverse heat conduction problem (IHCP) to determine the response of both the surface heat flux and the surface temperature of flat stainless steel samples subjected to water quenching under controlled laboratory conditions that ensured one-dimensional flow.

Mechanism of heat transfer at a metal mold interface was studied by Ho and Pehlke (1984) for ingot casting. They reported that as solidification progressed the metal and mold may stay in contact along isolated asperities on the microscopically rough surfaces or an interfacial gap may gradually develop. Three different mechanisms were expected to affect the transition of a metal-mold solid contact to an interfacial gap, namely, surface interaction of the metal and the mold, transformation of metal and mold materials and effects of the geometry. A numerical procedure was also presented which was based on the non-linear technique of Beck (1970) and an implicit formulation of the enthalpy method. An implicit finite difference scheme was selected because of the absence of a stability limit in the choice of time steps. Ho and Pehlke (1985) have also

conducted experimental study of aluminum castings in metallic molds. It was demonstrated that the solidification time was highly sensitive to a change in interfacial thermal conductance in the case of metallic molds. In the case of sand castings, it was noted that the use of Chvorinov's rule [Ho and Pehlke (1985)] was an effective alternative to numerical simulation provided that the interfacial thermal conductance was sufficiently high.

Huang et al. (1992 a) presented the conjugate gradient method for the inverse solution to determine unknown contact conductance during metal casting. The advantage of the conjugate gradient method was that there was no need to assume a specific functional form over the specific domain. The method was found to be stable and converged over an order of magnitude faster than the least squares methods. An inverse analysis of heat conduction involving phase change was employed for accurate determination of air gap resistance from the transient temperature measurements taken inside the casting region and at the outer mold surface. The results showed that the method requires much less computer time than the least squares methods and was less sensitive to the measurement errors. In the function estimation approach considered, a total of 80 unknowns were estimated to establish the unknown functional form of contact conductance; whereas in the least squares method four parameters were used to represent the function.

Isaac et al. (1985) simulated the solidification of aluminum in cast iron mold using experimental values of air gap. The values of heat transfer coefficient at the casting

mold interface and at the outside mold surface were obtained from the simulation. Contact resistance, mold coating thickness and the actual air gap were the three factors considered in the calculation of heat transfer coefficient at the mold-casting interface. It was found that the value of heat transfer coefficient at the interface was not constant, but varies with time. It decreases as solidification proceeds. Also, the heat transfer due to radation contributed to about 5 percent while the rest was mainly by conduction.

Various types of one-dimensional techniques exist for estimating the size gap that forms at the interface. Droste et al. (1986) formulated a method based on the thermoelasticity equations. The temperature field and thermal expansion characteristics of the metal and mold surfaces in contact were used to calculate the displacements of both surfaces.

Commonly used expressions for evaluating the metal-mold heat transfer coefficient or the heat flux were compiled by Brimacombe et al. (1995), which are listed in Table 1. These expressions have been developed by various researchers listed in the aforementioned publication. Various factors involved in metal-mold interfacial heat transfer in a solidification problem have been considered in these expressions. Some of the common phenomena incorporated are conduction and / or radiation, transient effects and chill properties to name a few. Extensive information regarding the formulations could be found in the references listed by Brimacombe et al. (1995).

Most of the work done on interfacial heat transfer was found on ingot mold casting where the inverse problem solution was attempted. However, it provided the

necessary insight in model formulation in the present research. As pointed out by Thomas (1991), continuous casting poses a significant challenge in implementing inverse techniques as it is difficult to obtain the temperature distribution by experimentation due to shortcomings in controlling the operating variables independently.

Table 1. Expressions for evaluation of heat transfer coefficient and heat flux.

Expression for h	Remarks
$h = h_s + h_g + h_r$	Conduction and radiation considered
$h = \dfrac{k_g}{(x_g + s_1 + s_2)}$	Only conduction is considered
$h = \dfrac{\sigma(T_c + T_m)(T_c^2 + T_m^2)}{\left(\dfrac{1}{\varepsilon_c} + \dfrac{1}{\varepsilon_m} - 1\right)}$	Only radiation is considered
$h = \dfrac{h'}{2\sqrt{t}}$	Transient case where interfacial gap forms
$h = a + bt$	Transient h where intimate contact at interface is enhanced
$h = \dfrac{k}{a}\left(\dfrac{r\sin\theta}{y} + \dfrac{a - \sin\theta}{y_f}\right) = \dfrac{k}{y_{eq}}$	Radiation is neglected
$q_{\max} = C_1(X_m / \alpha_m)^{n1}$	q_{max} depends on chill properties
$(q / q_{\max})\alpha_m^{0.05} = C_2 t^{n_2}$	q declines parabolically with time

Ho (1992) has characterized the metal mold interfacial heat transfer in continuous casting of slabs. A continuous casting model was formulated based on a spreadsheet program. This model was coupled with the interface model to integrate the phenomenon. A relationship characterizing the temperature dependency of mold flux viscosity was introduced and incorporated in the fluid flow equations for liquid mold flux. Also, the fluid flow equations coupled with heat transfer equations and a mass balance on the entire flux layer was solved to obtain the flux film thickness. The heat flux across the gap was then obtained from the flux film thickness.

Pioneering work in the field of continuous casting has been carried out by Samarasekara, Brimacombe (1991, 1992, 1995, 1996) and Thomas (1990, 1991, 1996) along with other researchers. Briamcombe et al. (1991) have determined axial heat flux profiles quantitatively from temperature measurements conducted on a slab mold under routine operating conditions. They have reported that the decline of heat flux below the meniscus was due to increase in resistance to heat flow across the gap and through the solidifying shell. The shell resistance was determined from the pool profile predicted with a one-dimensional solidification model using the heat flux values to characterize the surface boundary condition. The resistance of the gap was computed by considering the combined resistances of the shell, mold wall, and cooling water/mold wall interface.

Brimacombe et al. (1996) has proposed that the process of continuous casting should be explored through the development of advanced systems such as an 'intelligent

mold'. Brimacombe and coworkers conducted industrial trials by instrumenting the mold with thermocouples, load cells and differential transducers to investigate various aspects of the steel billet casting. The mold taper was found to have a significant effect on the heat transfer. Smaller tapers resulted in higher heat flux which was attributed to the fact that there was greater mechanical interaction between the mold and shell during the negative strip in the mold oscillating cycle.

Extensive research is being conducted at the Continuous Casting Consortium at the University of Illinois, Urbana-Champagne, lead by B. G. Thomas, in formulating sophisticated continuous casting models, which include mold distortion, interfacial heat transfer, macrosegregation, taper design, stress prediction, turbulence, etc.

Coupling sophisticated models to include various aspects of the process like turbulence, etc. in the basic formulation of continuous casting compromises the efficiency of the numerical study. Extensive studies have been conducted to include all kinds of process parameters but at the expense of computational time and space. Thus, the process of continuous casting entails efficient and simple models to simulate the phenomena realistically. Simplified formulations have to be explored and their results compared, to benchmark the adequacy of the models. Therefore, a simple one-dimensional conduction model was formulated in the present research for investigating the interfacial heat flux, which will be discussed in the following chapters. The two dimensional governing equations were solved using a finite element method.

CHAPTER 2

PROBLEM FORMULATION

Concept

In continuous casting process, molten metal enters a mold which is open ended and flows down the mold. The superheated metal is solidified as it flows downstream which is the effect of the mold and the post mold cooling. The copper mold is usually water-cooled whereas the post-mold cooling is done with water spraying. Solidified shell is continuously withdrawn from the exit of the mold. Hence we have a thermal transport from a continuously moving material. When the metal shell is formed, it shrinks due to phase change as well as subcooling. Metal shrinkage leads to an air gap at the metal-mold interface. This hampers the heat extraction efficiency of the mold.

Figure 2 shows the complete geometry of the mold with dimensional parameters. As stated earlier, aluminum was chosen for the cast material while copper was selected as the mold material. The pre-mold region was assumed to be insulated whereas the mold surface and the post mold region was subjected to convective heat transfer. Aluminum was modeled as Newtonian incompressible fluid with Boussinesque approximation. The fluid flow was assumed to be laminar and two-dimensional. The symmetry of the problem allowed for modeling half of the domain for computational purposes. The left half of the domain was modeled and a transient algorithm was used. The mold wall exit was taken as the origin. Hence the metal flows in the negative Y direction.

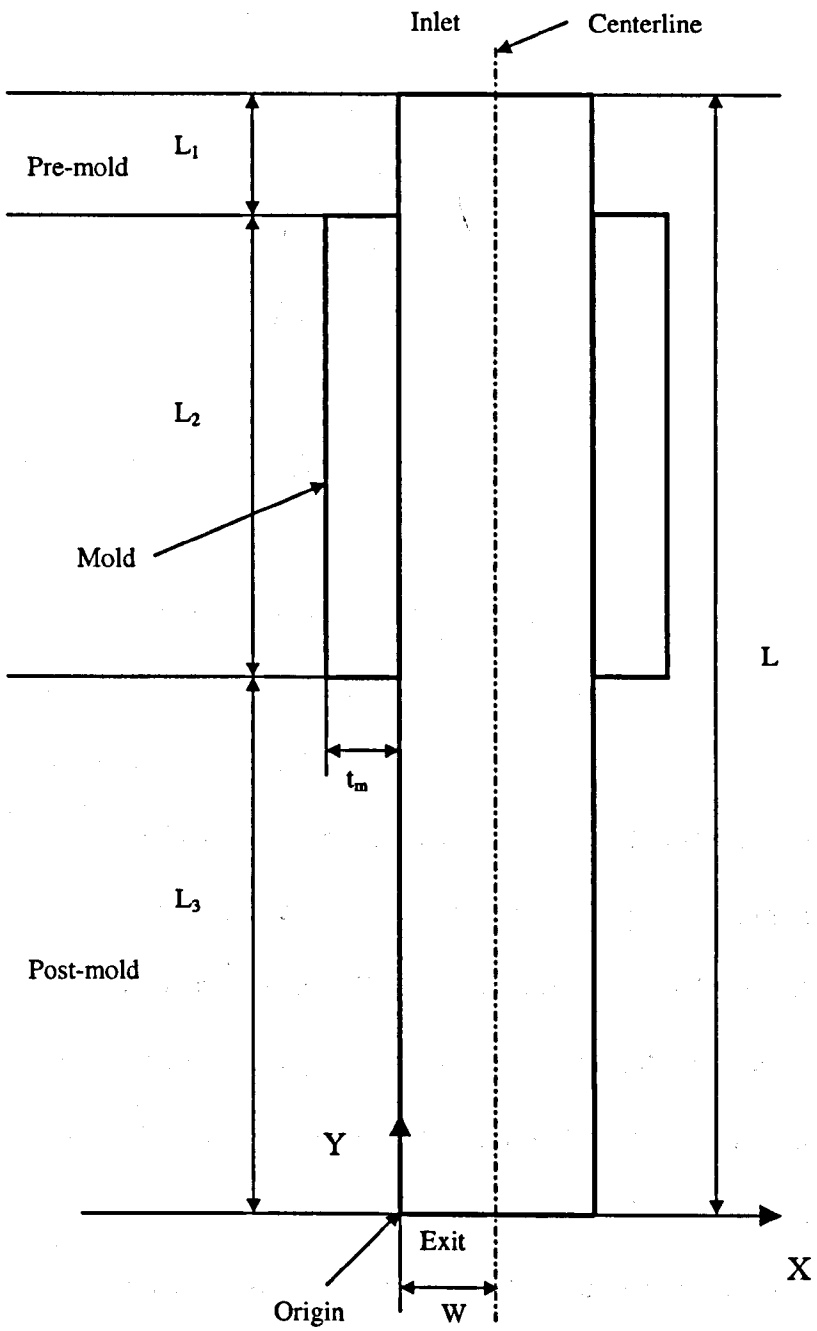

Figure 2. Problem domain in terms of dimensional parameters.

The aspect ratio is defined as:

$$Ar = L / W = 20 \tag{2.1}$$

Various mold parameters shown in Figure 2 are defined as follows:

$$L_3 / L = 0.5 \tag{2.2}$$

$$L_1 / L = 0.1 \tag{2.3}$$

$$t_m / W = 0.25 \tag{2.4}$$

where,

L_1 = length of the pre-mold region.

L_2 = length of the mold.

L_3 = length of the post mold or the secondary mold.

W = half width of the cast material.

t_m = thickness of the copper mold.

A commercial finite element code called Ansys (1999) was used for the numerical investigation. Although the code solves for a single-phase fluid, a user routine was developed to include multiphase fluid flow accompanied by solidification. The user routine was validated with analytical and experimental information to gain confidence in the method. The ultimate objective was to study the effect of air gap formation on the interfacial heat transfer. Consequently, the original algorithm was then modified to include interfacial heat resistance to model the air gap formation. The algorithm is explained in detail in the following chapter. Numerical simulations were conducted on a Silicon Graphics Inc. (SGI) Origin 200 server.

Enthalpy based formulation

During recent years, much interest has been devoted to the numerical analysis of problems involving nonlinear phase change, a phenomenon which takes place in many processes of technological interest to include solidification of various forming processes, freezing problems, applications to solar energy and applications to castings. While for certain materials phase change occurs over a wide band of temperature range thus allowing realistic computational approximations to physically model the situations; for several other materials the phase change phenomenon takes place with almost no temperature variation (a Dirac-δ-type behavior), thereby making such problems more difficult to deal with computationally. Present code (*Ansys*) employs the enthalpy method to tackle the phase change problem which is briefly outlined in this section.

A physical quantity, namely enthalpy, is introduced which is defined as the integral of the heat capacity with respect to temperature and is sufficiently smooth even over the phase change interval. Tamma and Raju (1990) pointed out that the temperature based formulations were ineffective in handling abrupt variations in heat capacity and these formulations approach to approximate heat capacity in the phase change zone. They also observed that the enthalpy methods were more natural in eliminating some of these hindrances to an extent, but still experience some of the same difficulties. The root of the problem was either in accurately representing the temperature distribution, locating the phase front, or both.

Enthalpy is defined as the integral of heat capacity with respect to temperature. Thus,

$$H = \int_{T_0}^{T} \rho \cdot C(T) dT \tag{2.5}$$

or equivalently,

$$\frac{dH}{dT} = \rho \cdot C(T) \tag{2.6}$$

The derivative in the above equation is numerically averaged over each element, from which the value of ρC is obtained.

The enthalpy method incorporates the latent heat in the specific heat of the material. Referring to Figure 3, the typical heat capacity is given by:

$$\rho \cdot C(T) = C_s \qquad \text{for } T_0 < T < T_1 \tag{2.7}$$

$$\rho \cdot C(T) = \rho \cdot C^* = \rho \cdot (\frac{L_h}{\Delta T}) \qquad \text{for } T_1 < T < T_2 \tag{2.8}$$

$$\rho \cdot C(T) = \rho \cdot C_l \qquad \text{for } T_2 < T \tag{2.9}$$

where T_0 = Reference temperature.

ΔT = Phase change interval. Phase transition zone is the temperature difference over which the evolution of latent heat takes place in the enthalpy method.

T_1 = Solidus temperature.

T_2 = Liquidus temperature.

The latent heat of the material is embedded in the adjusted specific heat C^* over the temperature range ΔT.

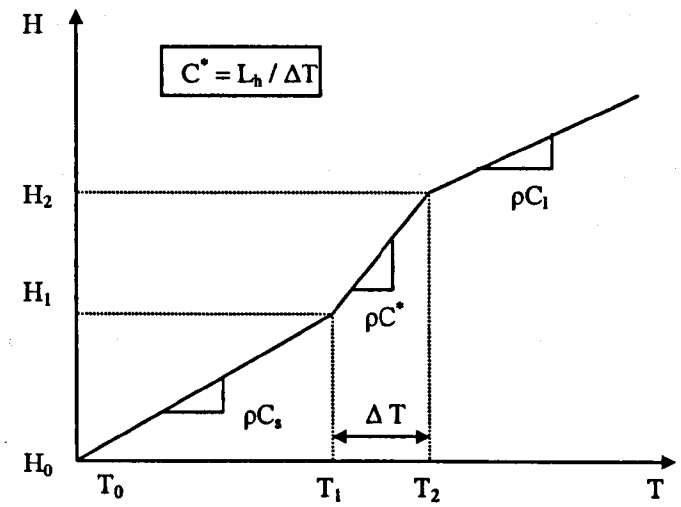

Figure 3. Typical enthalpy versus temperature plot in phase change problem.

For pure metals, solidification is assumed to occur over a finite temperature interval despite isothermal phase change. This phase change range must be kept small to avoid large deviation from the original solidification problem. Additionally, it is quite possible that the temperature at a node may skip the phase change interval in a single iteration if the time step is too large or the grid is not dense enough. Hence, the problem entails careful control of mesh and time stepping.

Rather than direct evaluation of the heat capacity, the enthalpy is interpolated according to:

$$H = N_i(x_i) \cdot H_i(t) \tag{2.10}$$

In equation (2.10), H_i and N_i are the enthalpy values at the nodes and the usual interpolation functions within an element respectively. The heat flow formulation involving solidification employed by the present code is briefly outlined in the following section.

Applying the law of conservation of energy over a differential control area without heat generation we get,

$$\rho \cdot C \cdot (\frac{\partial T}{\partial t} + \{v\}^T \cdot \{L\} \cdot T) = \{L\}^T \cdot ([D] \cdot \{L\} \cdot T) \tag{2.11}$$

where: ρ = Density

C = Specific heat

T = Temperature

t = Time

$$\{L\} = \text{vector operator} = \begin{Bmatrix} \frac{\partial}{\partial x} \\ \frac{\partial}{\partial y} \end{Bmatrix}$$

$$\{v\} = \text{velocity vector for mass transport of heat} = \begin{Bmatrix} v_x \\ v_y \end{Bmatrix}$$

$$[D] = \text{conductivity matrix} = \begin{bmatrix} k_x & 0 \\ 0 & 0 \end{bmatrix}$$

The common form of equation (2.11) can be written as

$$\frac{\partial(\rho C_p T)}{\partial t}+\frac{\partial(\rho V_x C_p T)}{\partial x}+\frac{\partial(\rho V_y C_p T)}{\partial y}=\frac{\partial}{\partial x}\left(k\frac{\partial T}{\partial x}\right)+\frac{\partial}{\partial y}\left(k\frac{\partial T}{\partial y}\right) \tag{2.12}$$

Specified convection over surface S can be represented as:

$$\{q\}^T\{\eta\}=-h(T_\infty-T_s) \tag{2.13}$$

where: $\{q\}$ = heat flux

$\{\eta\}$ = unit outward normal vector

T_∞ = ambient temperature.

T_s = temperature at the surface S of the model

h = coefficient of convective heat transfer.

It should be noted that positive heat flow is into the boundary.

Equation (2.11) is pre-multiplied by a virtual change in temperature δT and integrated over the area of the element to give:

$$\int_{Area}\left(\rho\cdot C\cdot\delta T\left(\frac{\partial T}{\partial t}+\{v\}^T\{L\}T\right)+\{L\}^T(\partial T)([D]\{L\}T)\right)d(area)=\int_S \delta T\cdot T\cdot h(T_\infty-T)d(S) \tag{2.14}$$

where: Area = area of the element

δT = an allowable virtual temperature (= $\delta T(x,y,t)$)

and S = surface of the model where convection is applied.

Since T varies over space and time, it can be written as:

$$T = \{N\}^T \{T_e\} \tag{2.15}$$

where: $T = T(x,y,t)$ = temperature

$\{N\} = \{N(x,y)\}$ = element shape functions

$\{T_e\} = \{T_e(t)\}$ = nodal temperature vector

The time derivative of equation (2.15) can be written as:

$$\dot{T} = \frac{\partial T}{\partial t} = \{N\}^T \left\{\dot{T}_e\right\} \tag{2.16}$$

δT also has the form:

$$\delta T = \{\delta T_e\}^T \{N\} \tag{2.17}$$

Further, using equation (2.15), we have:

$$\{L\}T = [B]\{T_e\} \tag{2.18}$$

where: $[B] = \{L\}\{N\}^T$

Substituting equations (2.13), (2.15), (2.16), (2.17) and (2.18) in equation (2.14), we get:

$$\int_{Area} \rho \cdot C\{N\}\{N\}^T d(Area)\left\{\dot{T}_e\right\} + \int_{Area} \rho \cdot C\{N\}\{v\}^T [B] d(Area)\{T_e\} +$$

$$+ \int_{Area} [B]^T [D][B] d(Area)\{T_e\} = \int_S T_\infty \cdot h \cdot \{N\} d(S) - \int_S h \cdot \{N\} \cdot \{N\}^T \{T_e\} \cdot d(S)$$

(2.19)

Gathering the coefficient of the terms $\left\{\dot{T}_e\right\}$ and $\{T_e\}$ on the left hand side, the equation (2.19) can be represented as:

$$[C_e^t]\left\{\dot{T}_e\right\} + \left([K_e^m] + [K_e^b] + [K_e^c]\right)\{T_e\} = \{Q_e^c\} \tag{2.20}$$

where: $[C_e^t] = \int_{Area} \rho \cdot C\{N\}\{N\}^T d(Area)$ = Element specific heat matrix.

$[K_e^m] = \int_{Area} \rho \cdot C\{N\}\{v\}^T [B] d(Area)$ = Element mass transport conductivity matrix.

$[K_e^b] = \int_{Area} [B]^T [D][B] d(Area)$ = Element diffusion conductivity matrix

$[K_e^c] = \int_S h \cdot \{N\} \cdot \{N\}^T \cdot d(S)$ = Element convection surface conductivity matrix.

$[Q_e^c] = \int_S T_\infty \cdot h \cdot \{N\} d(S)$ = Element convection heat flow vector.

Thus equation (2.20) represents the final form which is solved in each iteration. In this equation the element specific heat matrix $[C_e^t]$ is evaluated from the enthalpy curve for the solidification problem. Hence, referring to Figure 3, the enthalpy values needed to be input with respect to some reference value to get the enthalpy variation to deal with the phase change. A detailed version of the enthalpy formulation could be found in Ansys (1999) and the publication of Namburu and Tamma (1990).

Governing Equations

In this section, the laws governing the problem are elucidated in terms of mathematical expressions. The governing equations are subjected to the boundary conditions of the problem to formulate a solution. These expressions would then be discretized using the finite element approach to estimate the solution. The present problem involved thermal transport with conductive and convective heat transfer. The mold and the post mold were subjected to convective heat transfer whereas conduction was present throughout the domain. As discussed earlier, the solidification was handled by introducing latent heat evolution in the specific heat of the material using the enthalpy method.

Assumptions about the fluid and the analysis are as follows:

1. The fluid is Newtonian, incompressible with Boussinesque approximation.
2. The fluid flow is laminar in the liquid region.
3. There is negligible change in the density with change in phase.
4. Materials were considered homogeneous and isotropic.
5. Material properties were constant within individual phases.
6. Viscous work and viscous dissipation is neglected.
7. In the phase transition zone (ΔT), the thermal conductivity of the domain is equal to the thermal conductivity of the solid phase. In the enthalpy method, evolution of latent heat takes place in the phase transition zone.

The problem is defined by the laws of conservation of mass, momentum and energy which are stated in the following section. These laws are expressed in terms of partial differential equations which are discretized with a finite element technique.

Continuity Equation

From the conservation of mass law comes the continuity equation:

$$\frac{\partial(V_x)}{\partial x}+\frac{\partial(V_y)}{\partial y}=0 \tag{2.21}$$

where:

V_x and V_y = components of the velocity vector in the x and y direction, respectively.

x, y = global Cartesian coordinates.

t = time.

Momentum Equations

The momentum equations, commonly known as the Navier-Stokes equations, govern the fluid flow and are given by:

$$\rho\frac{\partial V_x}{\partial t}+\rho V_x\frac{\partial V_x}{\partial x}+\rho V_y\frac{\partial V_x}{\partial y}=-\frac{\partial P}{\partial x}+\mu\left[\frac{\partial^2 V_x}{\partial x^2}+\frac{\partial^2 V_x}{\partial y^2}\right] \tag{2.22}$$

$$\rho\frac{\partial V_y}{\partial t}+\rho V_x\frac{\partial V_y}{\partial x}+\rho V_y\frac{\partial V_y}{\partial y}=-\frac{\partial P}{\partial y}+\mu\left[\frac{\partial^2 V_y}{\partial x^2}+\frac{\partial^2 V_y}{\partial y^2}\right]+\rho g_y\beta(T-T_\infty) \tag{2.23}$$

Equations (2.22) and (2.23) represent the momentum equation in x and y directions respectively.

Energy equation

The energy equation governs the heat transfer and is given by:

$$\rho C\left[\frac{\partial T}{\partial t}+V_x\frac{\partial T}{\partial x}+V_y\frac{\partial T}{\partial y}\right]=k\left[\frac{\partial^2 T}{\partial x^2}+\frac{\partial^2 T}{\partial y^2}\right] \tag{2.24}$$

The energy equation is the thermal transport equation. As stated earlier, the density of the liquid is constant throughout the domain but subject to the Boussinesque approximation and the specific heat and the thermal conductivity are evaluated according to their respective phases in the domain.

The momentum equation is coupled with the energy equation. In the liquid region the velocity terms are assembled with the appropriate values from the velocity vector field obtained from the solution of momentum equations to get the temperature field. In the solid phase, the X component of velocity is set to zero whereas the withdrawal speed $-U_0$ is substituted for the Y velocity component to account for thermal transport. Thus, the only governing equation in the solid phase is the energy equation. The equations (2.21) through (2.24) are subjected to boundary conditions, which are described in the following section.

Boundary conditions.

The governing equations along with the boundary conditions define the problem completely. The boundary conditions are dictated by various assumptions stated in the previous section of governing equations. Referring to Figure 2, it should be noted that only the left half of the domain was modeled due to symmetry of the problem. The origin is set at the exit of mold wall.

The boundary conditions in dimensional parameters are as follows:

Mold inlet:

At $y = 0; 0 \leq x \leq W$:

$$V_x = 0, V_y = -U_0, T = T_0.$$

Centerline (axis of symmetry):

At $x = W; 0 \leq y \leq L$:

$$V_x = 0, \partial T / \partial x = 0.$$

Pre-mold region:

At $x = 0; 0 \leq y \leq L_1$:

$$V_x = 0, V_y = 0, \partial T / \partial x = 0.$$

Post-mold region:

At $x = 0; (L_1 + L_2) \leq y \leq L$:

$$V_x = 0, V_y = 0, H_3 \text{ (convective heat transfer coefficient).}$$

Mold exit:

At $y = L; 0 \leq x \leq W$:

$$V_x = 0, V_y = -U_0, \partial T / \partial y = 0.$$

Copper mold surface:

At $y = L_1$ and $-t_m \leq x \leq 0$; $y = (L_1 + L_2)$ and $-t_m \leq x \leq 0$; $x = -t_m$ and $L_1 \leq y \leq (L_1 + L_2)$:

H_2 (convective heat transfer coefficient).

The pre-mold is insulated whereas the copper mold and the post-mold region are subjected to surface convection. The metal enters the mold inlet at the superheat temperature and there is no axial heat transfer at the mold exit. Also, there is no heat and mass transfer across mold centerline which is the axis of symmetry. The mold walls are subjected to the no slip boundary condition and the mold entry as well as the exit is subjected to constant withdrawal velocity boundary condition.

Initial conditions:

Initially, the metal is supposed to be at superheat temperature and flowing at withdrawal speed throughout the domain.

At time $t = 0$;

For the entire domain: $T = T_0$, $V_x = 0$ and $V_y = -U_0$.

Non-dimensionalization of Governing Equations

The governing equations were non-dimensionalized by defining basic non-dimensional parameters which are outlined in this section. The following equations define the non-dimensional parameters:

$$X^* = \frac{x}{W} \tag{2.25}$$

$$Y^* = \frac{y}{W} \tag{2.26}$$

$$V_x^* = \frac{V_x}{W}, \; V_y^* = \frac{V_y}{W} \tag{2.27}$$

$$P^* = \frac{P}{U_0^2 \cdot \rho} \tag{2.28}$$

$$\theta = \frac{T - T_\infty}{T_s - T_\infty} \tag{2.29}$$

$$t^* = \frac{U_0 \cdot t}{W} \tag{2.30}$$

where: x, y = linear dimensions

V_x, V_y = velocity components in the x and y directions respectively

U_0 = withdrawal velocity

W = half thickness of the cast material

P = pressure

T_∞ ,T_s = ambient temperature and solidification temperature respectively

In equations (2.25) through (2.30), the superscript (*) is used to define the corresponding non-dimensional parameter. Standard non-dimensional numbers used for the non-dimensionalization of governing equations are stated as follows:

$$\mathrm{Re} = \frac{\rho \cdot U_0 \cdot W}{\mu} \tag{2.31}$$

$$\mathrm{Pr} = \frac{\mu \cdot C}{k} \tag{2.32}$$

$$Gr = \frac{g_y \beta \cdot \rho^2 \cdot W^3 (T - T_\infty)}{\mu^2} \tag{2.33}$$

$$Pe = \mathrm{Re} \cdot \mathrm{Pr} \tag{2.34}$$

$$Ste = \frac{C_s (T_s - T_\infty)}{L_h} \tag{2.35}$$

Substituting equations (2.25) through (2.35) in the governing equations (2.21) through (2.24), we get,

$$\frac{\partial V_x^*}{\partial X^*} + \frac{\partial V_y^*}{\partial Y^*} = 0 \tag{2.36}$$

$$\frac{\partial V_x^*}{\partial t^*} + V_x^* \frac{\partial V_x^*}{\partial X^*} + V_y^* \frac{\partial V_x^*}{\partial Y^*} = -\frac{\partial P^*}{\partial X^*} + \frac{1}{\mathrm{Re}} \left[\frac{\partial^2 V_x^*}{\partial X^{*2}} + \frac{\partial^2 V_x^*}{\partial Y^{*2}} \right] \tag{2.37}$$

$$\frac{\partial V_y^*}{\partial t^*} + V_x^* \frac{\partial V_y^*}{\partial X^*} + V_y^* \frac{\partial V_y^*}{\partial Y^*} = -\frac{\partial P^*}{\partial Y^*} + \frac{1}{\mathrm{Re}} \left[\frac{\partial^2 V_y^*}{\partial X^{*2}} + \frac{\partial^2 V_y^*}{\partial Y^{*2}} \right] + \frac{Gr}{\mathrm{Re}^2} \theta \tag{2.38}$$

$$\frac{\partial \theta}{\partial t^*} + V_x^* \frac{\partial \theta}{\partial X^*} + V_y^* \frac{\partial \theta}{\partial Y^*} = \frac{1}{Pe} \left[\frac{\partial^2 \theta}{\partial X^{*2}} + \frac{\partial^2 \theta}{\partial Y^{*2}} \right] \tag{2.39}$$

Equations (2.36) through (2.39) are the governing equations in the non-dimensional form for the present problem. The governing equations along with the non-dimensional boundary conditions which are defined in the following section, represent a complete set which define the problem of continuous casting.

Non-dimensional Boundary Conditions

The boundary conditions were non-dimensionalized in a similar manner to the govenring equations by using the same non-dimensional parameters as defined in the earlier section.

The boundary conditions in the non-dimensional form are as follows:

Mold inlet:

At $Y^* = L/W$; $0 \leq X^* \leq 1$:

- $V_x^* = 0$, $V_y^* = -1$, $\theta = \theta_0$.

Centerline (axis of symmetry):

At $X^* = 1$; $0 \leq Y^* \leq L/W$:

- $V_x^* = 0$, $\partial\theta / \partial X^* = 0$.

Pre-mold region:

At $X^* = 0$; $(L_2 + L_3)/W \leq Y^* \leq L/W$:

- $V_x^* = 0$, $V_y^* = 0$, $Bi_1 = 0$

Post-mold region:

At $X^* = 0$; $0 \leq Y^* \leq L_3/W$:

- $V_x^* = 0$, $V_y^* = 0$, Bi_3 (convection)

Mold exit:

At $Y^* = 0$; $0 \leq X^* \leq 1$:

- $V_x^* = 0$, $V_y^* = -1$, $\partial\theta / \partial Y^* = 0$.

Copper mold surface:

At $Y^* = L_3/W$ and $-t_m/W \leq X^* \leq 0$; $Y^* = (L_2 + L_3)/W$ and $-t_m/W \leq X^* \leq 0$; $X^* = -t_m/W$ and $L_3/W \leq Y^* \leq (L_2 + L_3)/W$:

- Bi_2 (convection)

To summarize, the mold wall was subjected to a no-slip velocity boundary condition ($V_x^* = 0$, $V_y^* = 0$), whereas the entry and the exit of the mold have a constant withdrawal velocity boundary condition ($V_y^* = -1$). The X- component of the velocity is zero at the centerline ($V_x^* = 0$). Boundary condition of the second kind was applied to the pre-mold, centerline ($\partial\theta / \partial X^* = 0$) and the mold exit ($\partial\theta / \partial Y^* = 0$) as regards the temperature. The metal enters the mold at superheated temperature ($\theta = \theta_0$) and the mold and the post mold surfaces are subjected to convective heat transfer defined by Biot number, Bi_2 and Bi_3, respectively.

Table 2. Thermophysical properties of aluminum and copper.

Property	Liquid aluminum	Solid aluminum	Copper
Density, kg/m^3	2542.5	2542.5	8933
Specific Heat, J/kg K	1080	1076	385
Viscosity, kg/m s	1.3×10^{-3}	-	-
Thermal Conductivity, W/m K	94.03	238	401
Thermal Expansion, /K	1.2×10^{-4}	-	-
Latent heat of fusion, J/kg	3.95×10^{5}	-	-
Phase change temperature, K	933.5	933.52	-

CHAPTER 3

NUMERICAL METHOD

Over the past five decades, solutions to the problem of phase change have been attempted with the help of analytical, semi-empirical and numerical techniques. Numerical techniques can be categorized into finite difference, finite element and finite volume approaches. Finite element analysis seems to have an edge over the other approaches due to its relative ease in handling abrupt non-linearities in material properties. The enthalpy method is one of the most powerful methods available to tackle a phase change problem. As pointed out by Tamma and Raju (1990), the enthalpy-based formulation offered a great potential and promise for numerical simulations of the phase change problem due to its inherent effectiveness in handling the evolution of latent heat.

In the present research, the enthalpy method has been adopted to model the continuous casting process, which was discussed in Chapter 2. This chapter briefly deals with the finite element formulation, user algorithm for continuous casting and the code validation. A computational matrix was set up to study the overall effect of each degree of freedom on the process. The basic algorithm was validated with published analytical and experimental information to benchmark the method. A commercial FEA software, Ansys (1999), was used for the numerical simulations. The following sections describe the element description as well as the finite element discretization.

Element Description

The element used for the present analysis was FLUID141 (Refer Ansys CFD Flotran analysis guide). Figure 4 shows FLUID141, which is a 4 node quad element (triangular 3 node element is also available as an option.). FLUID141 can be used to model transient or steady state fluid/thermal systems that involve fluid and/or non-fluid regions.

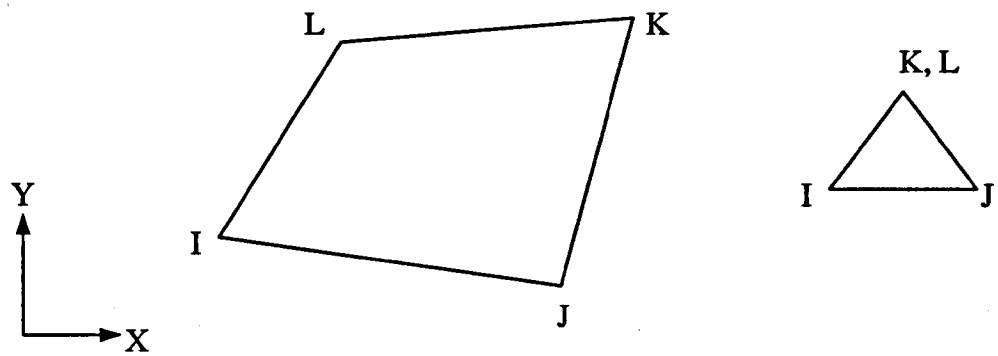

Figure 4. FLUID 141 Element, Ansys (1999)

The material properties defined using this element are density, viscosity, thermal conductivity and specific heat. In addition, enthalpy values at different temperatures need to be input in order to handle solidification. The properties can vary with respect to temperature. Velocities, temperature and pressure constitute the degrees of freedom. The momentum and the energy equation are coupled and are solved to get the velocity and the temperature fields.

It is often required to model systems involving the combination of fluid and non-fluid element, the present code models a maximum of 100 non-fluid elements. Only the

energy equation is solved in the non-fluid region. Material properties of the non-fluid elements include density, specific heat and thermal conductivity and their variation with temperature is permissible. Apart from these features, other user options include choosing turbulence models, different algebraic solvers, multiple species transport and rotating or stationary coordinate system. Detailed information on the models could be found in the Ansys (1999). Table 3 shows the input summary for the element.

Table 3. FLUID141 Input Summary

Element Name	FLUID141
Nodes	I, J, K, L
Degrees of Freedom	Velocities, Pressure, Temperature
Real Constants	See Real Constants. Refer Ansys (1999)
Material Properties	Non-fluid: Conductivity, Density, Specific Heat
	Fluid: Conductivity, Density, Specific heat, Viscosity
Surface Loads	Heat Flux, Convective heat transfer coeff, Radiation
Body Loads	Heat Generation, Force
Special Features	Nonlinear, Six turbulence models, Incompressible or compressible algorithm, transient or steady state algorithm, Rotating or stationary coordinate system, Algebraic solvers particular to FLOTRAN, Optional distributed resistance and fan models, Multiple species transport.
KEYOPT(1)	Activates multiple species transport. 0 - Species transport is not activated. 2 - 6 - Number of species transport equations to be solved
KEYOPT(3)	0 - Cartesian coordinates (default) 1 - Axisymmetric about Y-axis 2 - Axisymmetric about X-axis 3 - Polar Coordinates

Finite Element Formulation

The present code uses a sequential solution algorithm. This means that element matrices are formed, assembled and the resulting system solved for each degree of freedom separately. Development of the matrices proceeds in two parts. In the first, the form of the equations is achieved and an approach taken towards evaluating all the terms. Next, the algorithm is outlined and the element matrices are developed from the equations.

Discretization of the Equations:

The momentum and energy equation have the form of a scalar transport equation. There are four types of terms: transient, advection, diffusion and source. For the purpose of describing the discretization methods, variable ϕ is considered. The form of the scalar transport equation is:

$$\frac{\partial(\rho C_\phi \phi)}{\partial t} + \frac{\partial(\rho V_x C_\phi \phi)}{\partial x} + \frac{\partial(\rho V_y C_\phi \phi)}{\partial y} = \frac{\partial}{\partial x}\left(\Gamma_\phi \frac{\partial \phi}{\partial x}\right) + \frac{\partial}{\partial y}\left(\Gamma_\phi \frac{\partial \phi}{\partial y}\right) + S_\phi \qquad (3.1)$$

where

C_ϕ = transient and advection coefficient

Γ_ϕ = diffusion coefficient

S_ϕ = Source terms.

Table 4 shows the variables, coefficients and the source terms for the transport equations specific to this problem. Substituting the coefficients from Table 4. gives the governing

equations (2.21) through (2.24) for the present problem. The pressure equation is derived using the continuity equation. The development of the pressure equation can be found in the Ansys (1999). Since, the approach is the same for each equation, only the generic transport equation need be treated.

The discretization process, therefore, consists of deriving the element matrices to assemble the following matrix equation:

$$\left([A_e^{transient}]+[A_e^{advection}]+[A_e^{diffusion}]\right)\{\phi_e\}=\{S_e^{\phi}\} \tag{3.2}$$

Galerkin's method of weighted residuals is used to form the element integrals. The suffix e in above equation denotes the element.

Table 4. Transport equation representation specific to the current problem.

ϕ, Degree of freedom (DOF)	C_ϕ	Γ_ϕ	S_ϕ
V_x	1	μ	$-\partial P/\partial x$
V_y	1	μ	$-\partial P/\partial y+\rho\cdot g_y\cdot\beta(T-T\infty)$
T	C	k	0

Transient Term:

The first of the element matrix contributions is from the transient term and a lumped mass approximation is used. The general form is simply:

$$\left[A_e^{transient}\right] = \int W^e \frac{\partial(\rho \cdot C_\phi \phi)^e}{\partial t} d(vol) \tag{3.3}$$

A backward difference scheme is used to evaluate the transient derivative. On a nodal basis, the following implicit formulation is used. The current time step is the nth time step and the expression involves the previous two time step results.

$$\frac{\partial(\phi)}{\partial t} = \frac{(\phi)_{n-2}}{2\Delta t} - \frac{4(\phi)_{n-1}}{2\Delta t} + \frac{3(\phi)_n}{2\Delta t} \tag{3.4}$$

The nth time step produces a contribution to the diagonal of the element matrix, while the derivatives from the previous time step form contributions to the source term.

Advection Term:

The advection term is discretized using the monotone streamline upwind approach based on the idea that pure advection transport is along characteristic lines. In pure advection transport, one assumes that no transfer occurs across characteristic lines, i.e. all

transfer occurs along streamlines. Therefore, it can be assumed that the advection term as expressed in equation (3.5) is constant when expressed along a streamline.

$$\frac{\partial(\rho \cdot C_\phi V_x \phi)}{\partial x} + \frac{\partial(\rho \cdot C_\phi V_y \phi)}{\partial y} = \frac{\partial(\rho \cdot C_\phi V_s \phi)}{\partial S} \tag{3.5}$$

$$\left[A_e^{advection}\right] = \frac{d(\rho \cdot C_\phi V_s \phi)}{ds} \int W^e d(vol) \tag{3.6}$$

This formulation is made for every element, each of which will have only one node, which gets contributions from inside the element. The derivative is calculated using a simple difference (Refer to Figure 5.):

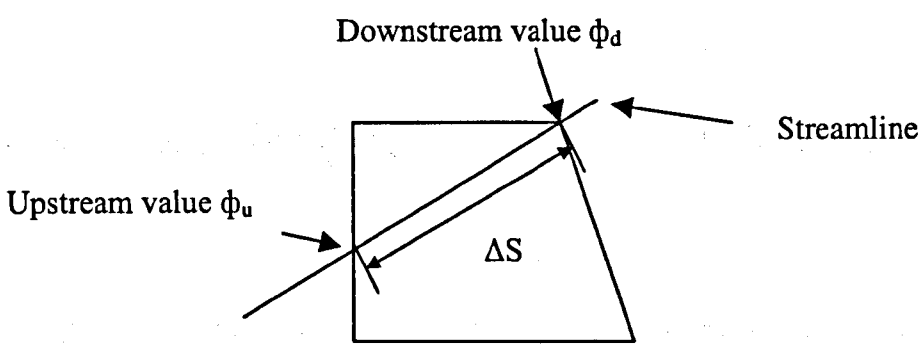

Figure 5. Streamline Upwind Approach over an element.

$$\frac{d(\rho \cdot C_\phi V_s \phi)}{ds} = \frac{(\rho \cdot C_\phi V_s \phi)_u - (\rho \cdot C_\phi V_s \phi)_d}{\Delta S} \tag{3.7}$$

The subscripts d and u represent the values at the downstream and the upstream nodes respectively. The process consists of cycling through all the elements and identifying the downwind nodes. A calculation is made based on the velocities to see where the streamline through the downwind node came from. Weighing factors are calculated based on the proximity of the upwind location to the neighboring nodes.

Diffusion Terms:

The expression for the diffusion terms comes from integration over the problem domain after the multiplication by the weighing function.

$$\text{Diffusion contribution} = \int W^e \frac{\partial}{\partial x}\left(\Gamma_\phi \frac{\partial \phi}{\partial x}\right) d(vol) + \int W^e \frac{\partial}{\partial y}\left(\Gamma_\phi \frac{\partial \phi}{\partial y}\right) d(vol) \tag{3.8}$$

The x and y terms are all treated in similar fashion. Therefore, the illustration is with the term in the x direction. An integration by parts is applied:

$$\int W^e \frac{\partial}{\partial x}\left(\Gamma_\phi \frac{\partial \phi}{\partial x}\right) d(vol) = \int \frac{\partial W^e}{\partial x} \Gamma_\phi \frac{\partial \phi}{\partial x} d(vol) \tag{3.9}$$

Once the derivative of ϕ is replaced by the nodal values and the derivatives of the weighting function, the nodal values will be removed from the integrals.

$$\frac{\partial \phi}{\partial x} = W_x^e \phi \tag{3.10}$$

$$W_x^e = \frac{\partial W^e}{\partial x} \tag{3.11}$$

The diffusion matrix may now be expressed as:

$$\left[A_e^{diffusion}\right] = \int W_x^e \Gamma_\phi W_x^e + W_y^e \Gamma_\phi W_y^e d(vol) \tag{3.12}$$

<u>Source Terms</u>:

The evaluation of the source terms consists of merely multiplying the source terms by the weighting function and integration over the volume.

$$S_\phi^e = \int W^e S_\phi d(vol) \tag{3.13}$$

The enthalpy method is used to model solidification which has been discussed in earlier chapter (Chapter 2).

Segregated Solution Algorithm:

Each degree of freedom is solved in sequential fashion. The equations are coupled, so that each equation is solved with intermediate values of the other degrees of freedom. The process of solving all the equations in turn and then updating the properties is called a global iteration.

The momentum equation is used to generate an expression for the velocity in terms of the pressure gradient. This is used in the continuity equation after it has been integrated by parts. The global iteration structure is shown in Figure 6. $V_x^{'}$ and $V_y^{'}$ are approximate velocities which are obtained by the initial solution of the momentum equations. These approximate values of the velocity components are used to formulate the pressure equation to obtain the pressure values in the liquid. The pressure solution along with the approximate values of the velocity components is used to get a refined velocity field. This velocity vector solution is finally used in the energy equation to get the temperature field. Finally, the global iteration terminates after updating the temperature dependent properties and a convergence check. The detailed exposition of the algorithm can be found in Ansys (1999).

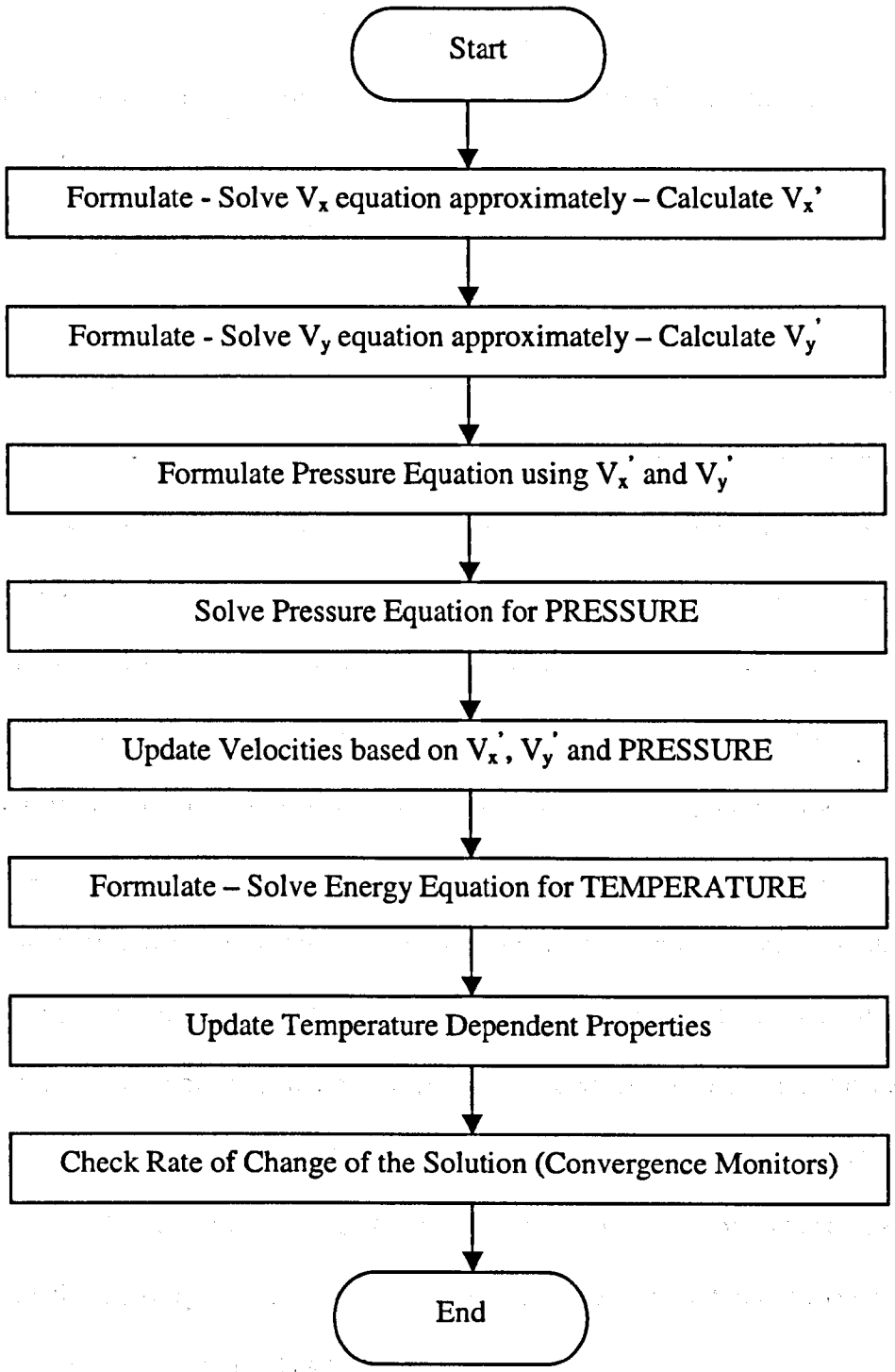

Figure 6. Global iteration structure of Ansys (1999).

User Algorithm

Figure 7 shows the algorithm for continuous casting. The commercial code Ansys (1999) basically solves for velocity and temperature field. The momentum and the energy equations are coupled, i.e. the velocity field is obtained and it serves as an input for the energy equation to solve for temperature. Due to the presence of multiphase flow, a user routine was developed to incorporate the withdrawal speed in the solid region. As illustrated in the algorithm, initially the nodes are identified as liquid or solid by comparing their respective temperature with the solidification temperature. Thus the domain is identified into two zones, namely liquid and solid zone. The momentum equation is solved only in the liquid zone, as it is not applicable to the solid zone. Therefore, the velocities in the solid zone are set to zero while solving the momentum equation. The velocity vector field in the liquid zone obtained by solving the momentum equation serves as an input to the energy equation, which is then solved to get the temperature distribution. In the solid zone, the energy equation is solved by setting $V_x = 0$ and $V_y = -U_0$, to account for thermal transport. Finally, the solution is checked for steady state condition. The normalized rate of convergence is checked for all the degrees of freedom. The convergence monitor was set to 10^{-6}. The solution was assumed to have attained the steady state if the normalized rate of change of all the variables was less than or equal to the convergence monitor value. For any degree of freedom (DOF), ϕ, the convergence monitor is defined as follows:

$$\text{Convergence Monitor} = \sum_{i=1}^{n} \frac{\left|\phi_i^k - \phi_i^{k-1}\right|}{\left|\phi_i^k\right|} \tag{3.14}$$

It represents the sum of the variable calculated from the results between the current k^{th} iteration and the previous $(k-1)^{th}$ iteration, divided by the sum of the current values. The summation is performed over all n nodes, using the absolute values of the differences.

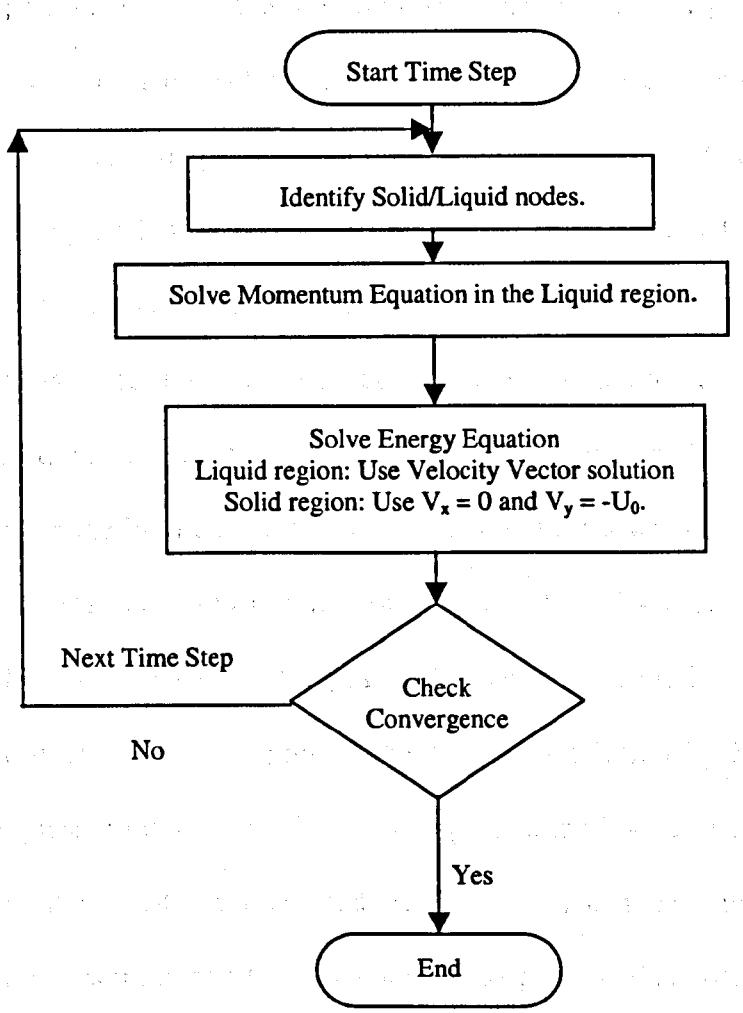

Figure 7. Continuous casting algorithm.

Code Validation

The accuracy of the present code was validated by comparing the results with published analytical and experimental results. This was done to gain confidence in the implementation of the basic algorithm for continuous casting so that it can be modified to incorporate the metal-mold interfacial heat transfer.

Analytical Validation:

The present code and the user algorithm were validated by comparing the results, namely the location of the solidification front, with analytical results by Siegel (1984). Siegel presented an analytical model of a continuously cast slab where a purely mathematical approach was adopted to obtain the solidification front position. Cauchy boundary value method was applied in two steps. First the solidification front shape was obtained to satisfy heat removal from the front due to evolution of latent and due to non-uniform heat transfer from the superheated liquid metal. In the second step, the heat conduction from the liquid metal to the solidification front was obtained. Four cases were run and the results compared in terms of the phase front location as shown in Figure 8. The pre-mold was insulated and the post mold was subjected to boundary condition of the first kind. The dashed lines represent the analytical solution by Siegel (1984) and the solid lines represent the numerical results by present method. The analytical solution was plotted using the equations presented by Siegel. As can be seen from Figure 8, the numerical results were in good agreement with the published analytical data.

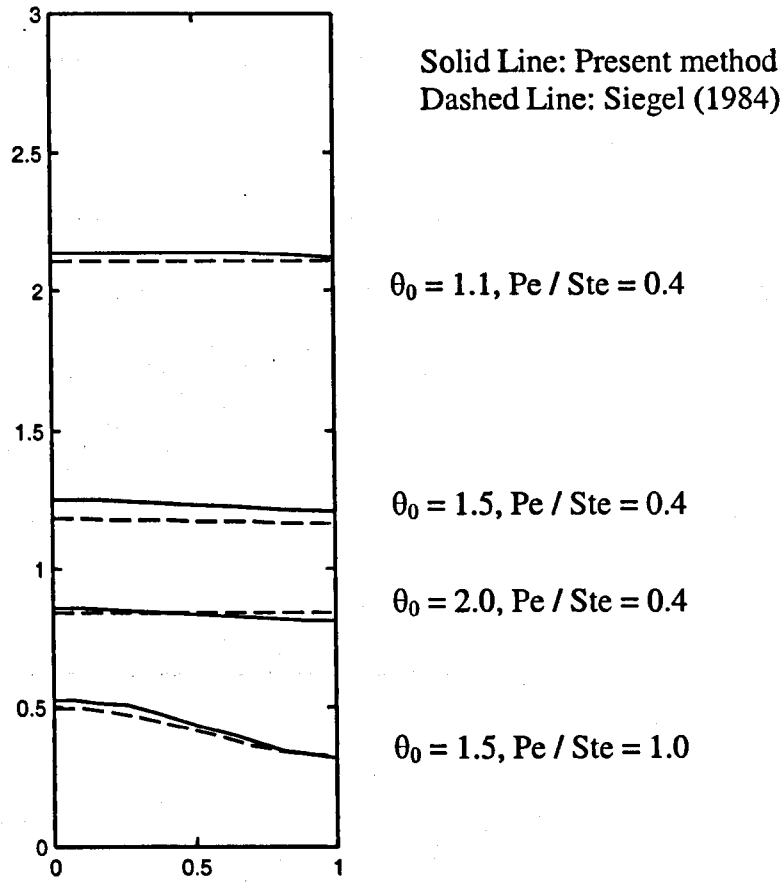

Figure 8. Comparison of numerically obtained solidification front positions with analytical results by Siegel (1984).

Experimental Validation:

Figure 9 shows the geometry of the problem presented by Wolff and Viskanta (1988). It consisted of a rectangular enclosure with boundary condition of the first kind on the vertical faces. Left vertical face and the right vertical face were held at T_h=233°C and T_c=229°C respectively. The horizontal faces were insulated. Molten tin was subjected to solidification. Details of the experimental setup and results could be found in Wolff and Viskanta (1988). Heat is transferred in the solid zone by pure conduction, whereas buoyancy forces are dominant in the liquid zone.

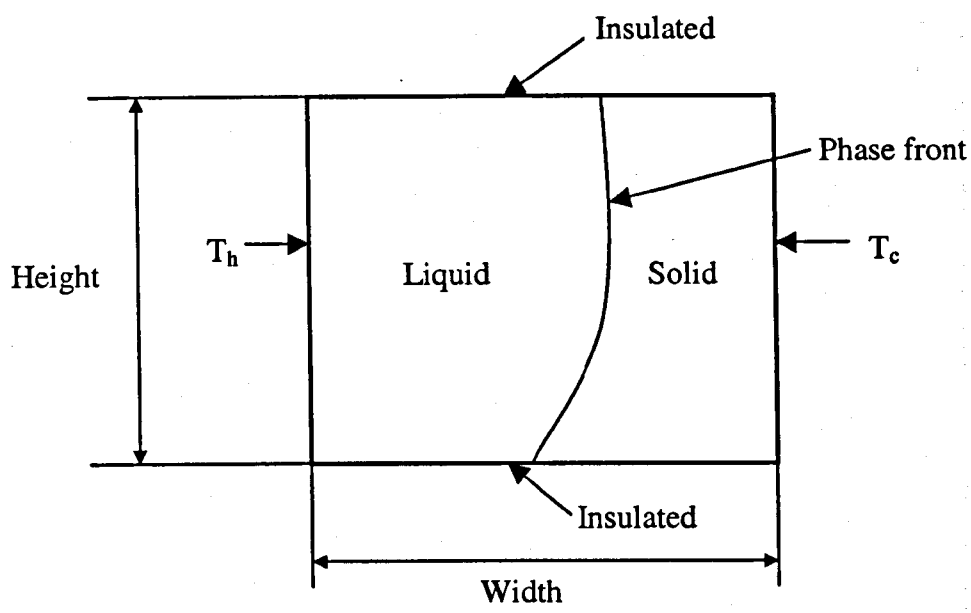

Figure 9. Solidification in an enclosed rectangular cavity; Wolff and Viskanta (1988).

As the experiment proceeds, more and more volume of metal gets solidified. The solidification front locations obtained numerically were compared with the experimental observations at different time intervals. Due to limitations of computational time and space, only three cases (at t = 0.077hr, t = 0.165hr, t = 0.529hr) were analyzed.

Figure 10 shows predicted and the experimentally measured solidification front positions. At early times, t = 0.077hr, the numerical model overpredicted the solidified volume. The discrepancy may be partly attributed to experimental errors, as observed by Wolff and Viskanta (1988). As solidification progresses, the error between the experimental and the numerical results diminished. The results were in good overall agreement with the published experimental data. The problem involved buoyancy flow in an enclosed rectangular cavity. Thus, the validation of this problem also established the correct application of Boussinesque approximation in the present method.

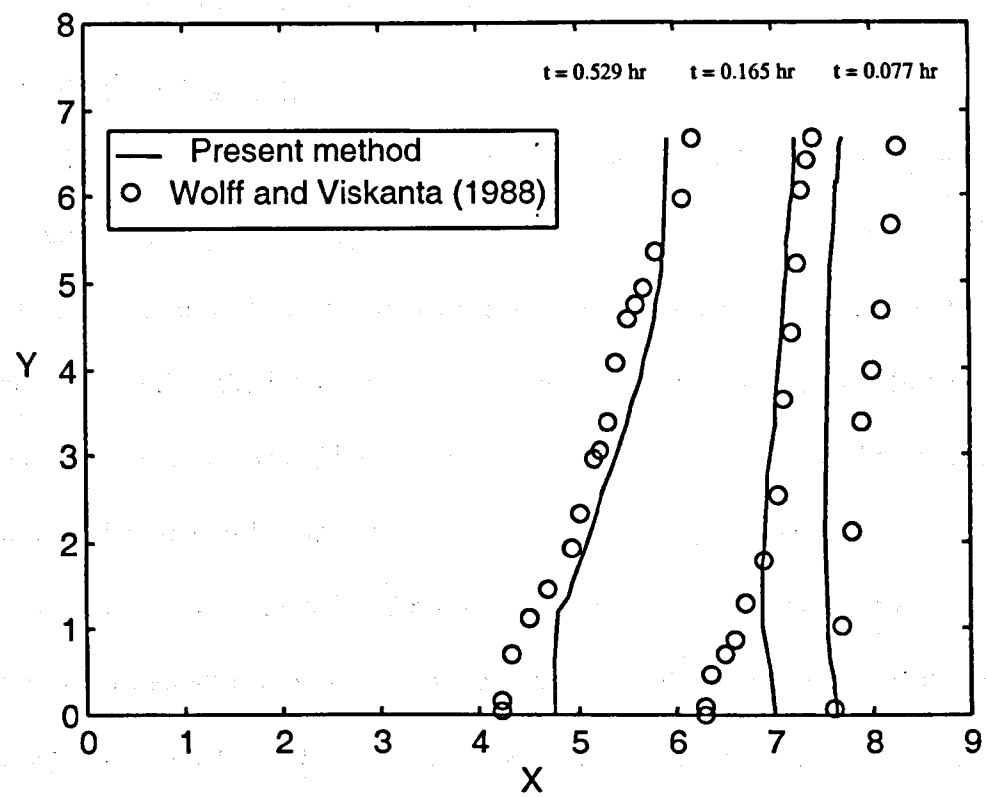

Figure 10. Comparison of numerically obtained solidification front positions with experimental data by Wolff and Viskanta (1988).

CHAPTER 4

INTERFACE HEAT TRANSFER MODEL

Introduction

Metal mold interfacial heat transfer plays an important role in the quality of the casting. The formation of an air gap at the metal-mold interface significantly affects the heat transfer due to reduced contact conductance. Air gap formation can be primarily attributed to metal shrinkage after solidification (phase change and sub-cooling), mold oscillations and mold flux properties. Present work focuses on the effect of air gap formation on the heat transfer due to metal shrinkage.

Quasi-steady state assumption:

Ho and Pehlke (1984,1985) have demonstrated that the quasi-steady state approximation is generally applicable in casting process. From a mathematical point of view, the quantification in terms of a heat transfer coefficient necessitates that heat conduction within the interfacial zone has reached steady state. Heat fluxes entering and leaving the interface would be unequal if the heat flow is considered transient. But, as the width of the air gap formed is sufficiently small it is possible to assume a quasi-steady state condition. Also, as pointed out by Ho and Pehlke, the transient effects due to time variation of radiant energy stored in the gap can usually be neglected as thermal radiation propagates with the speed of light. In order to examine the validity of this assumption, Ho and Pehlke (1984) scrutinized an interface zone consisting of an air gap of 1mm width. The thermal diffusivity of air has a similar magnitude to that of metals like aluminum and

copper since the small volumetric specific heat of air is sufficient to offset the effect of its low thermal conductivity. As a criterion to examine the degree to which a transient heat conduction problem has approached steady state, Ho and Pehlke (1984) have stated that the dimensionless Fourier number Fo, ($Fo = \sqrt{\alpha \cdot t / d}$) should be greater than unity. As reported by them, for an air gap of width d = 1mm, the estimated time is t = 0.0091s. The amount of this characteristic time is less to the rate at which the metal and mold surface temperature varies. This example allows for a quasi-steady state assumption and as seen in the later chapters the air gap formed due to shrinkage is of the order of a few microns which justifies this assumption. Assumptions in the formulation of the interfacial gap, based on the findings of Ho and Pehlke (1984, 1985), are as follows:

1. Shrinkage of the solid metal is uniform based on an average temperature and the shape of the air gap is uniform and continuous.
2. The physical dimensions of the air gap formed are small enough to neglect their effect on the thermal transport due to change in the shape of the domain.
3. Heat flow in the gap is by pure conduction.

Metal-Mold Interface Model Formulation

Figure 11 (b) displays the magnified sketch of the mold where the formation of the air gap takes place. As discussed earlier, the metal shrinks on cooling leading to the air gap formation. This leads to increased resistance to heat flow in the mold. Heat resistance incurred by the air gap is incorporated by changing the mold cooling rate (h_2) to effective heat transfer coefficient H_{eff} ($H_{eff} < h_2$). As seen in Figure 11 (a), H_{eff} is only

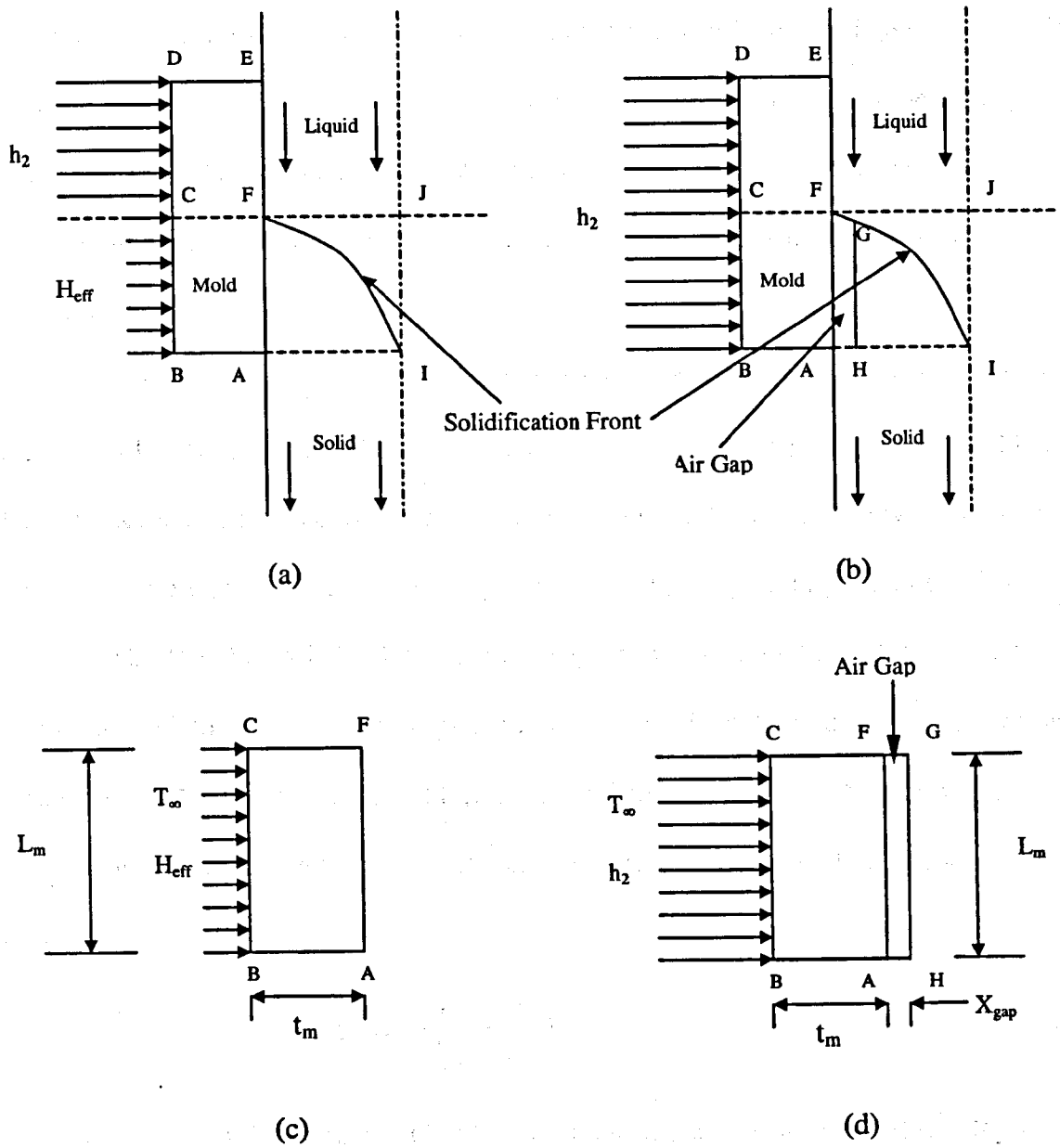

Figure 11. Effective heat transfer coefficient formulation.

a) Application of effective air gap heat resistance in terms of H_{eff},

b) Interfacial air gap formation, c) Magnified view of Area ABCF in Figure 11 (a), d)

Magnified view of Area HBCG in Figure 11 (b)

applied till the point C from the mold exit D on the mold surface, i. e. H_{eff} is only applied over the corresponding vertical length of the air gap. Thus, H_{eff} handles the air gap heat resistance where $H_{eff} < h_2$ and is calculated based on the shrinkage of the solidified metal in the mold. One-dimensional heat transfer was assumed in the formulation of H_{eff}, which is as follows.

The heat resistance due to the air gap is incorporated in the effective heat transfer coefficient H_{eff} [Figure 11 (a)] instead of physically modeling the air gap [Figure 11 (b)]. The total resistances to heat flow across the mold in both the models shown in Figures 11 (a) and (b) are equated to obtain an expression for H_{eff}. Figure 11 (c) and (d) illustrates the area ABCF and area HBCG of the mold shown in Figure 11 (a) and (b) respectively. The air gap width represented by segment FG is assumed small enough to consider it as a straight line. Referring to Figure 11 (c), the total resistance to the heat flow R_1, is the combination of the individual heat resistances due to the copper mold and convection on its surface.

$$R_1 = \left(\frac{1}{H_{eff}} + \frac{L}{k_{Cu}}\right) \tag{4.1}$$

Similarly, referring to Figure 11 (d), the total resistance to heat flow, R_2 is the combination of the individual heat resistance of the air gap, the copper mold and the mold surface convection.

$$R_2 = \left(\frac{1}{h_2} + \frac{L}{k_{Cu}} + \frac{X_{gap}}{k_{air}}\right) \tag{4.2}$$

Equating the resistances R_1 and R_2 from equation (4.1) and (4.2) we get,

$$(\frac{1}{h_2}+\frac{L}{k_{Cu}}+\frac{X_{gap}}{k_{air}})=(\frac{1}{H_{eff}}+\frac{L}{k_{Cu}})$$

or

$$H_{eff}=(\frac{k_{air}.h_2}{k_{air}+X_{gap}.h_2}) \tag{4.3}$$

Hence, knowing the value of air gap width X_{gap}, the effective heat transfer coefficient H_{eff} can be calculated. Equation (4.3) is used in the present numerical investigation by applying the calculated value of H_{eff} over the mold surface as demonstrated earlier in Figure 11 (a).

<u>Calculation of air gap width, X_{gap}</u>

Air gap width is calculated based on the two-dimensional metal shrinkage in the mold region. Metal shrinkage can be calculated as follows:

$$\Delta A = A_1.\beta.\delta T \tag{4.4}$$

where A_1 = Area of the solidified metal in the mold region [Area AFJI in Figure 11 (a)].

ΔA = Shrinkage area

β = $2 \cdot \alpha$, where α is the linear coefficient of expansion.

δT = Temperature difference = $(T_{avg} - T_s)$

T_{avg} = Average temperature of the solidified region.

T_s = Solidification temperature of the material.

Isotropic contraction was assumed and solidification temperature was taken as the reference temperature for contraction. The following section explains the method employed for calculating the area of the solidified metal A_1 and the average temperature of the solidified region T_{avg}, as referred in equation (4.4).

a. Calculation of solidified area of the metal, A_1

Figure 12 shows the typical finite element mesh for area A_1 [Area AFJI in Figure 11 (a)] of solidified metal in the mold region, referred to in equation (4.4).

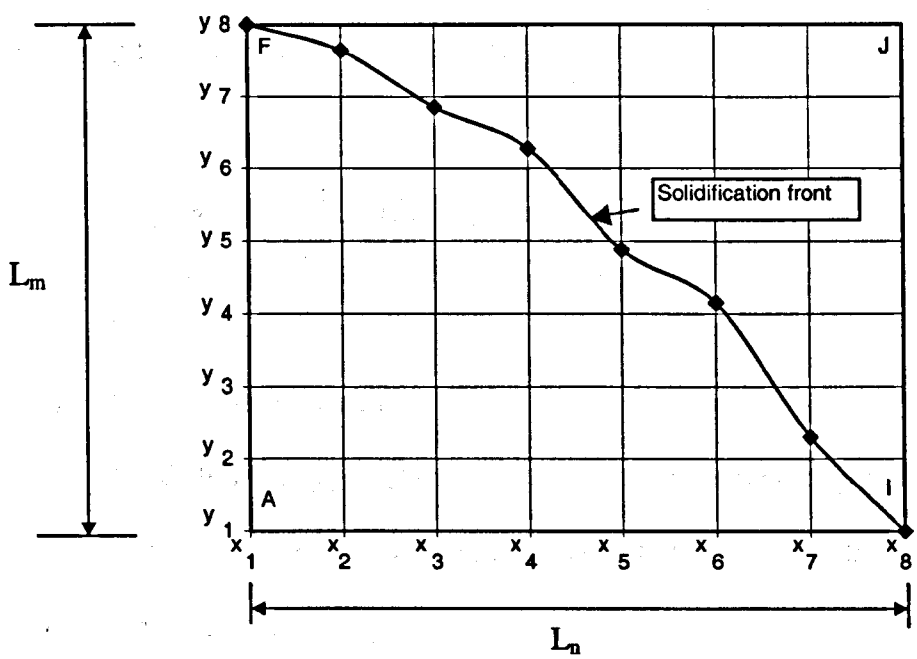

Figure 12. Typical finite element mesh of the solidified metal in the mold.

Numerical integration using Simpson's rule was employed to calculate the solid metal area A_1. Ordinates of the phase front at corresponding mesh verticals served as an

input for the numerical integration. If the solid front passed between two nodes, linear interpolation was employed to calculate the exact location based on the temperature of the nodes. Simpson's rule can be applied to even number of divisions. If the area under the solid front was comprised of odd number of divisions, then Simpson's rule was applied to the entire area except the last division where the midpoint rule was used.

b. Calculation of T_{avg}

The average temperature of the solidified metal area A_1 in the mold was obtained by double integration of the temperatures of the nodes in the area A_1. Simpsons rule of numerical integration was used for calculating T_{avg}.

Thus referring to Figure 12, T_{avg} is given by,

$$T_{avg} = \frac{1}{L_m \cdot L_n} \iint T_i dx_i dy_i \tag{4.5}$$

where,

T_i = temperature at node i.

L_m = the difference $(y_8 - y_1)$ in Figure 12, i.e. the vertical length of the solid shell on the copper mold wall, which is equal to the length of the segment AF in Figure 11(a).

L_n = the difference $(x_8 - x_1)$ in Figure 12, i.e. the shell thickness at the copper mold exit, which is equal to the length of the segment AI in Figure 11 (a).

The value of L_m and L_n is obtained from a subroutine which sorts the node on the mold wall and the mold region exit respectively to get the corresponding locations of points F and I in Figure 12. Points F and I in Figure 12 lie on the solidification front and hence their temperature is equal to the solidification temperature.

The metal shell shrinks after solidification and this metal shrinkage gives rise to an air gap. Therefore the metal shrinkage equals to the area of the air gap formed. Referring to Figure 11(d), it can be deduced that the area of the air gap, which is equal to the metal shrinkage, is equal to the area of the rectangle AFGH.

$\Delta A = L_m \cdot X_{gap}$

Then,

$$X_{gap} = \frac{\Delta A}{L_m} \tag{4.6}$$

Thus, substituting the value of X_{gap} obtained from equation (4.6) in equation (4.3) gives the effective heat transfer coefficient H_{eff}.

User Algorithm for Air Gap Formation

The algorithm for modeling the effective air gap heat resistance at the metal-mold interface is illustrated in Figure 13. The basic algorithm for continuous casting discussed in Chapter 3 was modified to include the effective heat resistance due to air gap formation. As discussed in the previous section of this chapter, the effective heat resistance was accounted for by changing the coefficient of convective heat transfer on the outer surface of the copper mold. In each time step, the effective heat transfer coefficient was calculated based on the formulation. The boundary condition, H_{eff}, on the outer surface of the mold was then updated for the next time step. Time step was carefully controlled to avoid divergence due to inherent stiffness of the problem. Also, since a small value of air gap width leads to a considerable change in the effective heat transfer coefficient, it was necessary to apply relaxation factors to the degree of freedom variables. Relaxation factor is defined as:

$$\phi_i^{new} = (1 - r^{\phi}) \cdot \phi_i^{old} + r^{\phi} \cdot \phi_i^{calculated} \tag{4.7}$$

where,

ϕ = any degree of freedom (DOF) variable.

r^{ϕ} = relaxation factor applied to ϕ.

In simple terms, the relaxation factor adds the fraction of the previous solution to the new solution, depending on its value.

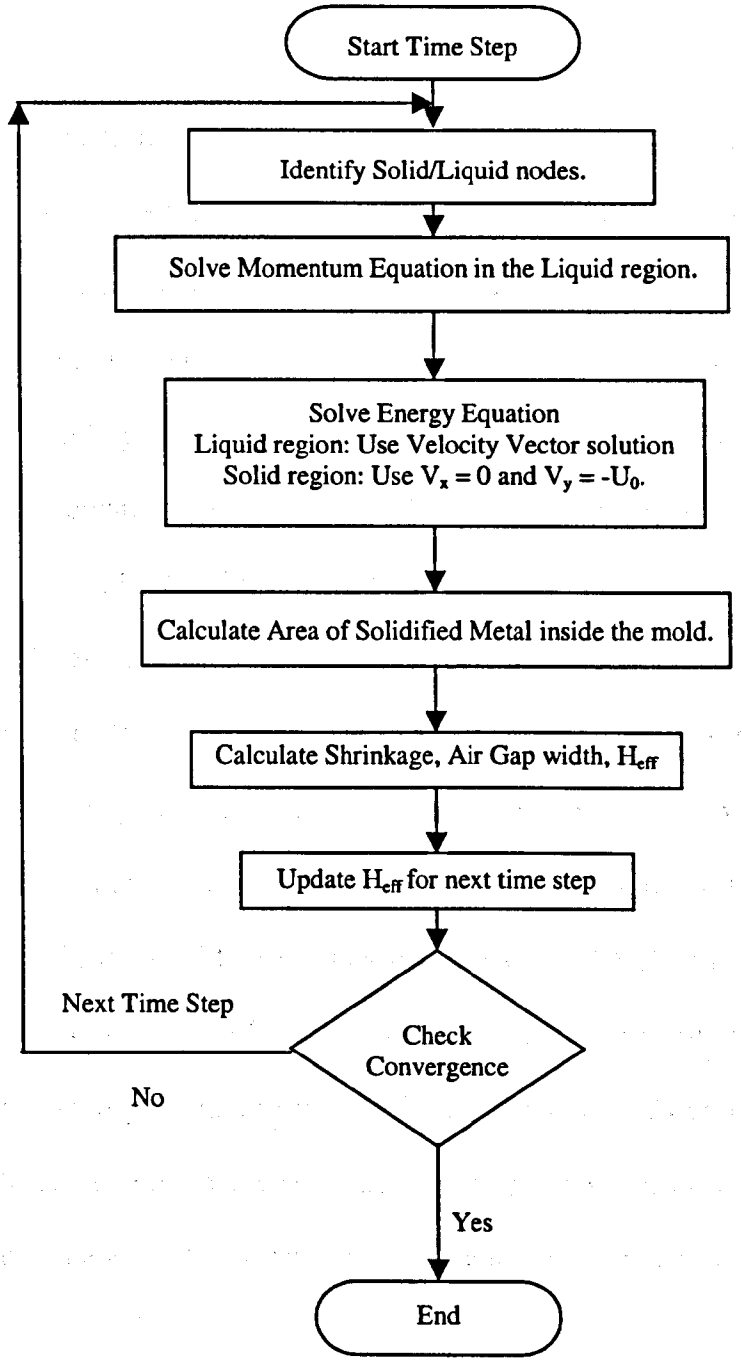

Figure 13. Algorithm for incorporating effective heat resistance due to air gap.

Grid Independence test

Mesh sensitivity testing was carried out to choose a grid size that produced accurate results at a computationally optimum time. The computation time increases with the increase in the number of elements. The mesh was carefully chosen as to avoid steep gradients. The mesh was denser in the mold region and near the wall due to the existence of a no-slip boundary condition and steep temperature gradient. Simpson's rule, which is employed to calculate the solidified metal area in the mold, is a fifth order rule. Thus, small nodal spacing leads to less round off error in the numerical integration.

Two different grids were examined, one with 2600 elements and the other with 5700 elements. In the latter case, the number of elements was more than double the smaller grid. The grids were tested by running a stiff case with higher values of parameters. The parameters chosen were, $\theta_0 = 2.0$, $Pe = 3.0$, $Bi_2 = 0.3$, $Bi_3 = 0.4$. Choosing a stiff case would ensure that the grid would be effective and computationally economical for low values of process parameters. The metal-mold interface modeling algorithm was incorporated and the results for the two grids compared. The centerline and the wall temperatures were compared for both the grids, as the temperature gradient is maximum at these locations. The temperature distribution is shown in Figure 14.

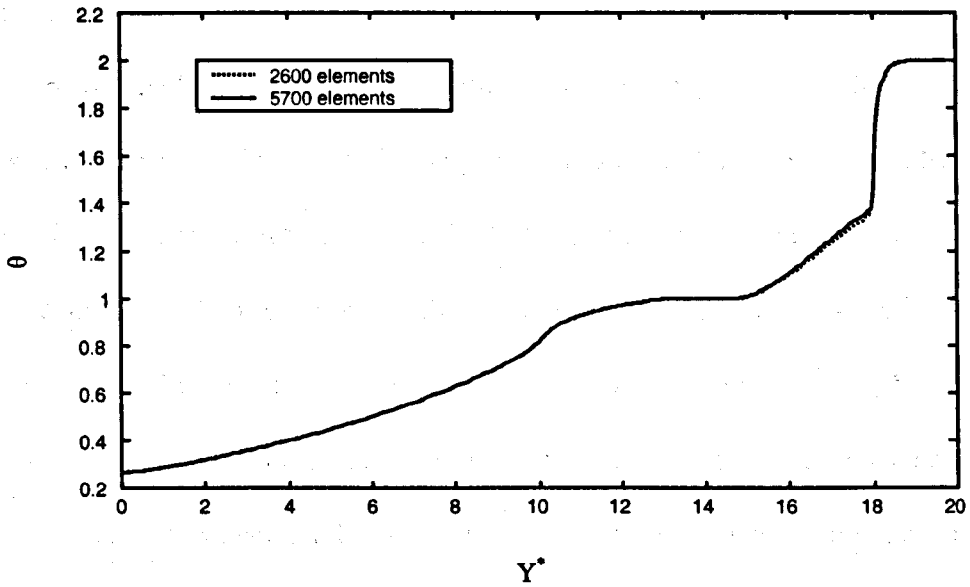

(a) Wall temperature

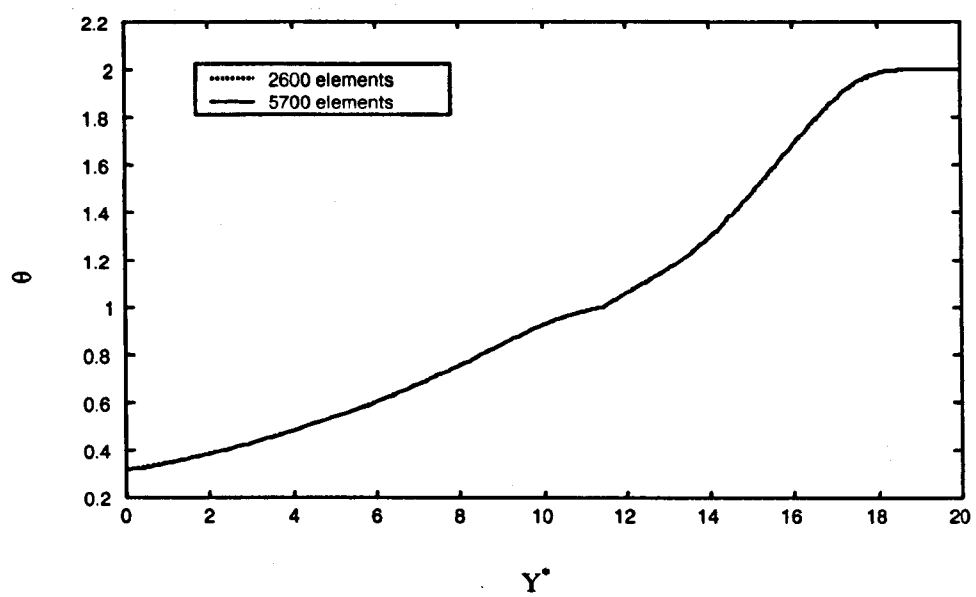

(b) Centerline temperature

Figure 14. Comparison of temperature profile for grid independence.

The maximum temperature difference along the wall and the centerline was equal to 2% and 1% respectively. Hence, the grid with 2600 elements, which is shown in Figure 15. was used for the numerical study in the present research. As stated earlier, Simpsons rule of numerical integration was used to calculate the area and the average temperature of the solidified metal in the mold region. Decreasing the node spacing results in a coarse grid which increases the error in the numerical integration by Simpsons rule. Simpsons rule is a fifth order method which means the error in the calculation is directly proportional to the fifth order of the distance between two adjacent nodes. Hence, a denser mesh would ensure least probable error in the calculation. Therefore a grid with lesser number of elements was not tested, as it would drastically increase the error in the calculation of area and the average temperature of the solid in the mold.

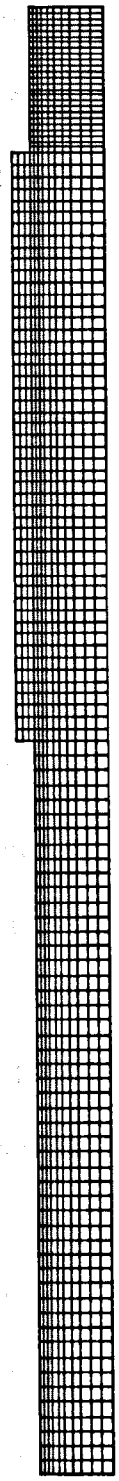

Figure 15. Computational mesh with 2600 elements.

CHAPTER 5

RESULTS AND DISCUSSIONS

Introduction

The results of the numerical analysis were judiciously interpreted to deduce meaningful conclusions. The analyses were conducted with and without air gap modeling to get a better comprehension of the metal-mold interfacial heat transfer. The problem was analyzed as a transient one and the results were obtained at a steady state condition. Ideally, at steady state condition there is no change in the values of degrees of freedom. In the current problem, steady state was assumed to have been reached when the normalized rate of change of all the variables was less than the convergence monitor value as defined earlier.

Primarily, the effect of four process variables was studied: withdrawal speed, superheat, mold cooling rate and the post-mold cooling rate. Only one parameter was allowed to vary at one time to study the effect of that parameter on the heat transfer. The effect of each parameter on the phase front location, temperature distribution, heat flux variation and mold heat extraction was studied. Some cases were also examined by comparing their results with and without air gap formation. The input and the output parameters for the code were in dimensional terms. Hence, to generalize the output for comparison, the results were non-dimensionalized by the use of certain predefined non-dimensional parameters. The non-dimensionalization procedure is outlined in a previous section in Chapter 2. A summary of these non-dimensional parameters with a brief description is repeated in the next section.

Non-Dimensionalization of Results

As discussed earlier, the results obtained were non-dimesionalized by defining basic non-dimensional parameters. Non-dimensionalization of results establishes scaling laws between models and thus provides maximum information as regards the system behavior in terms of its primary and secondary variables. The following non-dimensional parameters were employed to represent the results.

The Stefan number relates the ambient temperature of the system to the solidification temperature:

$$Ste = \frac{C_s \cdot (T_s - T_\infty)}{L_h} \tag{5.1}$$

Stefan number (Ste) was kept constant throughout the analyses and was equal to 2.5.

Withdrawal velocity was expressed in terms of Peclet number. The Peclet number takes into account the withdrawal speed, half-thickness of the cast material and the thermal diffusivity.

$$Pe = \frac{U_0 \cdot W}{\alpha_s} \tag{5.2}$$

The superheat temperature was expressed in terms of θ_0, which was defined as follows:

$$\theta_0 = \frac{T_0 - T_\infty}{T_s - T_\infty} \tag{5.3}$$

The mold cooling rates were non-dimensionalized using the Biot number, which was expressed in terms of convective heat transfer coefficient, half-thickness of the cast

material and the corresponding thermal conductivities. The pre-mold was insulated which gives zero value for Bi_1. The mold and the post-mold Biot numbers were expressed in terms of the thermal conductivity of copper and solid aluminum respectively. The mold and the post mold Biot numbers, Bi_2 and Bi_3, were defined as follows:

$$Bi_2 = \frac{h_2 \cdot W}{k_{Cu}} \tag{5.4}$$

$$Bi_3 = \frac{h_3 \cdot W}{k_{Al-solid}} \tag{5.5}$$

The effective heat transfer coefficient on the outer surface of the mold due the air gap formation was defined as:

$$H^* = \frac{H_{eff} \cdot W}{k_{Cu}} \tag{5.6}$$

The derived quantities included the local heat flux and the average heat flux. The local heat flux was non-dimensionalized as follows.

Considering the energy balance at the outer edge of the material, the heat flux can be represented as:

$$q = h \cdot (T - T_\infty) = -k \cdot \frac{\partial T}{\partial x} \tag{5.7}$$

Dividing equation (5.7) by $k \cdot (T - T_\infty) / L$ gives,

$$q^* = \frac{h \cdot L}{k} \tag{5.8}$$

Since the thermal conductivity of the domain is variable, the thermal conductivities of solid and liquid aluminum were used at corresponding locations depending on the respective phases. The non-dimensional local heat flux values obtained were integrated to obtain the overall dimensionless heat flux, Q^*, for the outer surface, as shown in equation (5.9).

$$Q^* = \frac{1}{L}\int_0^L q^* \cdot dy \tag{5.9}$$

The linear dimensions, x and y, were non-dimensionalized as:

$$X^* = \frac{x}{W} \tag{5.10}$$

$$Y^* = \frac{y}{W} \tag{5.11}$$

The non-dimensional air gap width was represented as:

$$G^* = \frac{X_{gap}}{W} \tag{5.12}$$

Computational Matrix

The main objective was to study the effect of air gap formation on the heat transfer phenomenon in continuous casting. A number of different numerical cases were run to study the effect of four basic parameters, namely, superheat temperature, withdrawal speed, mold cooling rate and the post-mold cooling rate. The output of these numerical runs was analyzed to understand the effect of each parameter. Only one parameter was allowed to be changed at a time, so that its effect on the heat transfer of the system could be understood. Calculated values like local heat flux, overall heat flux, effective heat transfer coefficient, air gap width and the fractional heat extracted in the mold were also used for comparison besides basic parameters like temperature and velocity fields.

The ranges of different parameters considered were:

- $Pe = 1.0 - 4.0$
- $\theta_0 = 1.2 - 3.0$
- $Bi_2 = 0.02 - 0.1$
- $Bi_3 = 0.05 - 0.15$

It can be seen that higher withdrawal speeds were investigated and since air gap formation would decrease the efficiency of heat extraction in the mold, relatively higher values of mold cooling rates were used to prevent breakout. The Stephan number (*Ste*) and Bi_1 were fixed to 2.5 and zero respectively. The different values of the parameters used in code validation [Siegel (1984)] (earlier in Chapter 3), provided the basis to

formulate the computational matrix which is shown in Table 5. A total of 36 cases were run with air gap modeling.

Table 5. Computational matrix for the current study with air gap modeling.

θ_0	Pe	Bi_2	Bi_3
1.2	2.0	0.02	0.05
1.2	2.0	0.05	0.05
1.2	2.0	0.1	0.05
1.2	2.0	0.02	0.1
1.2	2.0	0.05	0.1
1.2	2.0	0.1	0.1
1.2	2.0	0.02	0.15
1.2	2.0	0.05	0.15
1.2	2.0	0.1	0.15
1.2	2.5	0.02	0.05
1.2	2.5	0.05	0.05
1.2	2.5	0.1	0.05
1.2	2.5	0.02	0.1
1.2	2.5	0.05	0.1
1.2	2.5	0.1	0.1
1.2	2.5	0.02	0.15

Table 5 continued.

θ_0	Pe	Bi_2	Bi_3
1.2	2.5	0.05	0.15
1.2	2.5	0.1	0.15
1.2	1.2	0.1	0.15
1.2	1.5	0.1	0.15
1.2	1.8	0.1	0.15
1.2	3.0	0.1	0.15
1.2	3.5	0.1	0.15
1.2	4.0	0.1	0.15
1.2	1.0	0.02	0.05
1.2	1.2	0.02	0.05
1.2	1.5	0.02	0.05
1.5	1.5	0.1	0.15
2.0	1.5	0.1	0.15
2.5	1.5	0.1	0.15
3.0	1.5	0.1	0.15
1.5	2.0	0.1	0.15
2.0	2.0	0.1	0.15
2.5	2.0	0.1	0.15

Table 5 continued.

θ_0	Pe	Bi_2	Bi_3
2	3	0.1	0.15
2.5	3	0.1	0.15

In addition to the cases shown in Table 5, 9 cases were run without air gap modeling to compare the results of the same with air gap modeling. This was done to get a better understanding of the effect of air gap formation on the process. Table 6 shows the cases run without air gap. In all 54 cases were executed including grid independence and code validation.

Table 6. Computational matrix for cases run without air gap modeling.

θ_0	Pe	Bi_2	Bi_3
1.2	1.2	0.1	0.15
1.2	2.0	0.1	0.15
1.2	2.5	0.1	0.15
1.2	3.0	0.1	0.15
1.2	4.0	0.1	0.15
1.2	2.0	0.02	0.05
1.2	2.5	0.02	0.05
3.0	1.5	0.1	0.15
2.5	2.0	0.1	0.15

Effect of Withdrawal Speed

Withdrawal speed was expressed in the terms of non-dimensional parameter Pe, Peclet number as defined in earlier chapters. The following cases were run with air gap modeling to study the effect of withdrawal speed:

(a) $\theta_0 = 1.2$, $Bi_2 = 0.1$, $Bi_3 = 0.15$, Pe = 1.2, 1.5, 1.8, 2.0, 2.5, 3.0, 3.5, 4.0.

(b) $\theta_0 = 1.2$, $Bi_2 = 0.02$, $Bi_3 = 0.05$, Pe = 1, 1.2, 1.5, 2.0, 2.5.

The superheat (θ_0) was kept constant at 1.2, and two different cooling rates were incorporated to study the effect of withdrawal speed. Case (a) employs the highest value of cooling rates whereas Case (b) employs the lowest value in the present study. The Peclet number ranged from 1 to 4. Higher Peclet numbers were investigated, as higher withdrawal speeds are desirable for higher productivity. Figures 16 (a) and 16 (b) show the solidification front locations for Cases (a) and (b) respectively. The phenomenon of continuous casting is a transient one; hence, as Pe increases, the liquid metal has higher velocities and less time to cool and, consequently the solidification front moves down the mold. The movement of the phase front is more prominent in Case (b) as compared to Case (a) because Case (b) has relatively lower cooling rates. Also, the slope of the front becomes steeper with an increase in Pe; the steepest slope is exhibited at Pe = 4.0 for $\theta_0 = 1.2$, $Bi_2 = 0.1$, $Bi_3 = 0.15$. For higher mold cooling rates, the position of the solidification front on the wall differs by small magnitudes as compared to that with Case (b). However, the slope of the solidification front was steeper in the case of higher cooling rates [Case (a)] for the same Peclet numbers. No breakout condition was observed, despite high values of Peclet number.

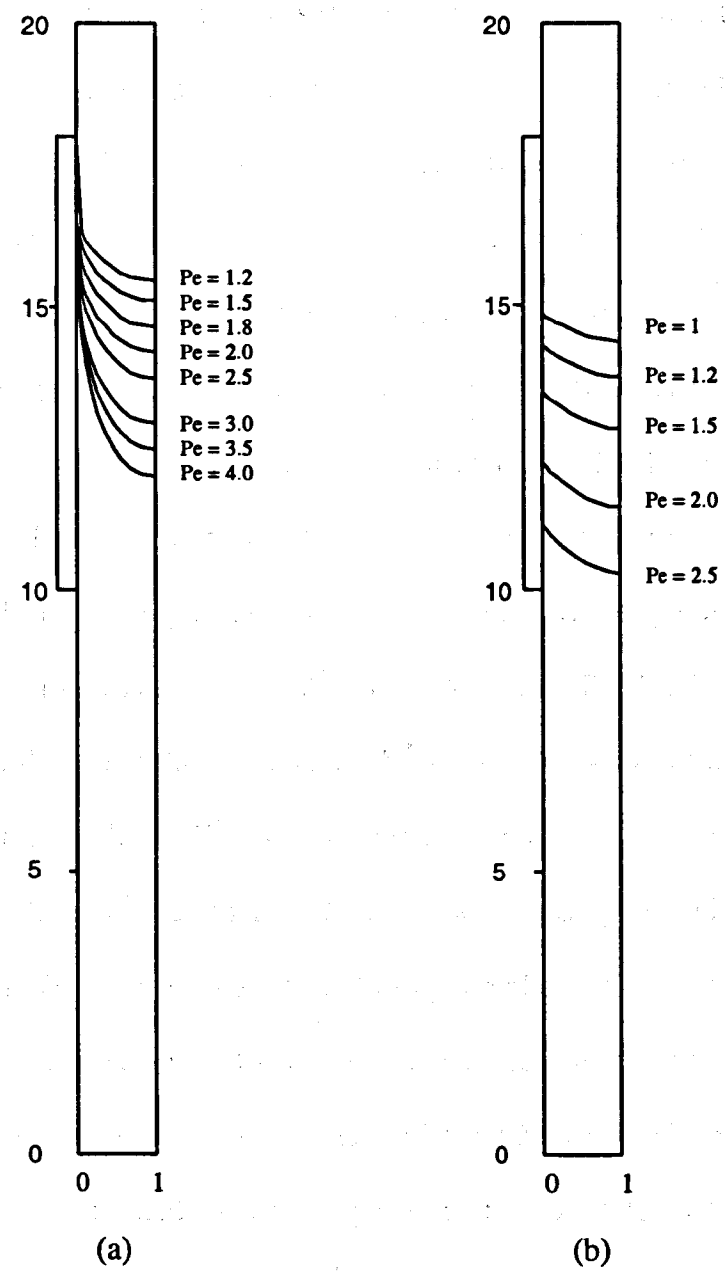

Figure 16. Effect of withdrawal speed on solidification front:

a) $\theta_0 = 1.2$, $Bi_2 = 0.1$, $Bi_3 = 0.15$

b) $\theta_0 = 1.2$, $Bi_2 = 0.02$, $Bi_3 = 0.05$

Figure 17 shows a typical velocity vector plot for $\theta_0 = 2.0$, $Bi_2 = 0.1$, $Bi_3 = 0.15$, $Pe = 4.0$. The velocity vectors are uniform at the entry of the mold due to a constant withdrawal velocity boundary condition. However, the magnitude of the velocity vectors decreases towards the solidification front and consequently zero velocities are observed at the solidification front. Distortion of vectors was observed near the solidification front. The vectors also tend to move more towards the wall along the ordinates.

Variation of non-dimensional local heat flux along the wall for $\theta_0 = 1.2$, $Bi_2 = 0.02$, $Bi_3 = 0.05$, $Pe = 1, 1.2, 1.5, 2.0, 2.5$ is shown in Figure 18. For a given Peclet number, the local heat flux values are at maximum at the entry of the mold region. The pre-mold is subjected to boundary condition of the second kind (i.e. pre-mold region is insulated, hence the heat flux is zero from $Y^* = 18$ to $Y^* = 20$). The local heat flux rises abruptly from zero in the pre-mold region (from $Y^* = 20$ to $Y^* = 18$ in the downstream direction) to its maximum value at $Y^* = 18$ which is the entry of the copper mold. In the downstream direction, from $Y^* = 20$ to $Y^* = 0$, there is a sharp drop in the heat flux from $Y^* = 18$ (the entry of mold region) to the point of inception of the solidification front. The local heat flux remains almost constant from the solidification front position on the wall up to the mold exit. In this region, lower values of local heat flux along the wall are observed which can be attributed to the air gap formation as it leads to higher heat resistance or lower contact conductance. At $Y^* = 10$, the flux increases as the metal exits the mold where the air gap ceases to exist. The discontinuity in the curves at $Y^* = 10$ is due to the change in the boundary condition at the mold exit ($Bi_2 \neq Bi_3$). The post-mold

region is subjected to water spray cooling where the flux values show a constant decrease as sensible heat is extracted from the metal as it moves further downstream .

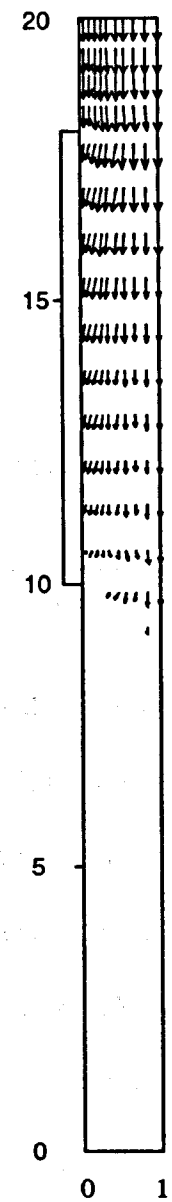

Figure 17. Velocity vector field for $\theta_0 = 2.0$, $Bi_2 = 0.1$, $Bi_3 = 0.15$, $Pe = 4.0$.

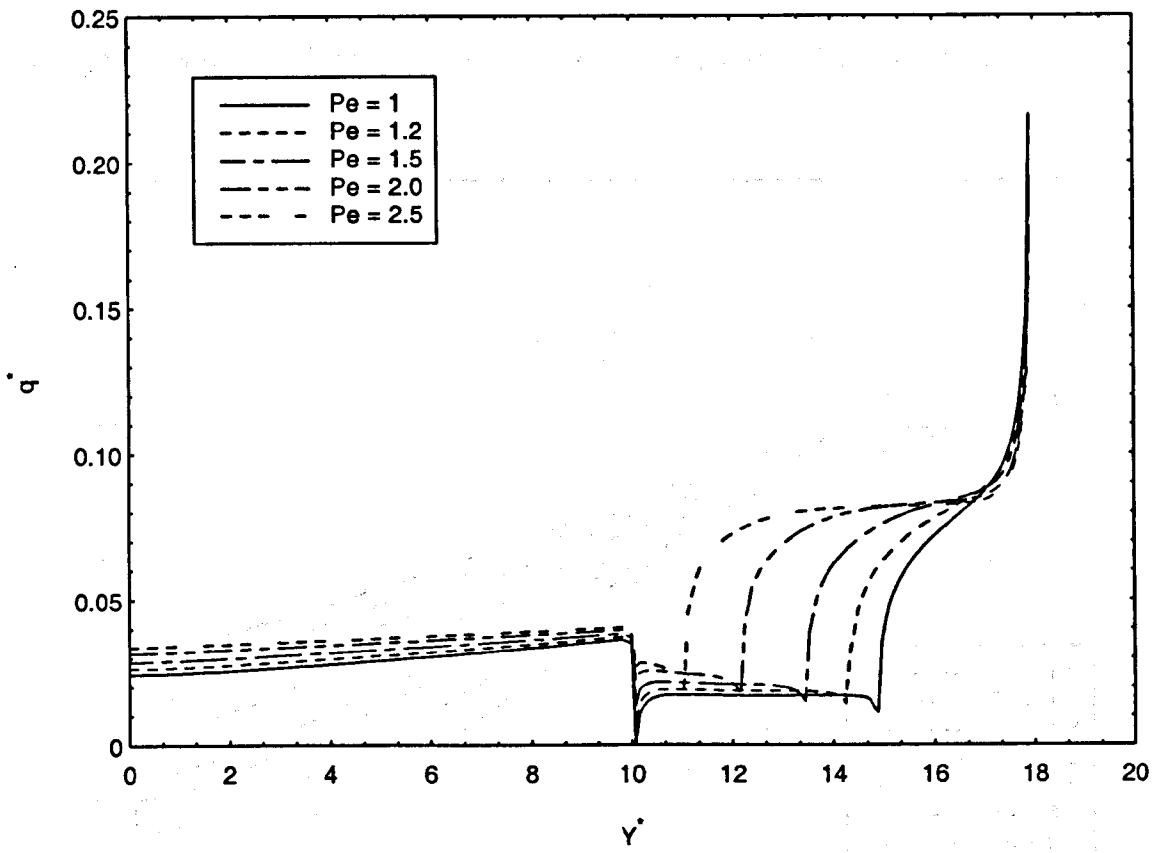

Figure 18. Effect of withdrawal speed on non-dimensional local heat flux for

$\theta_0 = 1.2$, $Bi_2 = 0.02$, $Bi_3 = 0.05$.

Figure 19 shows the variation of wall temperature versus Y^*. The slope changes abruptly at $Y^* = 18$ as a result of the change in the boundary condition from the pre-mold region ($Y^* = 18$ to 20) to the mold region ($Y^* = 10$ to 18). It can be seen from the figure that the wall temperature increases with increase in Y^*, i.e. along the upstream direction. There was a noticeable change in slope of the temperature profile at $Y^* = 10$, which indicated higher mold temperatures, again due to the increased heat resistance incurred by the air gap formation. Higher Peclet numbers lead to higher wall temperatures as

expected due to the transient nature of the problem. Therefore, it can be stated that the average temperature of the system increases with increase in Peclet number.

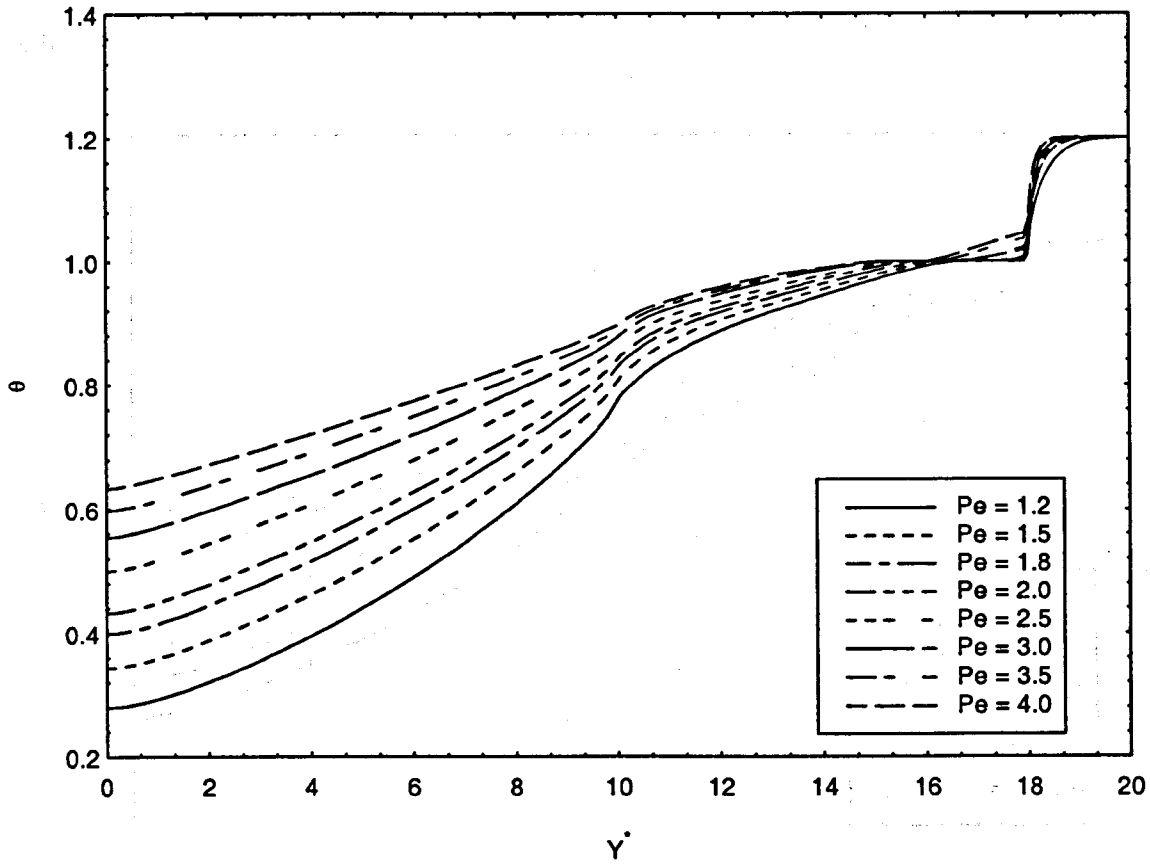

Figure 19. Effect of withdrawal speed on wall temperature for

$\theta_0 = 1.2, Bi_2 = 0.1, Bi_3 = 0.15$

Figure 20 displays the variation of centerline temperatures along the mold. As shown in the figure, an increase in Pe value increases the centerline temperature throughout the domain. The centerline temperature curves are smoother as compared to the wall temperature profiles. All the centerline temperature curves for different Peclet numbers exhibit a change in the slope in the mold region ($Y^* = 10 - 18$) at the

solidification front. In the region close to the solidification front, the phase change takes place almost isothermally. Hence, in this region, the curves tend to flatten out due to a smaller temperature differential, which explains the change in slope at the solidification front.

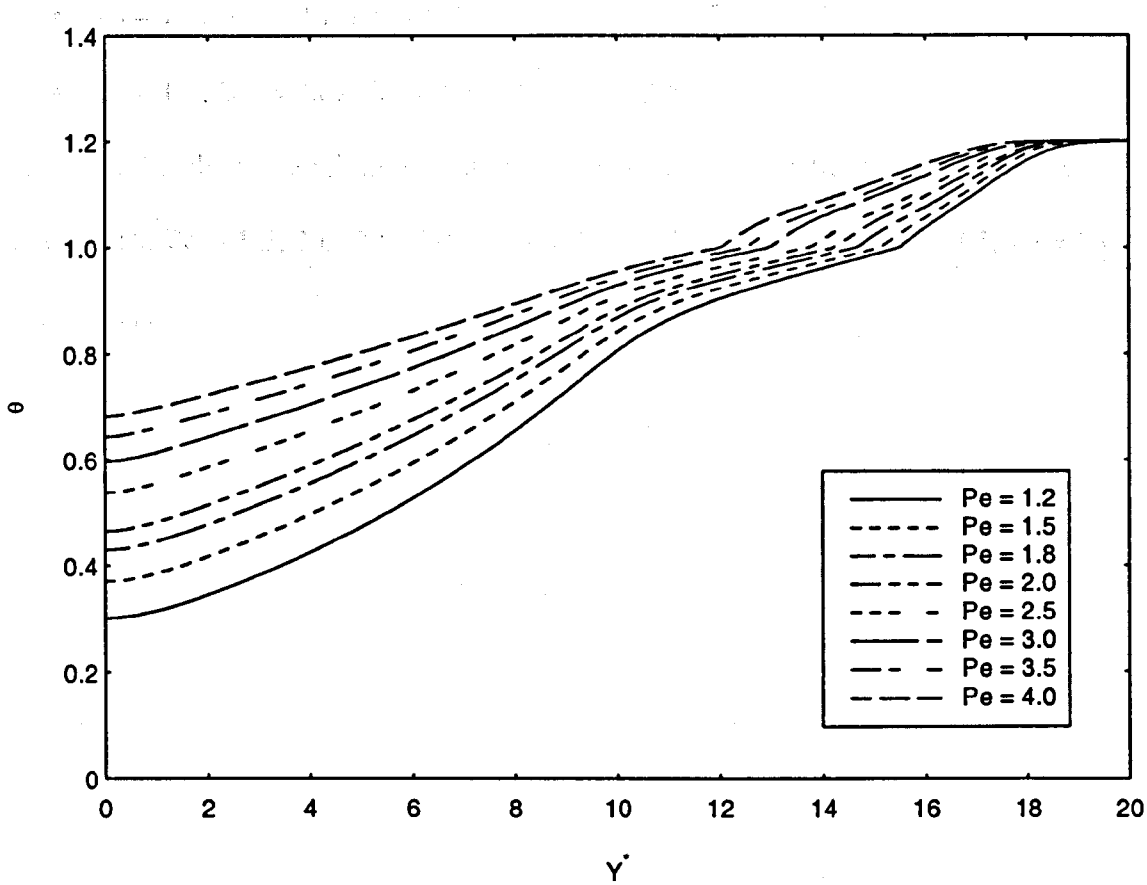

Figure 20. Effect of withdrawal speed on centerline temperature for

$\theta_0 = 1.2$, $Bi_2 = 0.1$, $Bi_3 = 0.15$

The influence of air gap formation on the metal-mold interfacial heat transfer can be better understood when the results of the cases run with and without air gap modeling were compared. The following cases were studied with and without air gap modeling:

- $\theta_0 = 1.2$, $Bi_2 = 0.1$, $Bi_3 = 0.15$, $Pe = 1.5, 2.0, 2.5, 3.0, 4.0$.
- $\theta_0 = 1.2$, $Bi_2 = 0.02$, $Bi_3 = 0.05$, $Pe = 2.0, 2.5$.

Figure 21 and 22 show the relative positions of the solidification fronts for $\theta_0 = 1.2$, $Bi_2 = 0.1$, $Bi_3 = 0.15$, $Pe = 1.5, 2.0, 2.5, 3.0, 4.0$ and $\theta_0 = 1.2$, $Bi_2 = 0.02$, $Bi_3 = 0.05$, $Pe = 2.0, 2.5$ respectively.

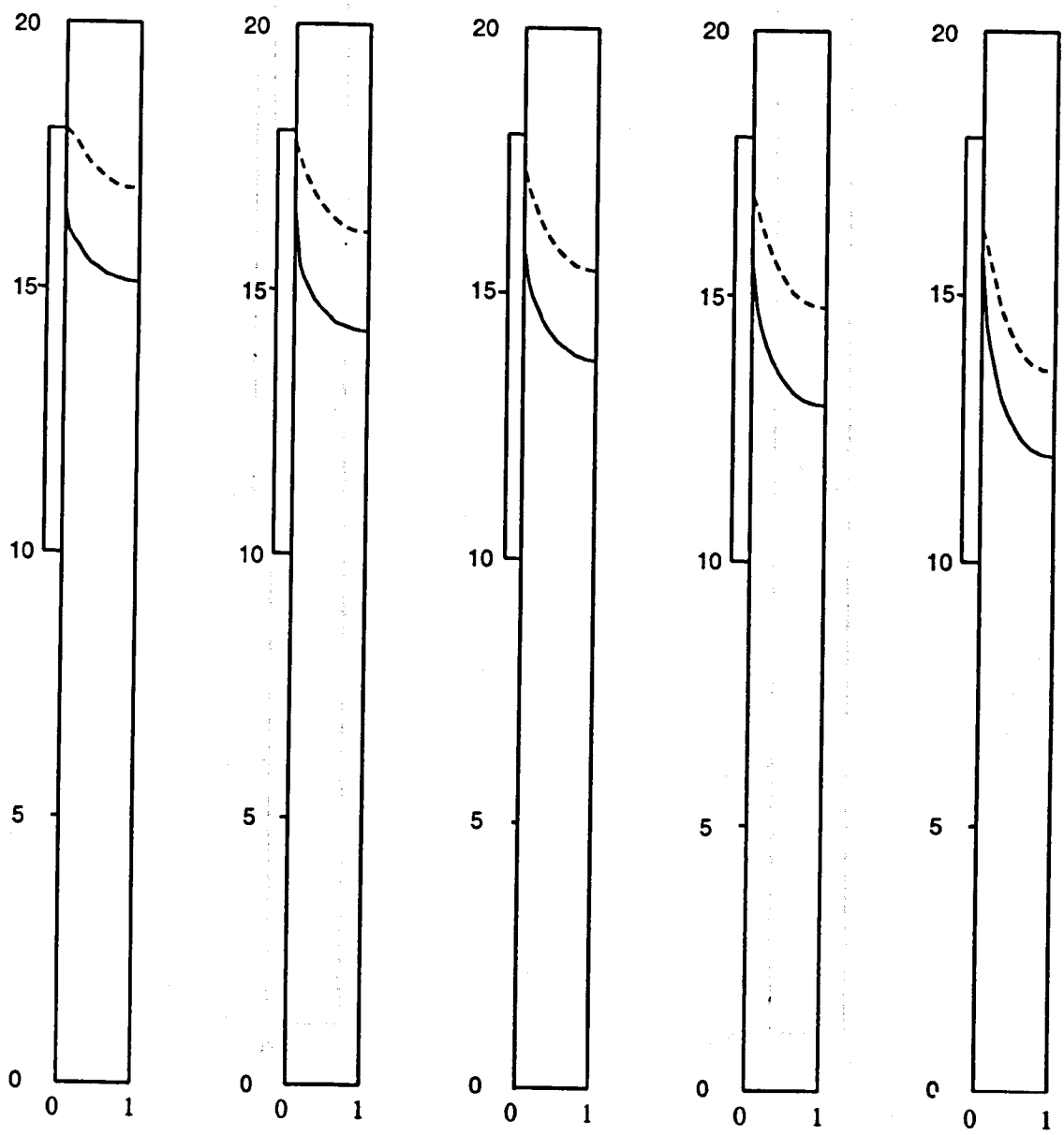

a) Pe = 1.5 b) Pe = 2.0 c) Pe = 2.5 d) Pe = 3.0 e) Pe = 4.0

Figure 21. Comparison of solidification front positions for $\theta_0 = 1.2$, $Bi_2 = 0.1$, $Bi_3 = 0.15$.

Dotted line: Without air gap modeling, Solid line: With air gap modeling

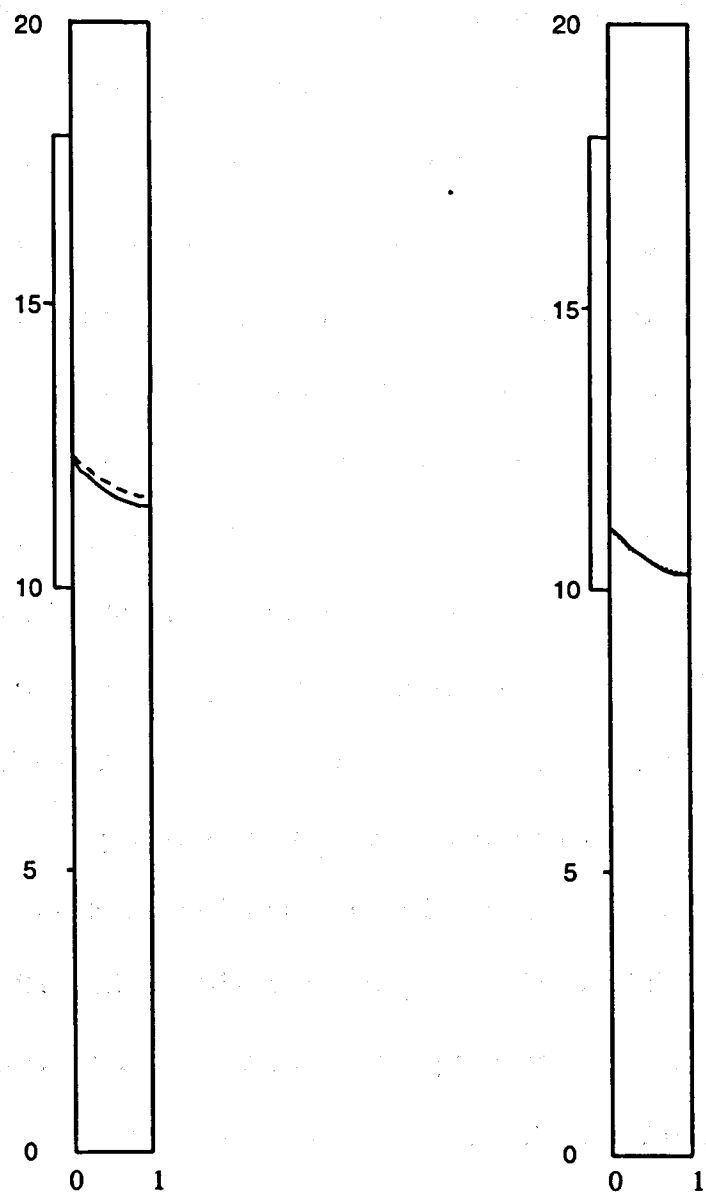

(a) Pe = 2.0 (b) Pe = 2.5

Figure 22. Comparison of solidification front positions for $\theta_0 = 1.2$, $Bi_2 = 0.02$, $Bi_3 = 0.05$

Dotted line: Without air gap modeling, Solid line: With air gap modeling

Figures 21 and 22 show the relative positions of the solidification fronts for θ_0 = 1.2, Bi_2 = 0.1, Bi_3 = 0.15, Pe = 1.5, 2.0, 2.5, 3.0, 4.0 and θ_0 = 1.2, Bi_2 = 0.02, Bi_3 = 0.05, Pe = 2.0, 2.5 respectively. In these figures, the solid lines represent the results when air gap modeling formation considered. The dotted lines in the figures are corresponding results without taking the air gap modeling into account. It is to be noted that with increase in the air gap width there is a decrease in the effective heat transfer coefficient H_{eff}. Consequently, this leads to lower thermal efficiency of the system relative to the initial cooling rate Bi_2. Lower heat extraction in the mold means hotter fluid flows through the mold. Hence the solidification front moves downstream with respect to the same cases run without air gap modeling and is demonstrated in Figure 21. It is also observed from Figure 21 that the slope of the solidification front for the cases with air gap modeling was steeper with respect to that without air gap modeling. Figures 22 (a) and (b) show the solidification fronts for Pe = 2.0 and Pe = 2.5 with lower cooling rates (θ_0 = 1.2, Bi_2 = 0.02, Bi_3 = 0.05), respectively. It can be noted that the air gap does not influence the position and the shape of the phase front significantly for the given parameters. A combination of higher withdrawal speed (Pe = 2.0, Pe = 2.5) and lower cooling rates (Bi_2 = 0.02, Bi_3 = 0.05) leads to the downstream movement of the solidification front. As the solidification front moves downstream we have less solidified metal in the mold. The area of the solidified metal in the mold is less, consequently leading to lesser shrinkage or smaller air gap width. It should be noted that the shrinkage area is directly proportional to the area of the solidified metal in the mold. In fact, as seen in Figure 22 (b) (θ_0 = 1.2, Pe = 2.5, Bi_2 = 0.02, Bi_3 = 0.05), the solidification fronts for

both, with and without air gap modeling, are almost indistinguishable. This is because as the air gap width tends to zero, the value of the non-dimensionalized heat transfer coefficient H^* approaches the Bi_2 value which is prominently demonstrated in the present cases. Therefore, it can be stated that for a given set of parameters and conditions in the study of withdrawal speed, there exists a limiting value of Pe above which the effect of air gap formation on the overall heat transfer is negligible. This is further corroborated when the local heat flux values are compared for the same cases run with and without air gap modeling. Figure 23 (a), (b) and (c) shows the comparison of local heat flux variation for cases run with and without air gap modeling for ($\theta_0 = 1.2$, $Bi_2 = 0.1$, $Bi_3 = 0.15$) Pe = 1.5, Pe = 2.5 and Pe = 4.0, respectively.

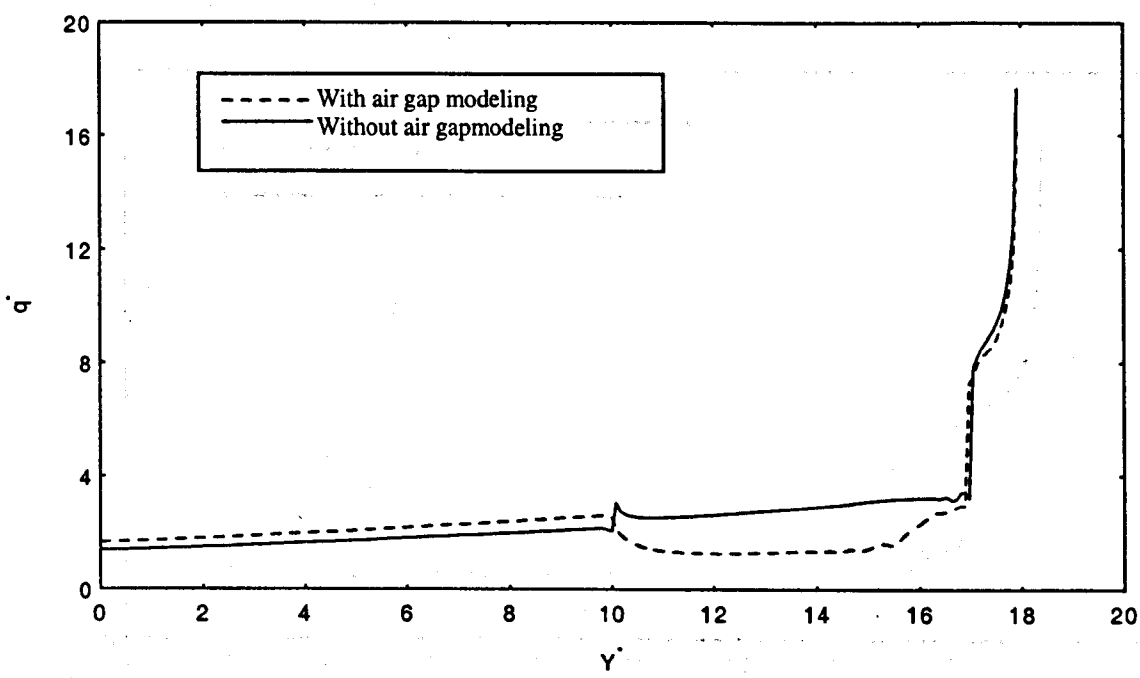

(a) Pe = 1.5

Figure 23. Comparison of local heat flux for $\theta_0 = 1.2$, $Bi_2 = 0.1$, $Bi_3 = 0.15$

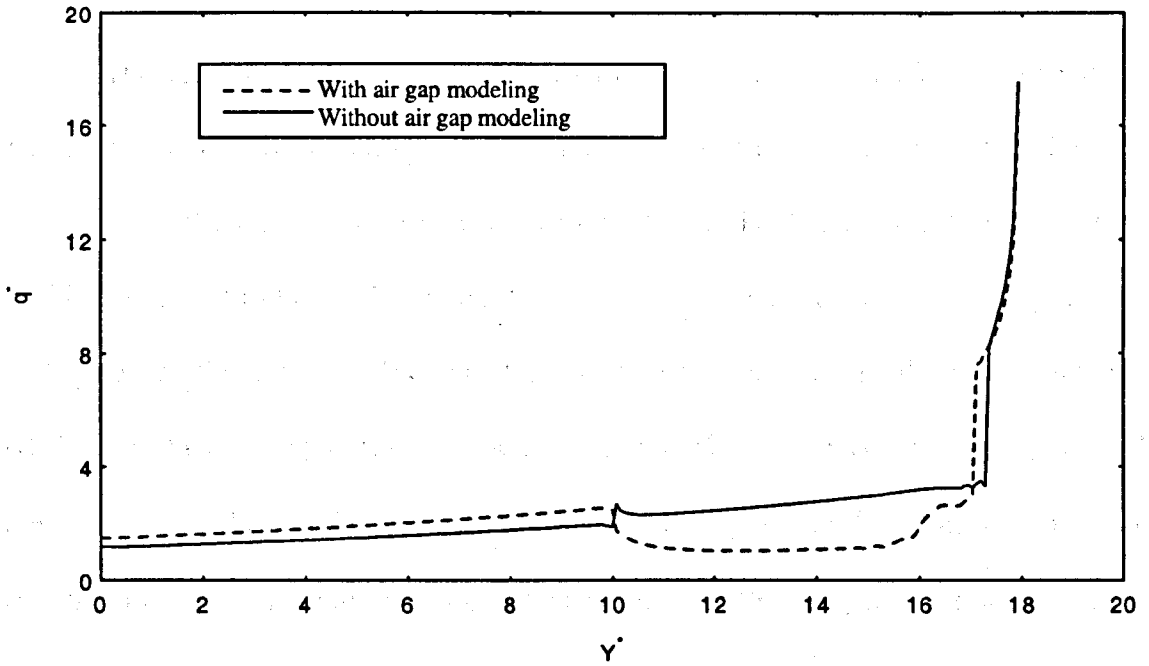

(b) Pe = 2.5

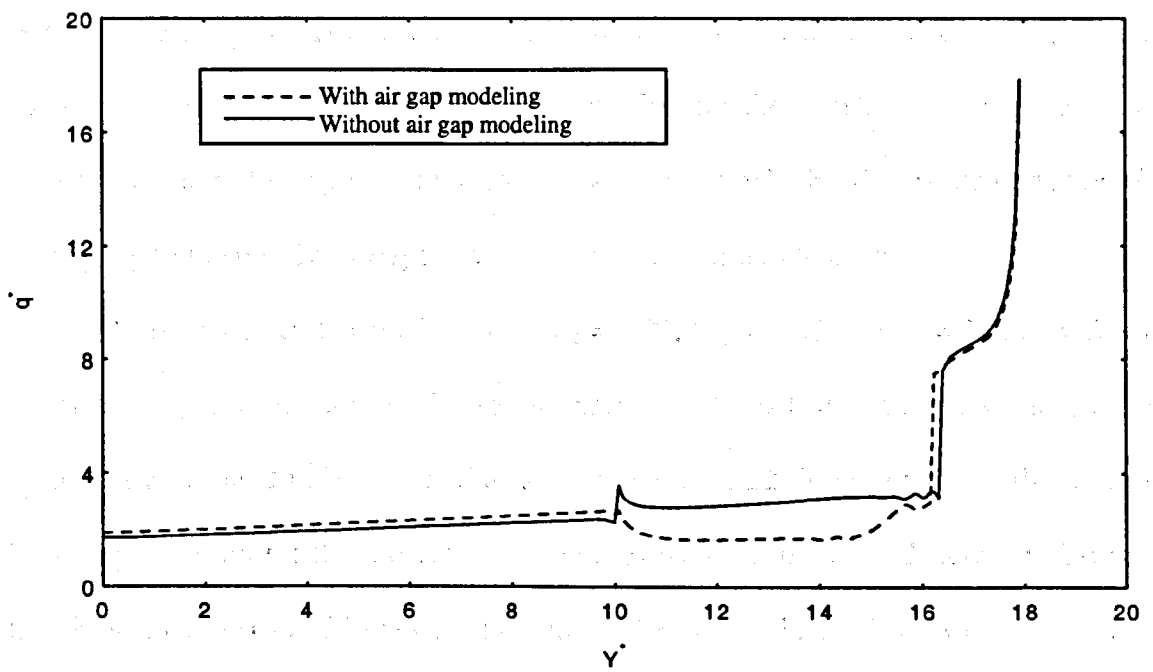

(c) Pe = 4.0

Figure 23 cont. $\theta_0 = 1.2$, $Bi_2 = 0.1$, $Bi_3 = 0.15$

The formation of the air gap leads to decreased heat transfer due to increased resistance to heat flow. This leads to higher temperatures throughout the domain as compared to the cases run without air gap modeling. Higher temperatures in the post-mold region lead to higher local heat flux for the cases with air gap modeling, as shown in Figure 23. Since the coefficient of convective heat transfer in the post mold region (Bi_3) is constant and equal for both the cases, the local heat flux is directly proportional to the temperature differential ($T - T_\infty$) at the wall in the post-mold region. It is to be noted that the ambient temperature was constant throughout the analyses (Ste = 2.5). Hence, the temperature differential ($T - T_\infty$) is higher in cases without air gap modeling because of the lesser heat extraction in the mold as well as higher post-mold temperatures as a result of the air gap. This explains the high values of local heat flux in the post-mold cooling region. A sharp drop in the local heat flux for the interfacial air gap model was seen at the point of inception of the solidification front, which exhibits the presence of an air gap, up to the mold exit beyond which the air gap ceases to exist.

As observed earlier for $\theta_0 = 1.2$, $Bi_2 = 0.02$, $Bi_3 = 0.05$ and Pe = 2.0, Pe = 2.5, the effect of air gap formation on the solidification front position with and without air gap modeling was found to be minimal as shown in Figure 22. It was expected that the local heat flux variation for the aforementioned cases would show little difference. To verify this, Figures 24 (a) and 24 (b) were plotted for the local heat flux variation for the cases, ($\theta_0 = 1.2$, Bi2 = 0.02, Bi3 = 0.05) Pe = 2.0 and Pe = 2.5, respectively.

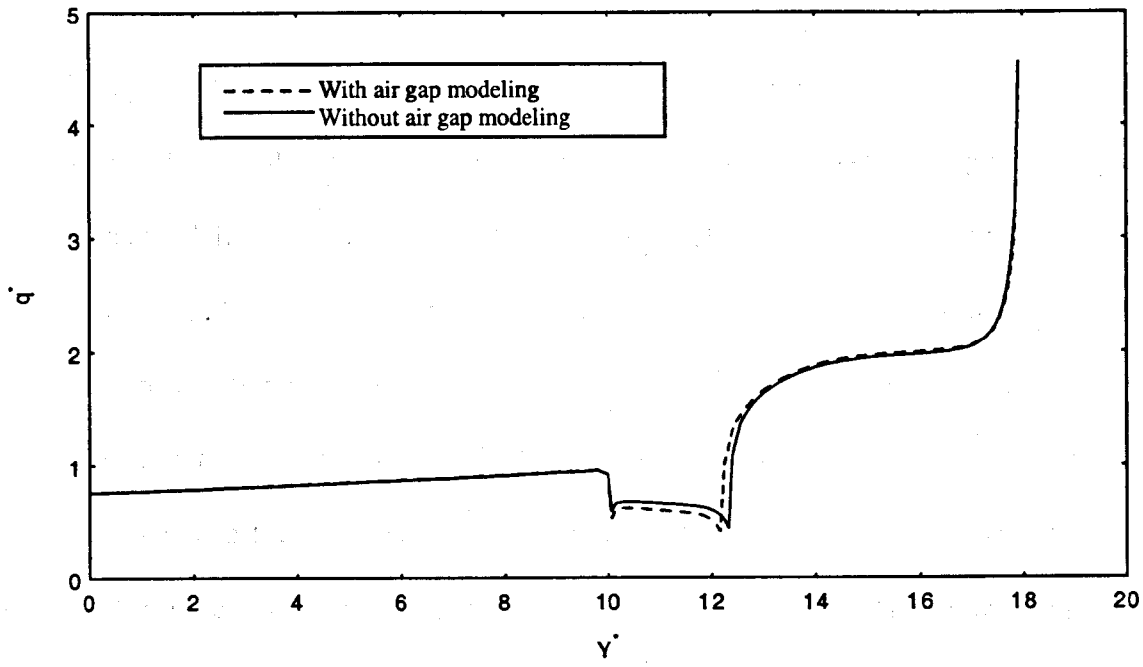

(a) Pe = 2.0

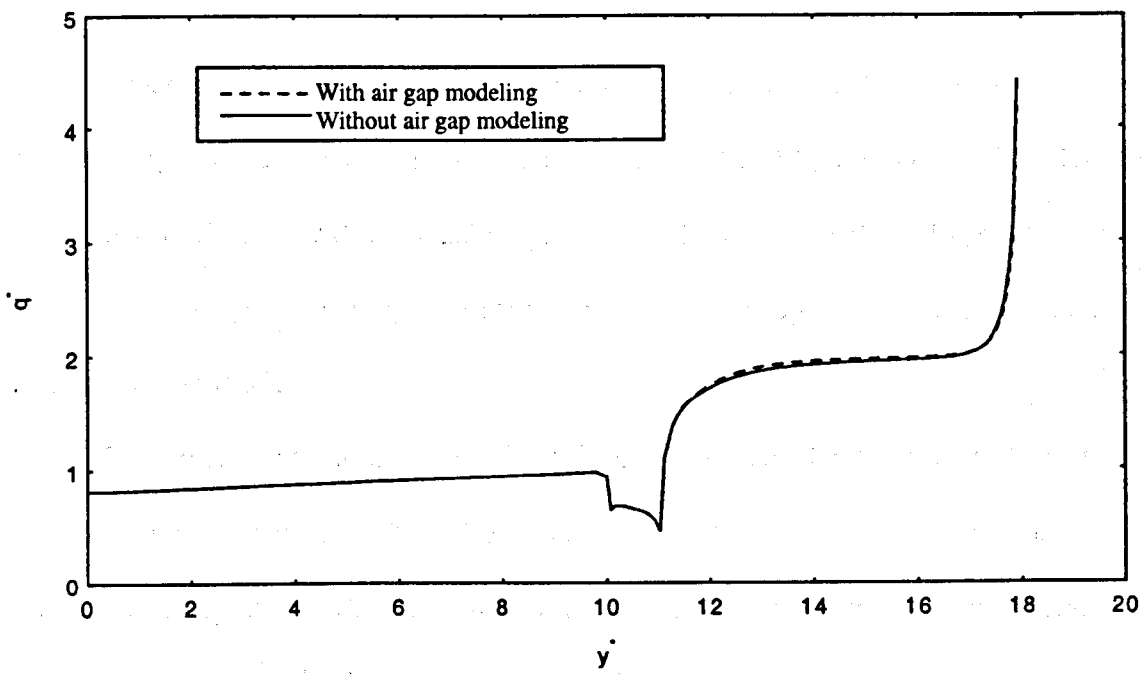

(b) Pe = 2.5

Figure 24. Comparison of local heat flux for $\theta_0 = 1.2$, $Bi_2 = 0.02$, $Bi_3 = 0.05$ for cases with and without air gap modeling.

Indeed, Figure 24 clearly demonstrates the diminishing effect of air gap with increasing Pe numbers. The local heat flux profiles for cases with and without air gap modeling are almost identical for Pe = 2.5. As explained earlier (Figure 22), a combination of low cooling rates and high withdrawal speeds leads to less metal to be solidified in the mold. This leads to smaller air gap width or less heat resistance, as the shrinkage is directly proportional to the area of the solidified metal in the mold. Consequently, there is little difference between the cases run with and without the air gap modeling as regards the heat transfer as seen by the local heat flux variation in Figure 24. Therefore, the process parameters for the cases (θ_0 = 1.2, Bi_2 = 0.02, Bi_3 = 0.05 and Pe = 2.0, Pe = 2.5) can be considered as the limiting variables for the current study as far as the effect of withdrawal speed is concerned. Figure 25 (a) and (b) shows the overall non-dimensional heat flux for θ_0 = 1.2, Bi_2 = 0.1, Bi_3 = 0.15, Pe = 1.2, 1.5, 1.8, 2.0, 2.5, 3.0, 3.5, 4.0 and θ_0 = 1.2, Bi_2 = 0.02, Bi_3 = 0.05, Pe = 2.0, Pe = 2.5 respectively. The diamond shaped symbol represents cases with air gap modeling whereas the rectangle shaped symbol represents cases without air gap modeling.

The overall non-dimensional heat flux was obtained by numerically integrating the local non-dimensional heat flux values over the mold wall. Simpsons rule of numerical integration was adopted for numerical integration. The overall non-dimensional heat flux is always higher for analyses without air gap modeling. The air gap formation hampers the heat transferred from the metal to the mold thereby reducing the heat extraction efficiency of the mold. In cases without air gap modeling, the average

heat flux is representative of the maximum ideal heat flux that can exist for the given set of parameters. Hence, even if the air gap formed is smal,l it still offers some resistance to heat flow resulting in a lower value of overall heat flux for the case with air gap modeling. As observed in Figure 25 (b) for $\theta_0 = 1.2$, $Bi_2 = 0.02$, $Bi_3 = 0.05$ and Pe = 2.0, Pe = 2.5 the difference between the values of the overall heat flux with and without air gap modeling was small because the air gap formed had a minimal effect on the solidification front positions as well as the heat flux variation. It can be recalled that similar trend was observed in Figures 22 and 24.

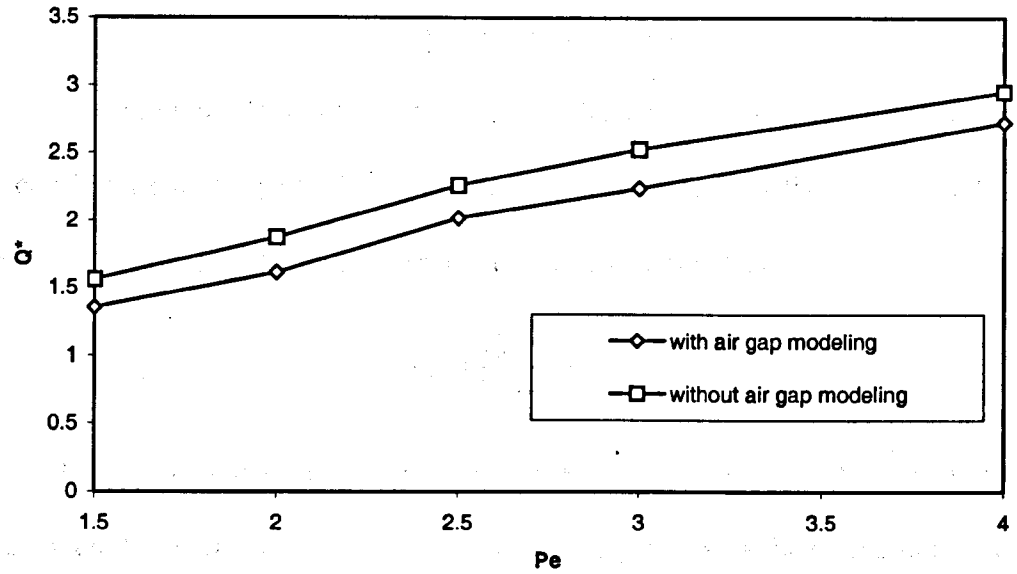

(a) $\theta_0 = 1.2$, $Bi_2 = 0.1$, $Bi_3 = 0.15$

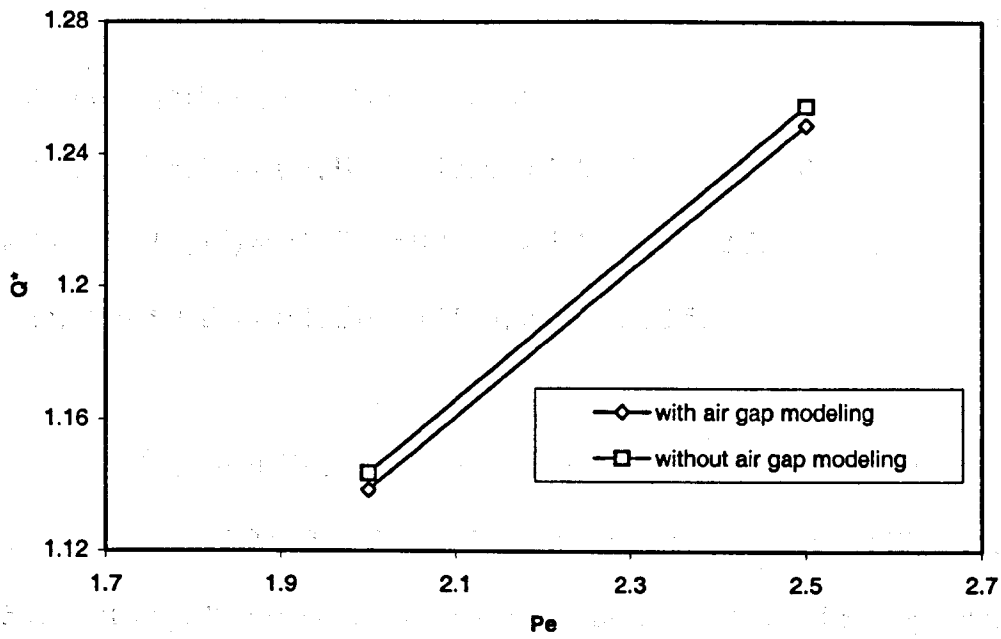

(b) $\theta_0 = 1.2$, $Bi_2 = 0.02$, $Bi_3 = 0.05$

Figure 25. Average non-dimensional heat flux versus Peclet number with and without air gap modeling.

Effect of Superheat

The molten metal is heated to a particular temperature before it is passed through the continuous casting mold. This temperature is known as the superheat temperature. Superheat is given by the parameter, θ_0, which was defined as

$$\theta_0 = \frac{T_0 - T_\infty}{T_s - T_\infty} \tag{5.13}$$

Increasing the superheat increases the inlet temperature, thereby increasing the time taken for solidification, whereas decreasing the superheat drastically may cause freezing of the liquid at the shrouds. Hence the process entails the liquid metal to be poured at optimum superheat temperature.

Following were the input parameters for the numerical analysis to study the effect of superheat with air gap modeling:

Case (a) Pe = 1.5, Bi_2 = 0.1, Bi_3 = 0.15, θ_0 = 1.2, 1.5, 2.0, 2.5, 3.0

Case (b) Pe = 2.0, Bi_2 = 0.1, Bi_3 = 0.15, θ_0 = 1.2, 1.5, 2.0, 2.5.

Case (c) Pe = 3.0, Bi_2 = 0.1, Bi_3 = 0.15, θ_0 = 1.2, 2.0, 2.5.

Three different withdrawals speeds were employed, and the superheat values ranged from 1.2 to 3.0. The cooling rates were kept constant at Bi_2 = 0.1 and Bi_3 = 0.15 respectively. It is seen that the degree of superheat affects the temperature profiles, heat flux, solidification front position and the shell thickness at the mold exit. Figures 26 (a), (b) and (c) show the solidification front locations for Cases (a), (b) and (c) respectively.

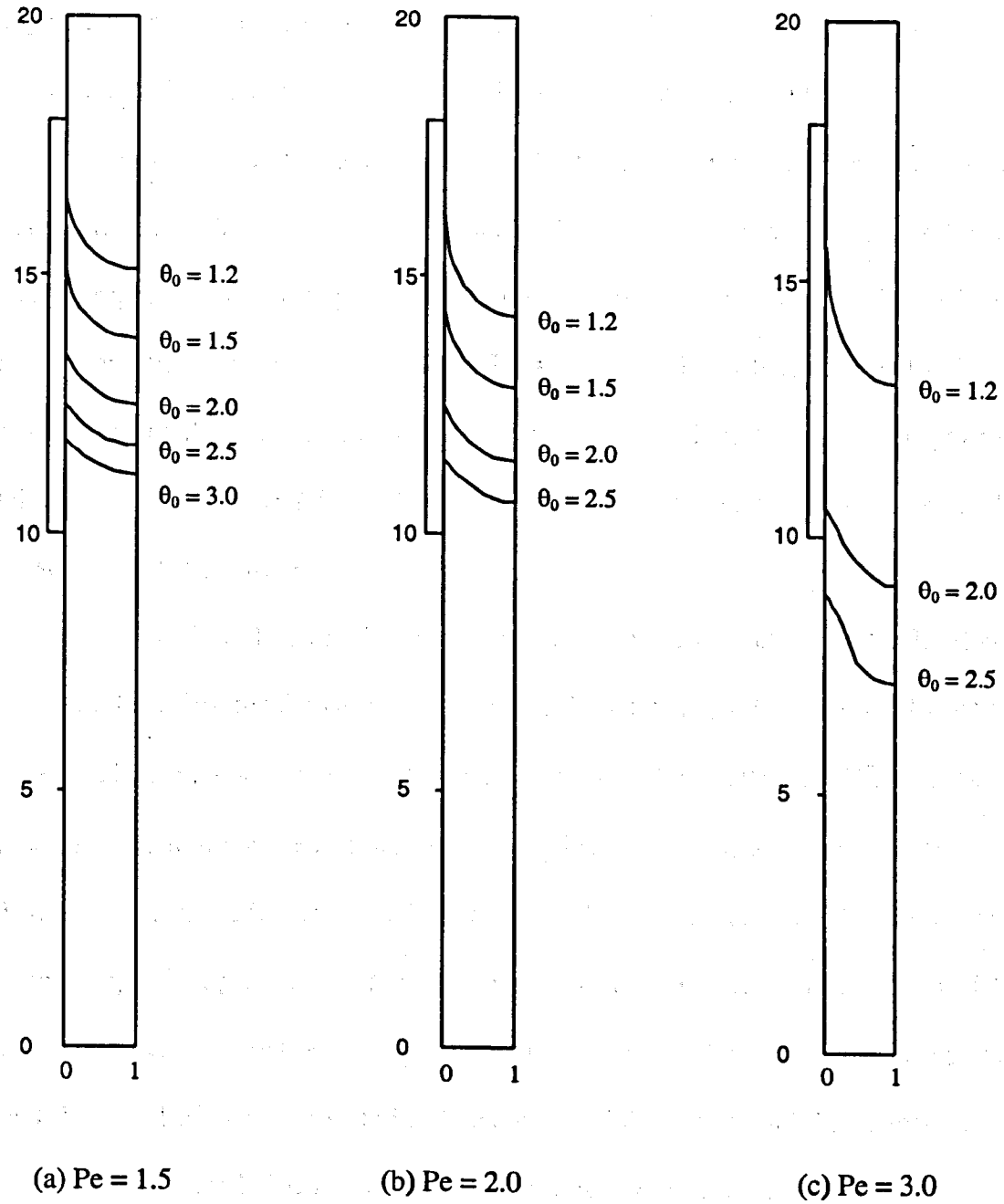

Figure 26. Effect of superheat on the location of solidification front for different Peclet numbers ($Bi_2 = 0.1$, $Bi_3 = 0.15$).

For the same cooling rates and withdrawal speed, as the superheat increases, the average temperature of the system increases and the solidification front moves downstream. With increase in the withdrawal speed, the solidification fronts move further downstream as expected. The amount of superheat convected downstream is higher for higher values of θ_0. The shape of the solidification front does not change significantly except for higher withdrawal speeds, where the front is steeper as seen in Figure 26 (c). Breakout condition was observed for Pe = 2.5 at $\theta_0 = 2.5$, $Bi_2 = 0.1$, $Bi_3 = 0.15$, despite high values of cooling rates. Thus for the given system, it is not advisable to pour the metal at Pe = 2.5 and $\theta_0 = 2.5$. For higher Peclet numbers the metal should be poured at lower superheat temperature.

As evident from Figure 27, the air gap had a considerable effect on the local non-dimensional heat flux for the case with $\theta_0 = 1.2$, Pe = 1.5, $Bi_2 = 0.1$, $Bi_3 = 0.15$. At this superheat value, the non-dimensional effective heat transfer coefficient, H^*, was 2×10^{-2}, i.e., the decrease in the value of Bi_2 due to air gap heat resistance was by about 80%. This lead to a drastic reduction in local heat flux which was due to a combination of low withdrawal speed, superheat and high cooling rates. This is because (As seen in Figure 26), the solidification front moves upstream with lower withdrawal speed and superheat ($\theta_0 = 1.2$, Pe = 1.5), which results in higher value of the area of solidified metal in the mold. It is to be noted that metal shrinkage is directly proportional to the area of the solidified metal in the mold. Consequently, more shrinkage leads to higher values of air gap width resulting in a drastic drop in local heat flux. This effect was also observed for the same superheat value at a higher Peclet number (Pe = 2.0) and can be seen in Figure

28. The maximum local heat flux was observed for the highest superheat value for the case with $\theta_0 = 3.0$, Pe = 1.5, $Bi_2 = 0.1$, $Bi_3 = 0.15$ and $\theta_0 = 2.5$, Pe = 2.0, $Bi_2 = 0.1$, $Bi_3 = 0.15$ respectively and can be seen in Figures 27 and 28 respectively.

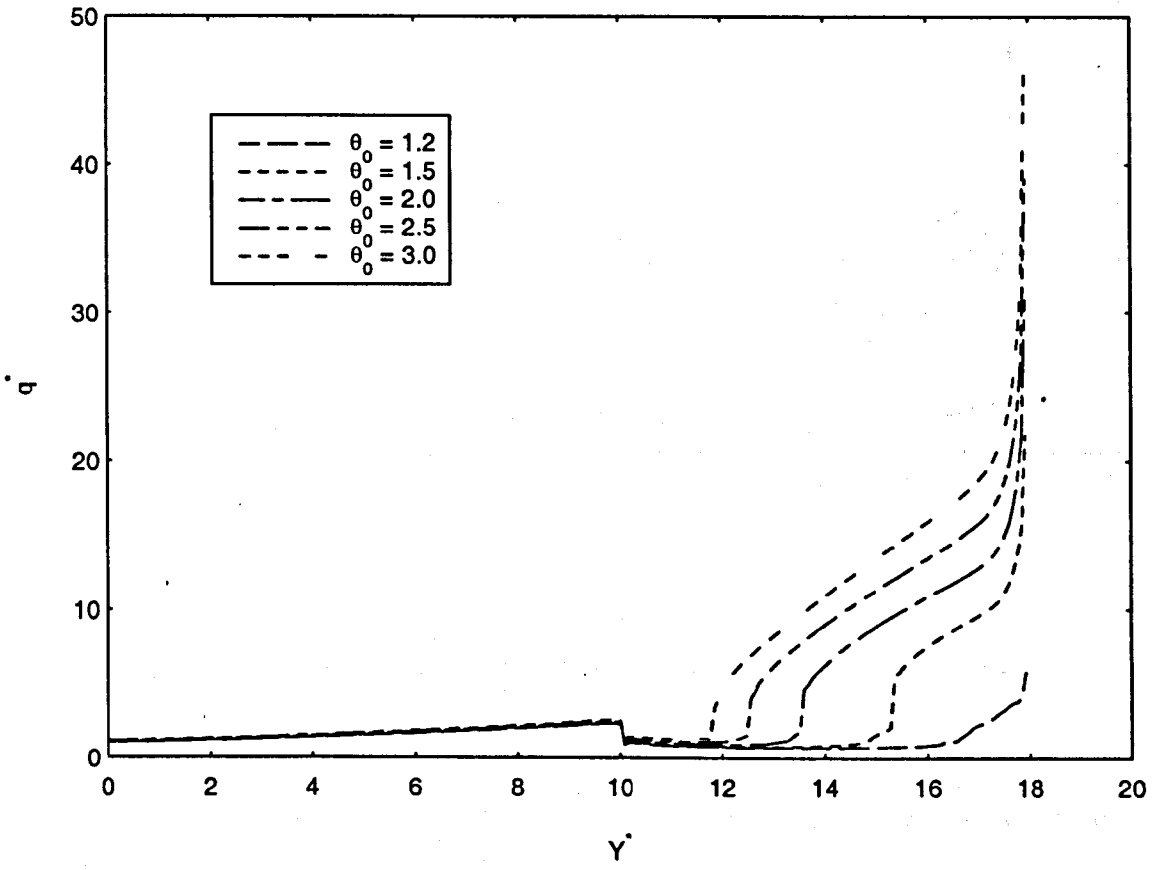

Figure 27. Variation of local heat flux for different superheats for

Pe = 1.5, $Bi_2 = 0.1$, $Bi_3 = 0.15$

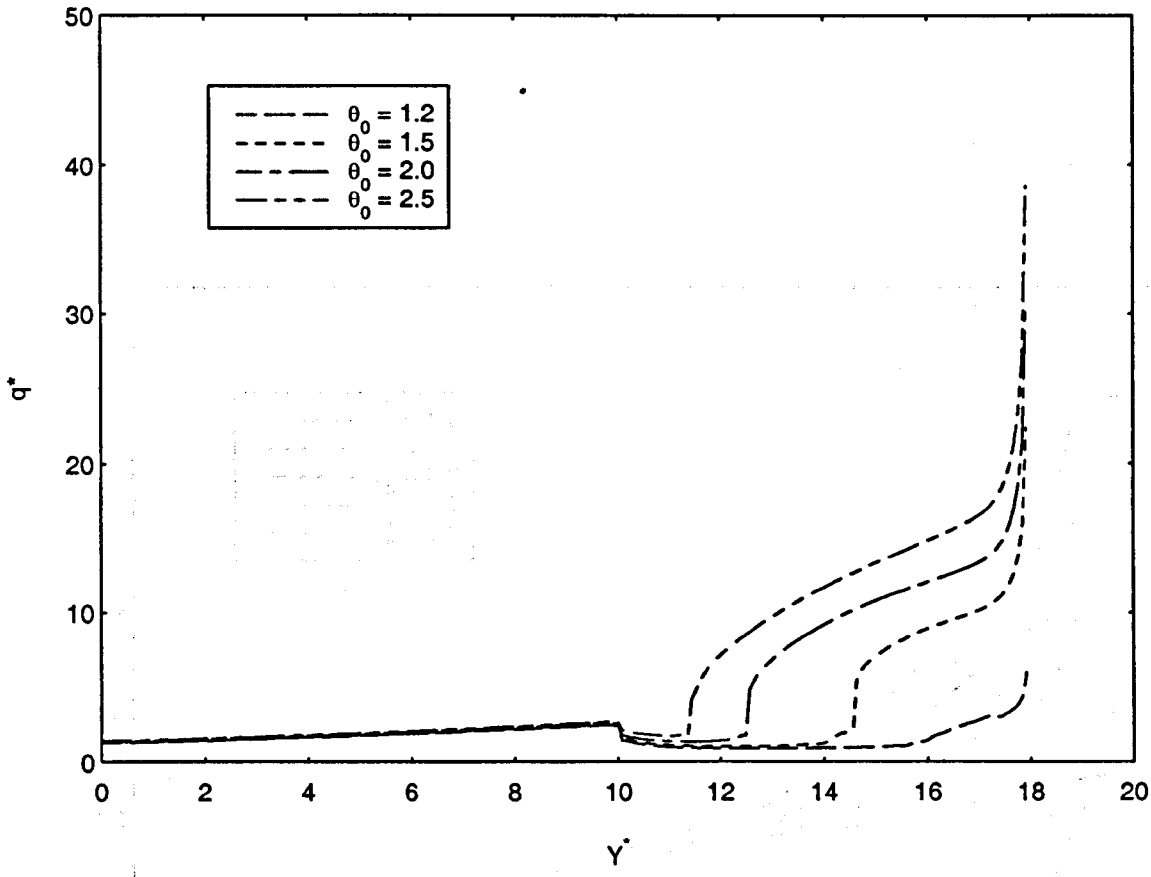

Figure 28. Variation of local heat flux for different superheats for

$Pe = 2.0, Bi_2 = 0.1, Bi_3 = 0.15.$

With increase in the superheat, higher heat flux values were observed throughout the domain, which indicates that more heat is extracted in the mold and the post-mold region, despite air gap heat resistance. The wall temperature in the post mold region as well as the mold region also increases with increase in superheat temperature leading to higher temperature difference with respect to the ambient temperature, thus leading to higher local heat flux values. Figures 29 and 30 show the wall and centerline temperature variation throughout the domain respectively.

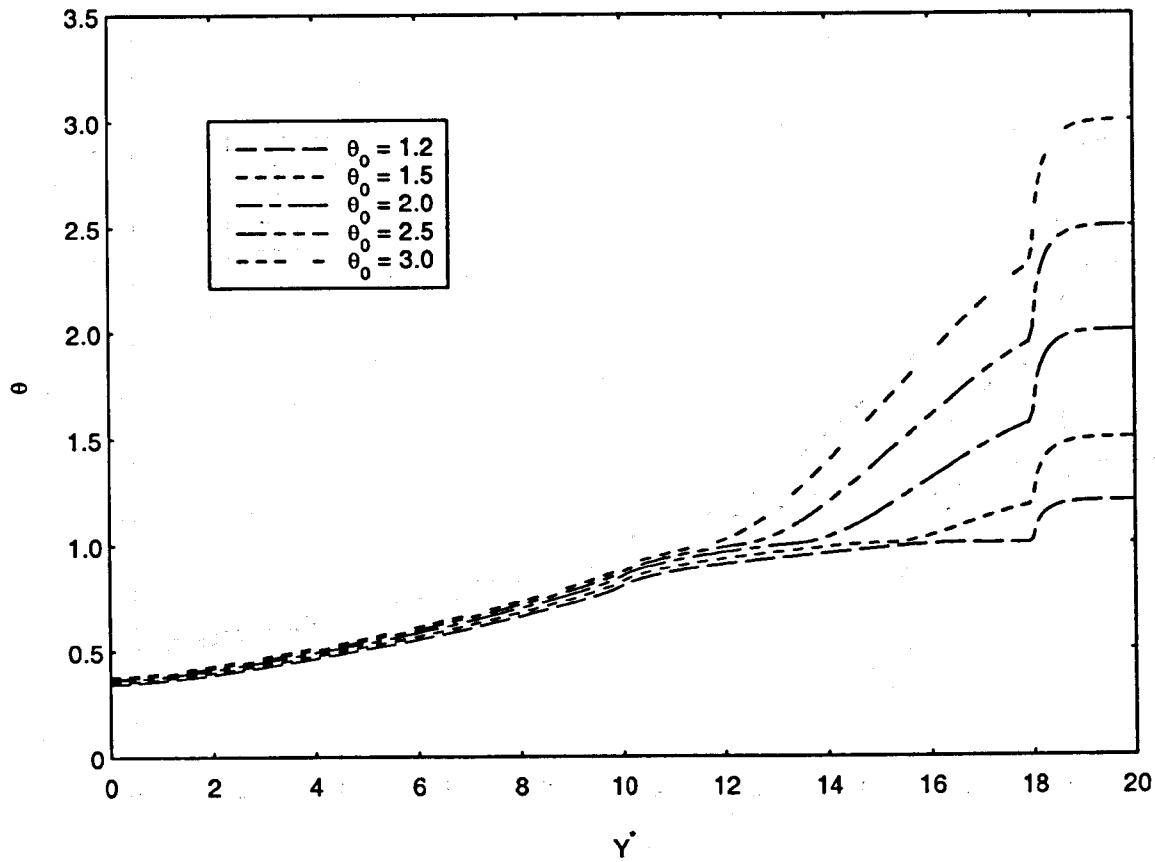

(a) Pe = 1.5, $Bi_2 = 0.1$, $Bi_3 = 0.15$

Figure 29. Wall temperature profiles for different superheat values

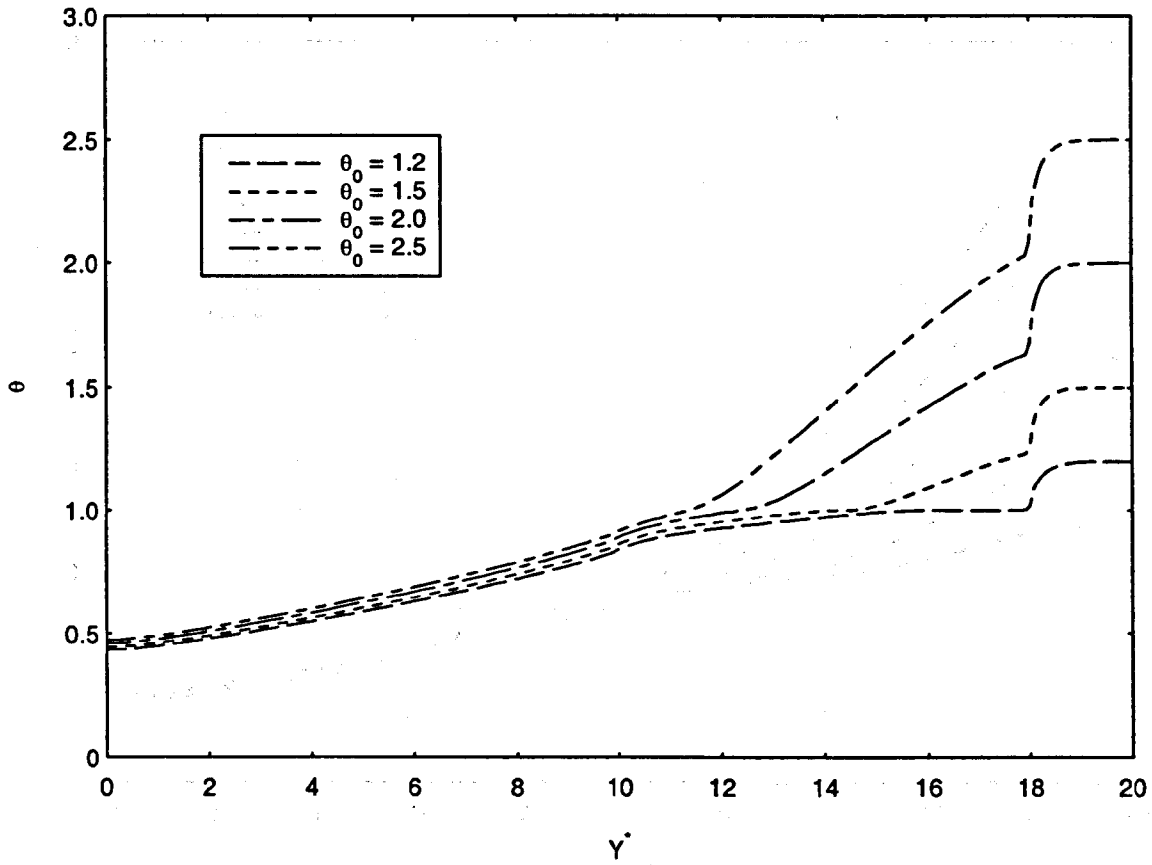

(b) Pe = 2.0, $Bi_2 = 0.1$, $Bi_3 = 0.15$

Figure 29 contd. Wall temperature profiles for different superheat values.

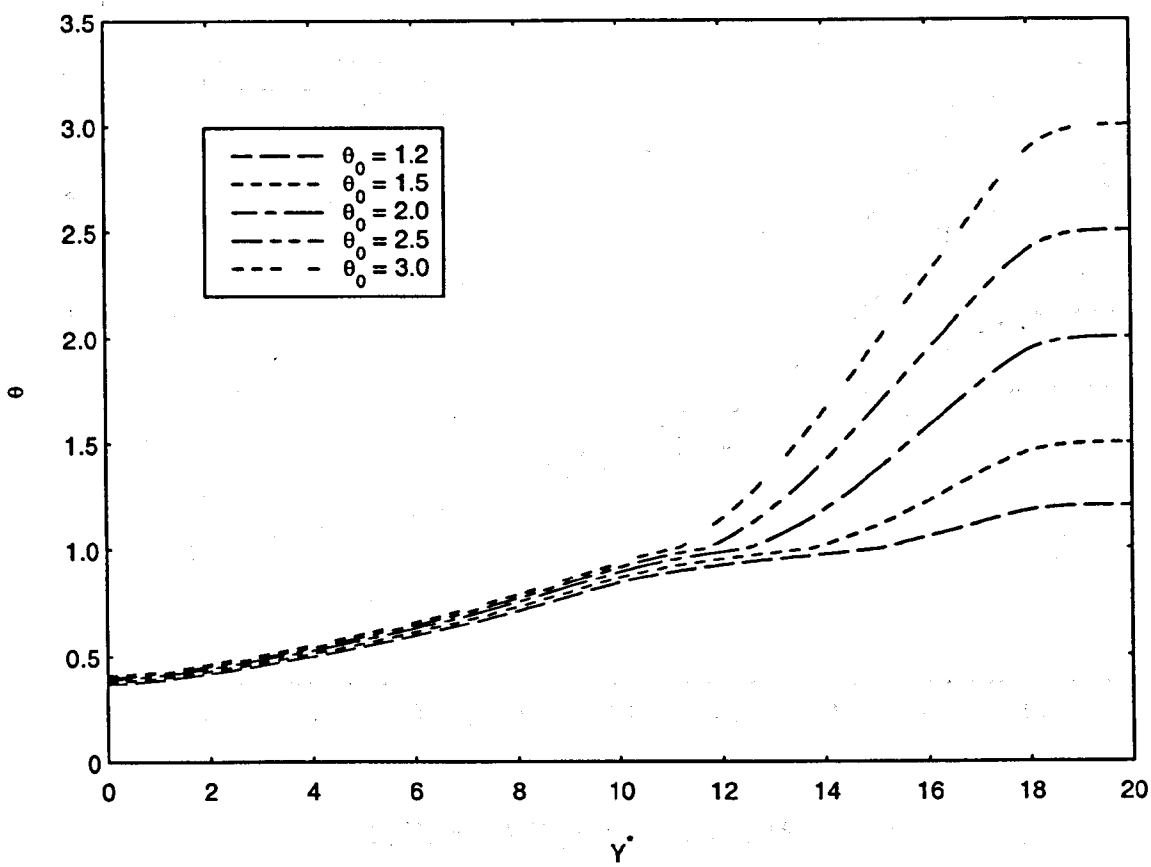

(a) Pe = 1.5, $Bi_2 = 0.1$, $Bi_3 = 0.15$

Figure 30 Centerline temperature profiles for different superheat values

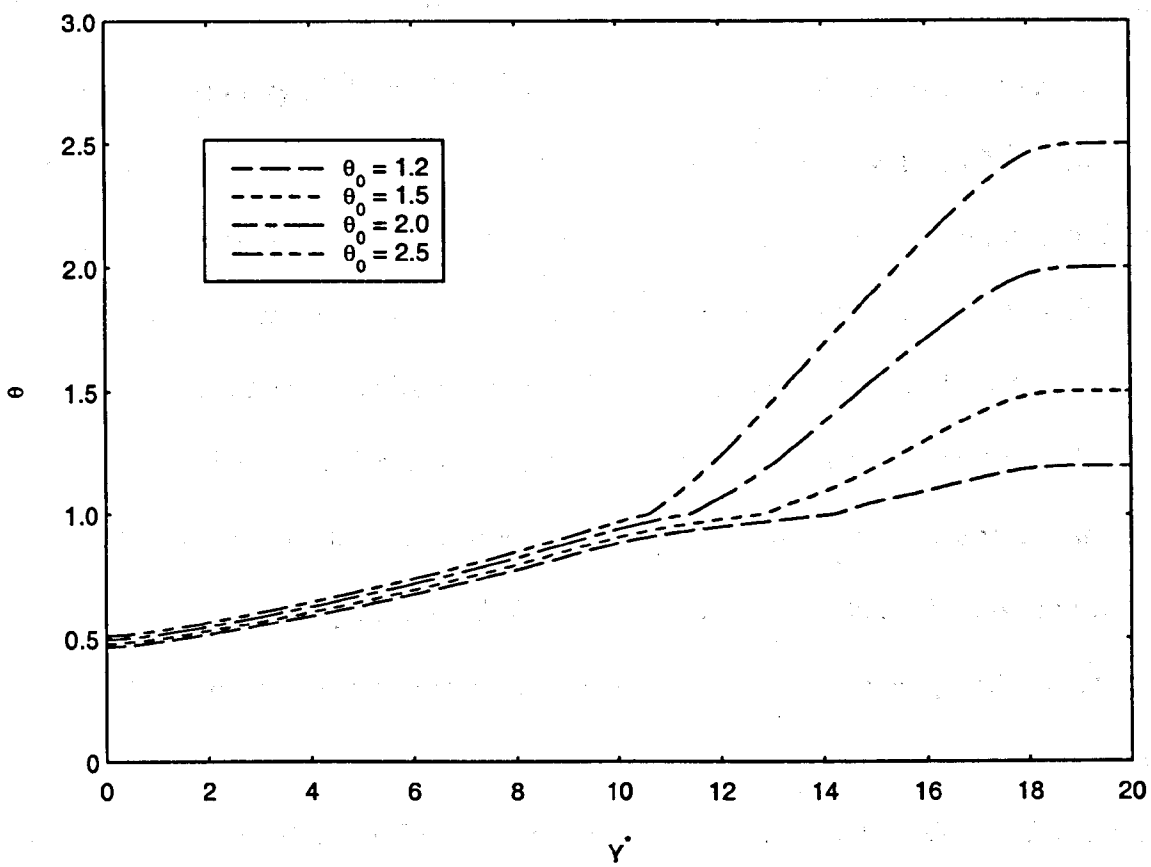

(b) Pe = 2.0, $Bi_2 = 0.1$, $Bi_3 = 0.15$

Figure 30 contd. Centerline temperature for different superheat values

The wall and centerline temperatures are higher for higher superheat and the temperature profiles exhibit a typical behavior. The pre mold region ($Y^* = 18 - 20$) is insulated and hence the temperature gradient is zero. In the downstream direction, (from $Y^* = 20$ towards $Y^* = 0$), the wall temperature almost remains constant from $Y^* = 20$ to $Y^* = 18$ until the entry of the mold ($Y^* = 18$), where it suddenly drops due to axial heat conduction. The metal undergoes cooling in the mold area ($Y^* = 18$ to $Y^* = 10$) and hence the temperature profile shows a constant decrease till the solidification front location. There is a change in the slope at this point and the curve flattens out in the rest of the mold till the metal exits the mold. This is the region where the latent heat is removed and is the reason for more or less a constant temperature profile. Latent heat of fusion is defined as the amount of heat that must be removed when there is a change of phase of a unit mass of liquid to solid. During solidification, the latent heat is removed at constant temperature which explains the constant temperature profile near the solidification front in the mold region. Once the metal exits the mold, it is subjected to convective heat transfer resulting in a constant decrease in the slope of the wall temperature profile. Therefore to summarize, it can be said that higher superheat results in higher wall temperature and consequently leads to higher heat flux. The centerline temperature profile is of prime importance as the centerline temperature determines the metallurgical length. Metallurgical length is the vertical length of the solid shell from the meniscus to the point where the solidification front intersects the axis. This length determines the torch cutoff point for the given parameters in continuous casting.

Knowing the metallurgical length is important to prevent breakouts. The centerline temperature shows a similar behavior to wall temperature profile except for the fact that the drop in the temperature at the entry of the mold region ($Y^* = 18$) is less abrupt. The change in slope is observed at the mold entry, solidification front location and the mold exit.

Figure 31 shows the effect of superheat on the percent decrease in the mold cooling rate Bi_2. The percent decrease in mold cooling rate is given by:

$$\% \text{ Decrease in } Bi_2 = \left(\frac{Bi_2 - H^*}{Bi_2}\right) \times 100 \tag{5.14}$$

This parameter gives an estimate of the decrease in the heat extraction in the mold due to heat resistance incurred by the air gap. As observed earlier, increase in superheat value results in the downstream movement of the solidification front which leads to lesser area of solidified metal in the mold. This leads to air gap of smaller width, as shrinkage is directly proportional to the area of the solidified metal in the mold. Smaller air gap offers less resistance to heat flow and as the air gap width goes on decreasing the value of the non-dimensional effective heat transfer coefficient, H^*, goes on increasing. It can be observed that the percent decrease in Bi_2 is zero if there is no air gap, i.e. if H^* is equal to Bi_2 in equation (5.14). Therefore, it can be seen in Figure 31 that the value of the parameter, percent decrease in Bi_2, decreases with increase in superheat irrespective of different withdrawal speeds. For the ranges of parameters investigated in the present study, the decrease in Bi_2 value ranged from 65 to 79 % for Pe = 1.5 and 49 to 70 % for Pe = 2.0. In their work for transient metal-mold interfacial heat transfer coefficient,

Nishida and Matsubara (1976) have reported a decrease in heat transfer coefficient of more than 50 % for ingot mold castings.

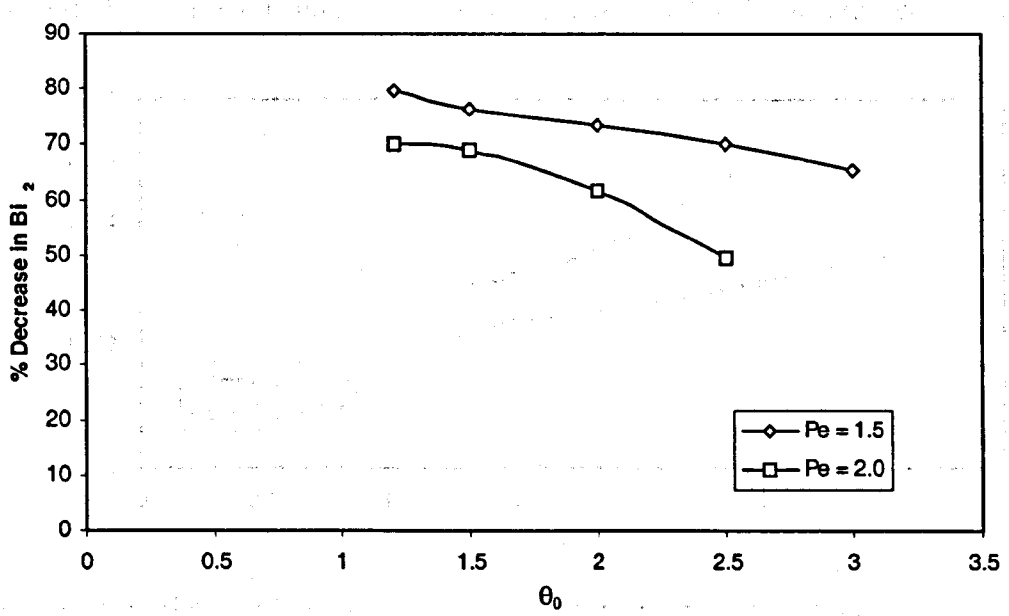

Figure 31. Effect of superheat on the percent decrease in Bi_2 for

$Pe = 1.5, 2.0, Bi_2 = 0.1, Bi_3 = 0.15.$

The variation of the non-dimensional effective heat transfer coefficient, H^*, and the non-dimensional air gap width, G^*, is shown in Figures 32 and 33 respectively. It was found that H^* increases with increase in the superheat whereas G^* decreases with increase in superheat. Increasing superheat decreases the air gap width, G^* as stated earlier and decreasing air gap width leads to increase in the effective heat transfer coefficient H^*. In the present study, the value of H^* increased by 41 % with increase in superheat from $\theta_0 = 1.2$ to $\theta_0 = 3.0$ for $Pe = 1.5$, $Bi_2 = 0.1$, $Bi_3 = 0.15$ and it increased by 68 % with increase in superheat from $\theta_0 = 1.2$ to $\theta_0 = 2.5$ for $Pe = 2.0$, $Bi_2 = 0.1$, $Bi_3 = 0.15$. It was also noted

that an air gap of a few micrometer width had a profound effect on the heat transfer. As shown in Figure33, the non-dimensional air gap width varied from 6.4×10^{-4} to 2.5×10^{-3}, which in dimensional from represents widths from 0.64 to 2.5 μm respectively.

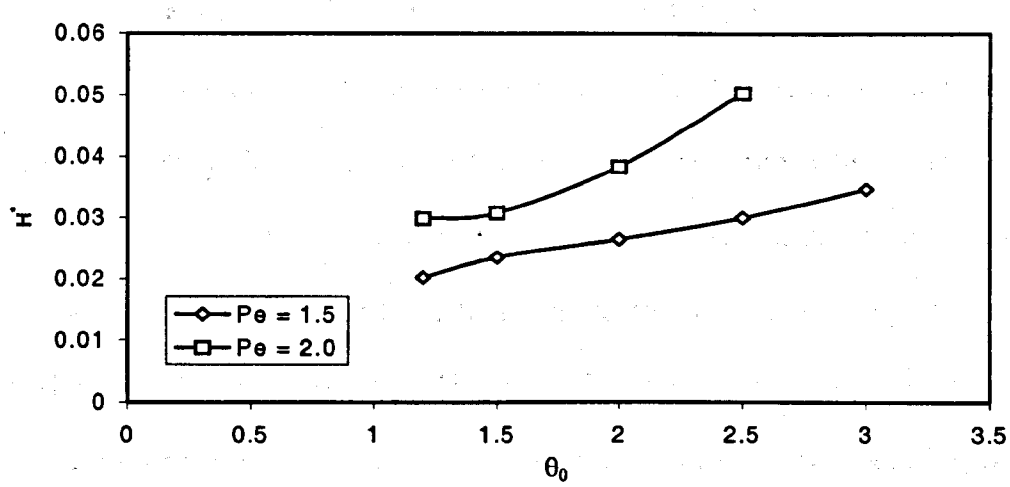

Figure 32. Variation of non-dimensional effective heat transfer coefficient with superheat for Pe = 1.5, 2.0,Bi_2 = 0.1, Bi_3 = 0.15

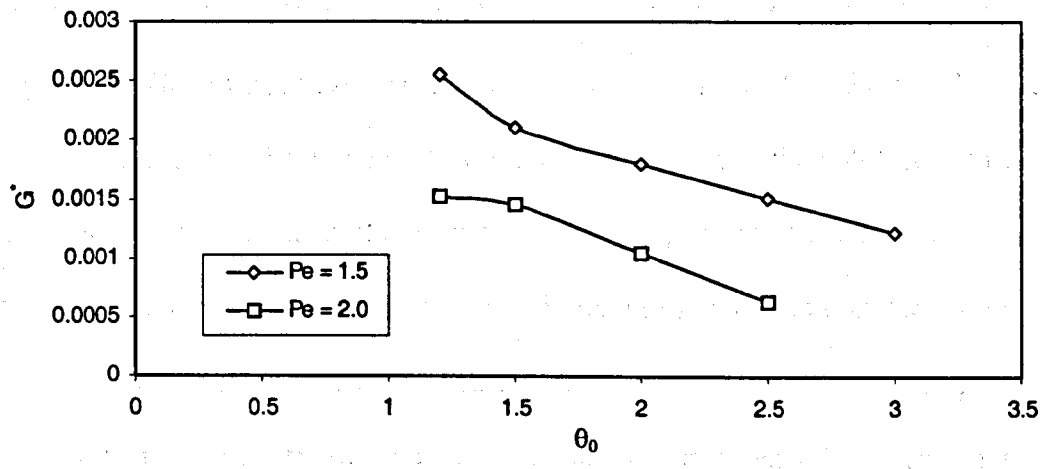

Figure 33. Variation of non-dimensional air gap width with superheat for Pe = 1.5, 2.0,Bi_2 = 0.1, Bi_3 = 0.15

In order to further investigate the effects of air gap formation, the following cases were run with and without air gap modeling:

- $Pe = 1.5$, $Bi_2 = 0.1$, $Bi_3 = 0.15$, $\theta_0 = 1.2, 3.0$
- $Pe = 2.0$, $Bi_2 = 0.1$, $Bi_3 = 0.15$, $\theta_0 = 1.2, 2.5$

Figure 34 shows the solidification front location for the above cases. Dashed line represents the solidification front for the respective cases run without air gap modeling whereas the solid line represents the solidification front for air gap modeling. As seen in Figure 34, the effect of air gap formation is more prominent at low superheat value ($\theta_0 = 1.2$) [Figures 34 (a) and (c)]. The solidification front is significantly displaced downstream for the air gap modeling with respect to the cases without air gap modeling. The difference between the front locations with and without air gap considerably decreases with increase in superheat [Figure 34 (b) and (d)]. Therefore, it can be stated that the effect of air gap formation on the heat transfer is less significant with increase in superheat. This is because, the area of the solidified metal in the mold decreases with increase in the superheat due to downstream movement of the solidification front. Again, less solid metal in the mold means smaller air gap, as there is a direct relationship between the shrinkage and the solid metal area in the mold as dictated by equation (4.4). It would be expected that if the solid metal area in the mold was comparatively small leading to negligibly small air gap width then the difference between the solidification front positions for the model with and without air gap modeling would be negligible.

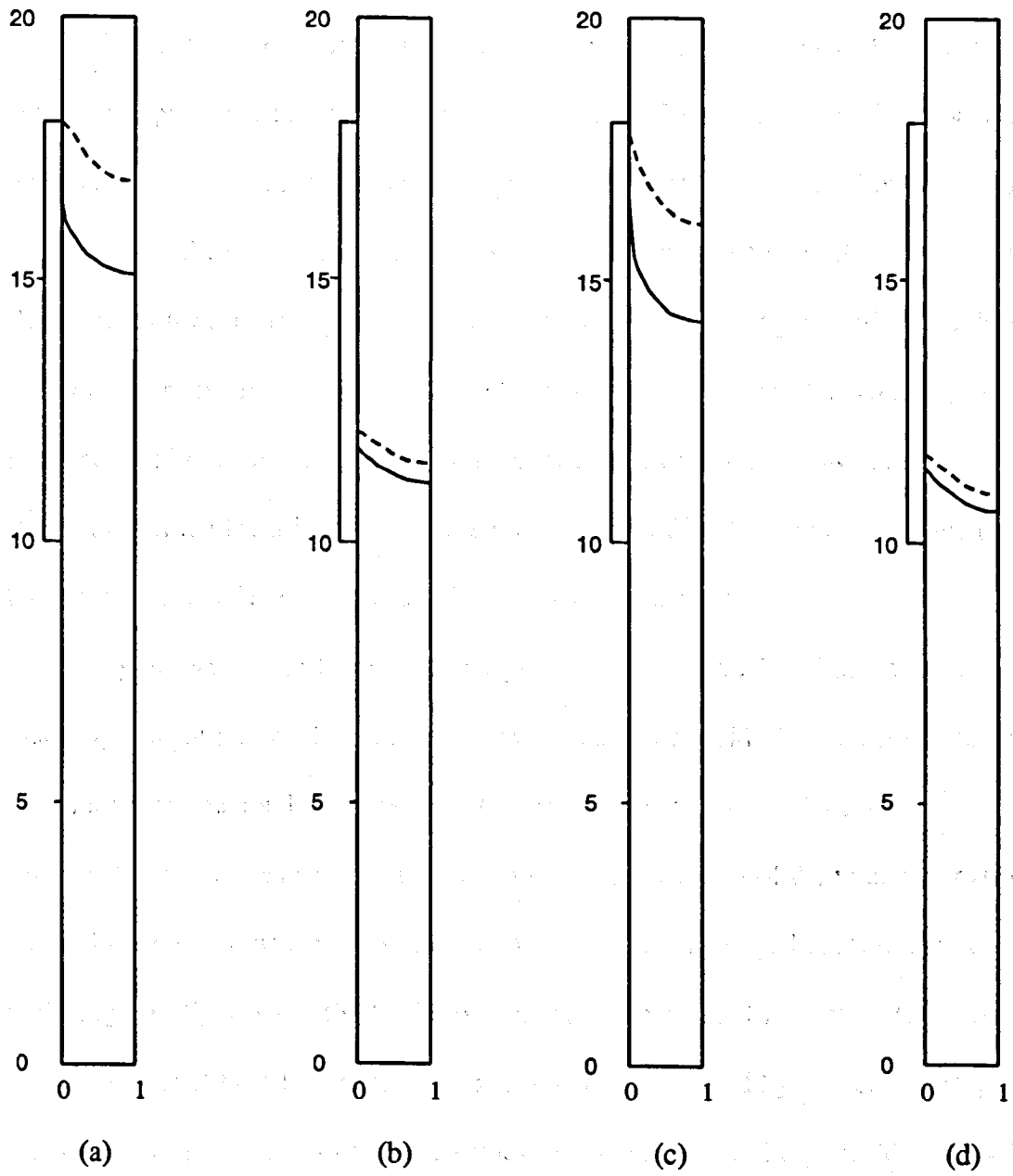

Figure 34. Comparison of solidification front positions with and without air gap modeling for $Bi_2 = 0.1$, $Bi_3 = 0.15$. (a) $Pe = 1.5$, $\theta_0 = 1.2$, (b) $Pe = 1.5$, $\theta_0 = 3.0$, (c) $Pe = 2.0$, $\theta_0 = 1.2$, (d) $Pe = 2.0$, $\theta_0 = 2.5$, Dotted line: Without air gap modeling, Solid line: With air gap modeling

Thus, it can be summarized that with increase in superheat, the air gap model behavior approaches the model without air gap modeling in terms of the heat transfer rate. This was confirmed when the non-dimensional local heat flux profile for the aforementioned cases was observed. As seen in Figures 35(b) and 35 (d), the local heat flux profiles for the air gap model as well as those without air gap modeling exhibit little difference for higher superheat values. On the contrary, Figures 35 (a) and (c) display the prominent effect of the air gap on the local heat flux variation at low superheat values. A sharp drop in the local heat flux in the mold region ($Y^* = 10 - 18$) can be seen which is the typical effect of the resistance to heat flow by the air gap.

By observing the local heat flux profiles in Figures 27 and 28, it can be deduced that a significant part of the total heat is extracted in the mold. To corroborate this fact the percentage of the total heat extracted in the mold was plotted against corresponding superheat temperatures and can be seen in Figure 36. Percent of the total heat extracted in the mold is defined as the ratio of the non-dimensional average heat flux extracted in the mold region ($Y^* = 10 - 18$) to the overall non-dimensional heat flux, Q^*. The average non-dimensional heat flux in the mold region was evaluated by numerical integration of the non-dimensional local heat flux values only over the mold region ($Y^* = 10 - 18$). As defined earlier, the overall non-dimensional heat flux Q^* was obtained from integrating the non-dimensional local heat flux values over the mold and the post mold region along

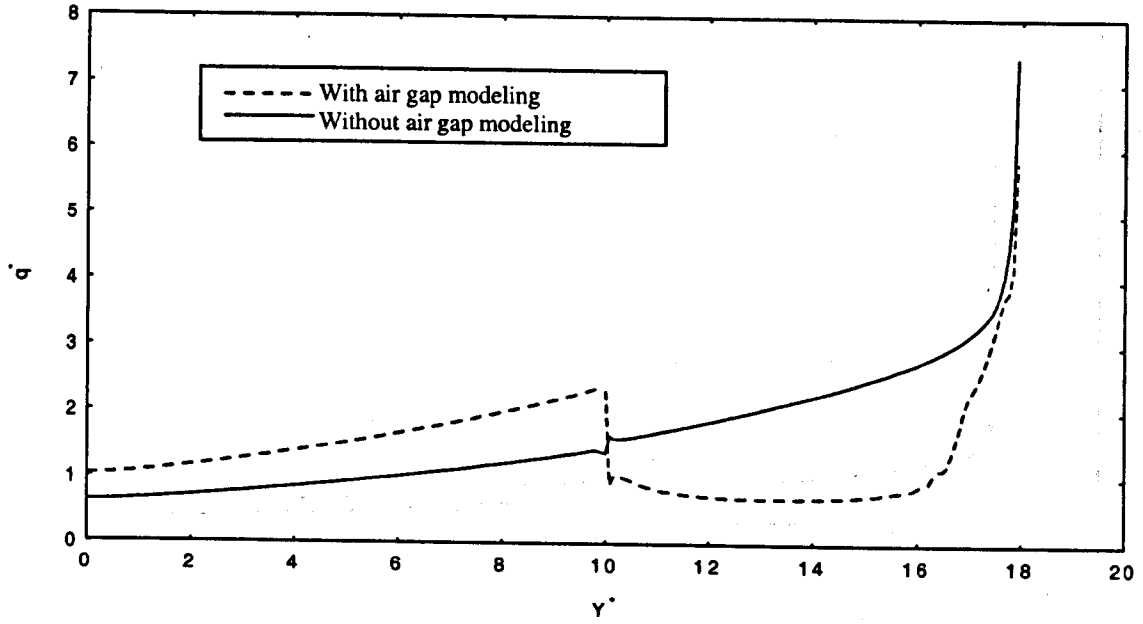

(a) $\theta_0 = 1.2$

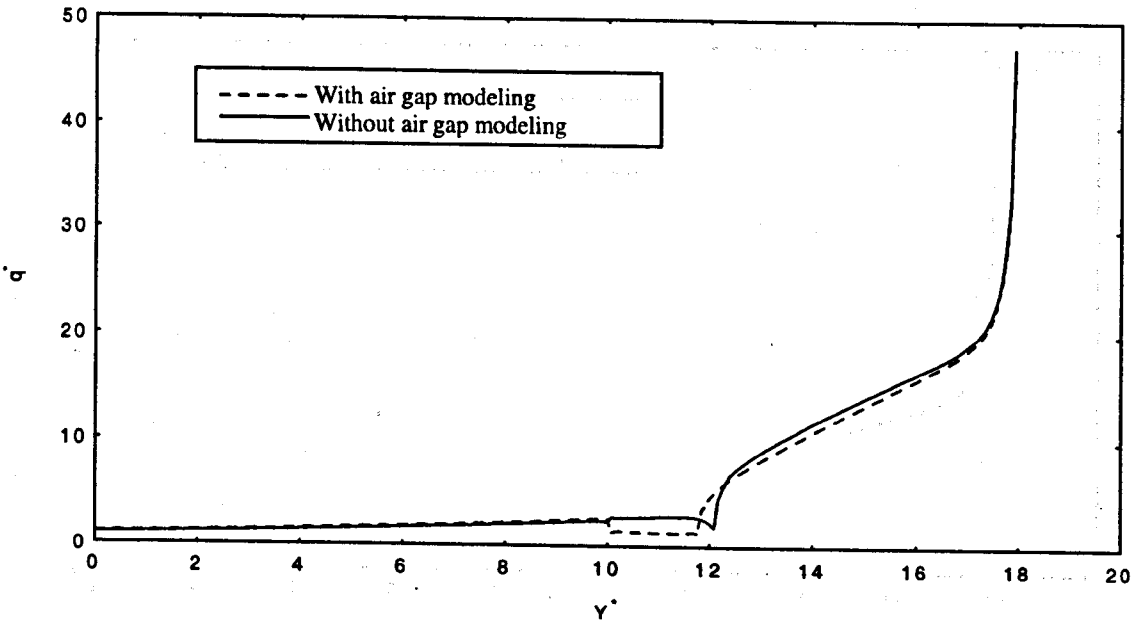

(b) $\theta_0 = 3.0$

Figure 35. Comparison of local heat flux profiles at different superheat values for Pe = 1.5, $Bi_2 = 0.1$, $Bi_3 = 0.15$ for cases with and without air gap modeling.

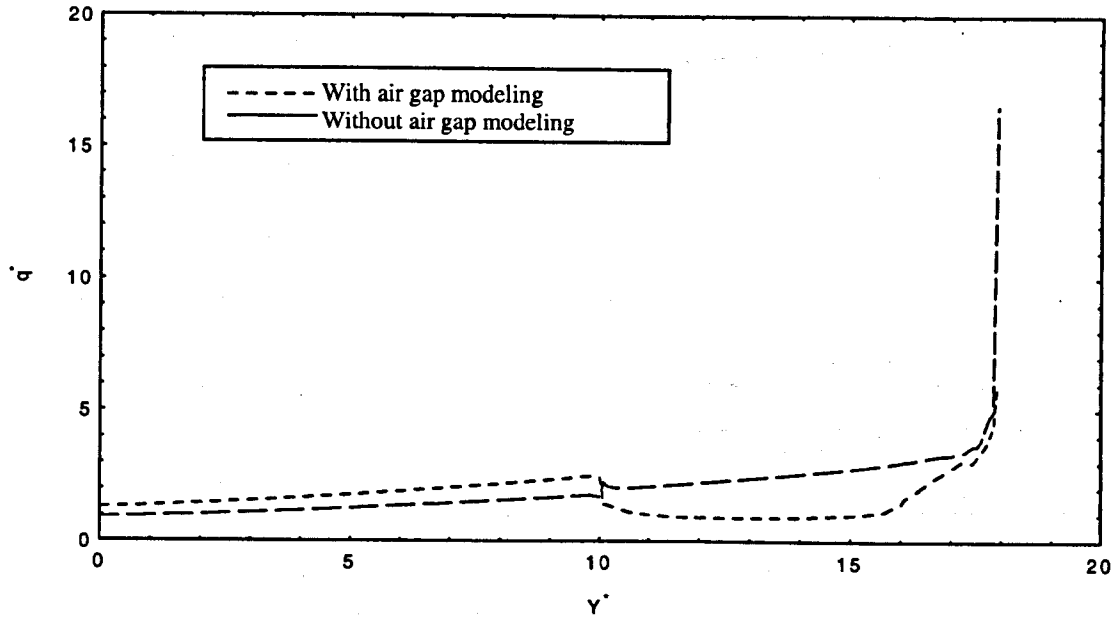

(c) $\theta_0 = 1.2$

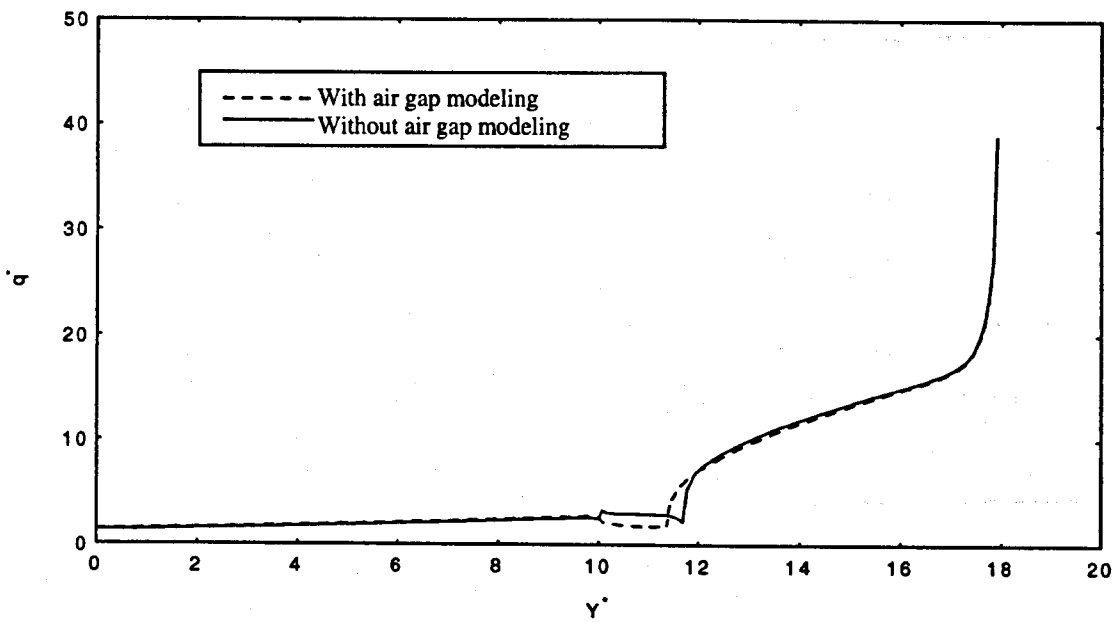

(d) $\theta_0 = 2.5$

Figure 35 contd. Pe = 2.0, $Bi_2 = 0.1$, $Bi_3 = 0.15$

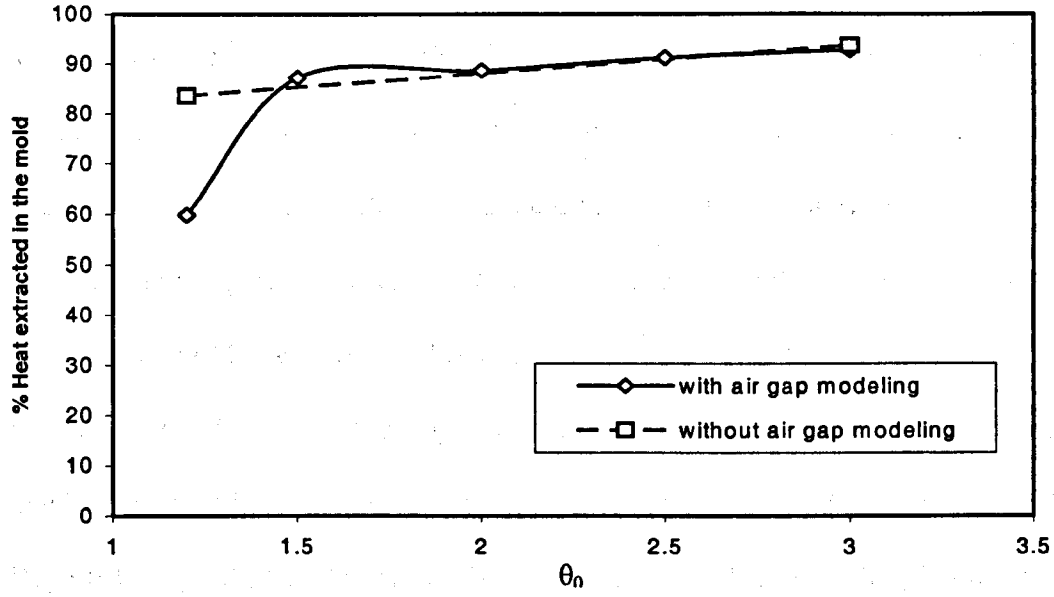

(a) Pe = 1.5

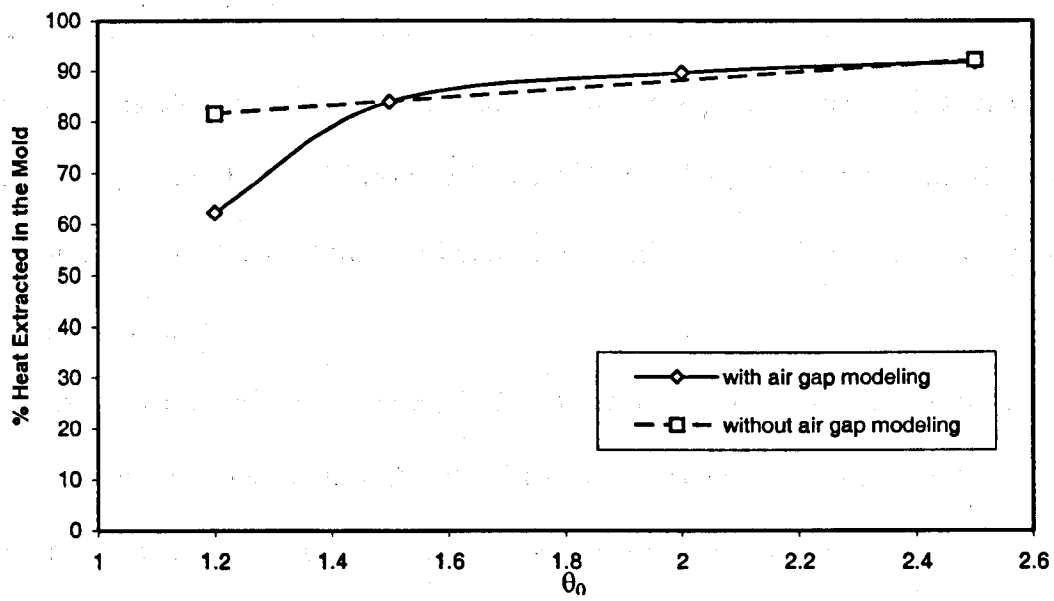

(b) Pe = 2.0

Figure 36. Effect of Superheat on the percent of total heat extracted in the mold for for cases with and without air gap modeling.($Bi_2 = 0.1$, $Bi_3 = 0.15$)

the wall, i.e. from $Y^* = 0$ to $Y^* = 18$. While comparing the local heat flux profiles with and without air gap modeling, as displayed in Figure 35, it was seen that at lower superheat the air gap formed affected the local heat flux in the mold region significantly. As can be seen in Figure 36 the effect of air gap formation on the percent of the total heat extracted in the mold was considerable at low superheat value ($\theta_0 = 1.2$). The dotted line represents the results without air gap modeling. The value of the percent of heat extracted in the mold for air gap modeling was lower by about 30 % for $\theta_0 = 1.2$,Pe = 1.5, $Bi_2 = 0.1$, $Bi_3 = 0.15$ and about 25 % for $\theta_0 = 1.2$,Pe = 1.5, $Bi_2 = 0.1$, $Bi_3 = 0.15$ when compared with those cases without air gap modeling. This difference is attributed to the increased heat resistance of the air gap in the mold region. The fractional heat extracted in the mold is almost the same with and without air gap modeling for higher values of superheat [$\theta_0 = 3.0$, Figure 36 (a) and $\theta_0 = 2.5$, Figure 36 (b)] indicating the diminishing effect of air gap on the heat transfer because of smaller air gap formation with increasing superheat values.

As observed earlier, Figure 33 shows the variation of non-dimensional air gap width with respect to superheat. A curve fit was obtained to yield a polynomial variation of the calculated non-dimensional air gap width with the superheat for various Pe. For both the cases the cooling rates were set to $Bi_2 = 0.1$ and $Bi_3 = 0.15$. The corresponding graphs can be seen in Figure 37.

The diamond shaped symbol represents cases with Pe = 1.5 and the corresponding equation is given by:

$$G^* = 0.0004 \cdot \theta_0^4 - 0.0038 \cdot \theta_0^3 + 0.0128 \cdot \theta_0^2 - 0.0193 \cdot \theta_0 + 0.013 \qquad (5.15)$$

The rectangle shaped symbol represents cases with Pe = 2.0 and the corresponding equation is given by:

$$G^* = 0.0006 \cdot \theta_0^3 - 0.0034 \cdot \theta_0^2 + 0.0058 \cdot \theta_0 - 0.0015 \qquad (5.16)$$

The r^2 value for the above equations for the respective range of superheat temperature was found to be equal to unity, which exhibited that the data was in good agreement with the fitted curve. The previously described phenomena, that is, decrease in the air gap with increase in Pe and θ_0 is clearly visible here.

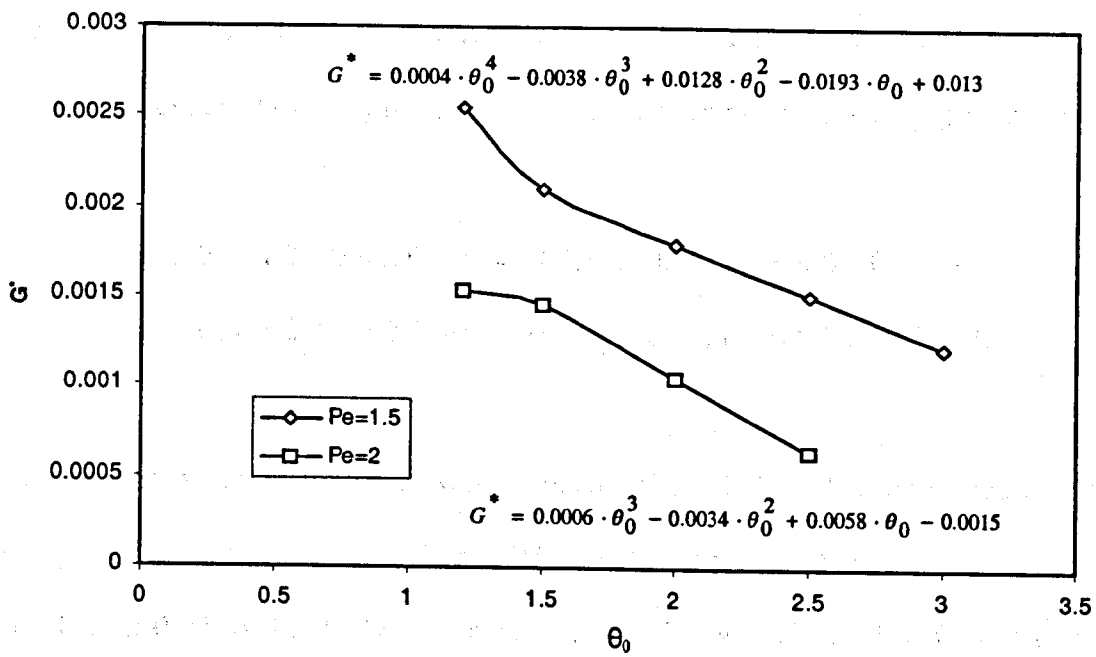

Figure 37. Polynomial curve fit for the variation of non-dimensional air gap width with superheat at different withdrawal speeds. ($Bi_2 = 0.1$, $Bi_3 = 0.15$).

Effect of mold cooling rate

The mold cooling rate is characterized by the non-dimensional number, Bi_2. The mold cooling rate is significant, as a major fraction of the total heat is extracted in the mold and is reported in the previous section. The cooling rate, for a given withdrawal speed, should be sufficiently high to prevent breakout. On the other hand if the cooling rate is very high, it may cause the metal to freeze throughout the domain. High cooling rates increase the production costs as well. So the process demands cooling rates, which are optimum in terms of economy as well as other process requirements. In this study, the copper mold was modeled with convective heat transfer on its surfaces. The following parameters were used to study the effects of mold cooling rate with air gap modeling:

(a): $\theta_0 = 1.2$, $Pe = 2.0$, $Bi_3 = 0.05, 0.1, 0.15$, $Bi_2 = 0.02, 0.05, 0.1$.

(b): $\theta_0 = 1.2$, $Pe = 2.5$, $Bi_3 = 0.05, 0.1, 0.15$, $Bi_2 = 0.02, 0.05, 0.1$.

Two different withdrawal speeds were employed (Pe = 2.0, 2.5), whereas the post mold cooling rate was allowed to vary from 0.05 to 0.15 and the mold cooling rate under study ranged from 0.02 to 0.1. Only, one parameter i.e. Bi_2 was allowed to vary at one time keeping the others constant. Figures 38 and 39 shows the solidification front locations for the aforementioned Cases (a) and (b) respectively.

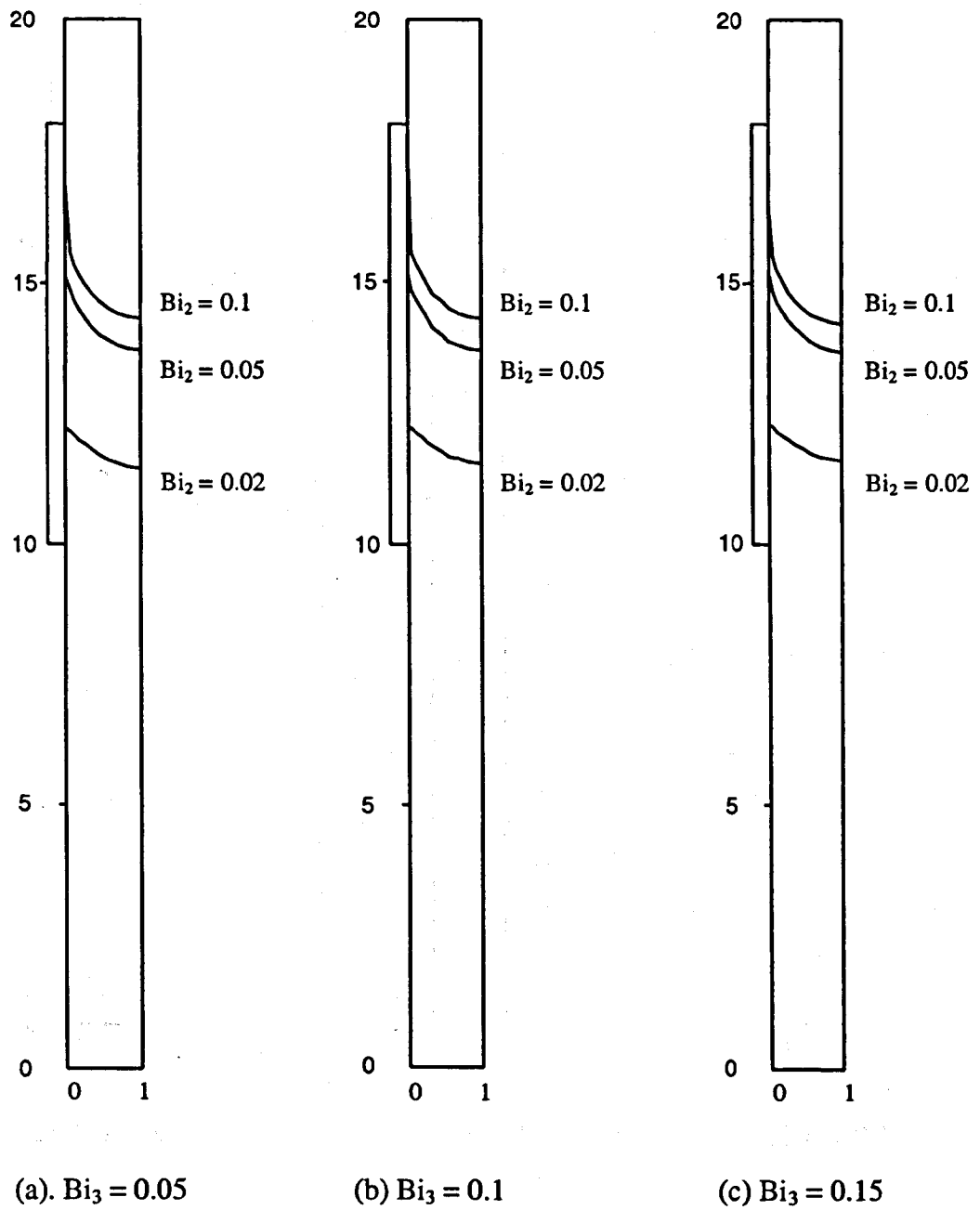

Figure 38. Effect of mold cooling rate on the solidification front locations at different post mold cooling rates for $\theta_0 = 1.2$, $Pe = 2.0$.

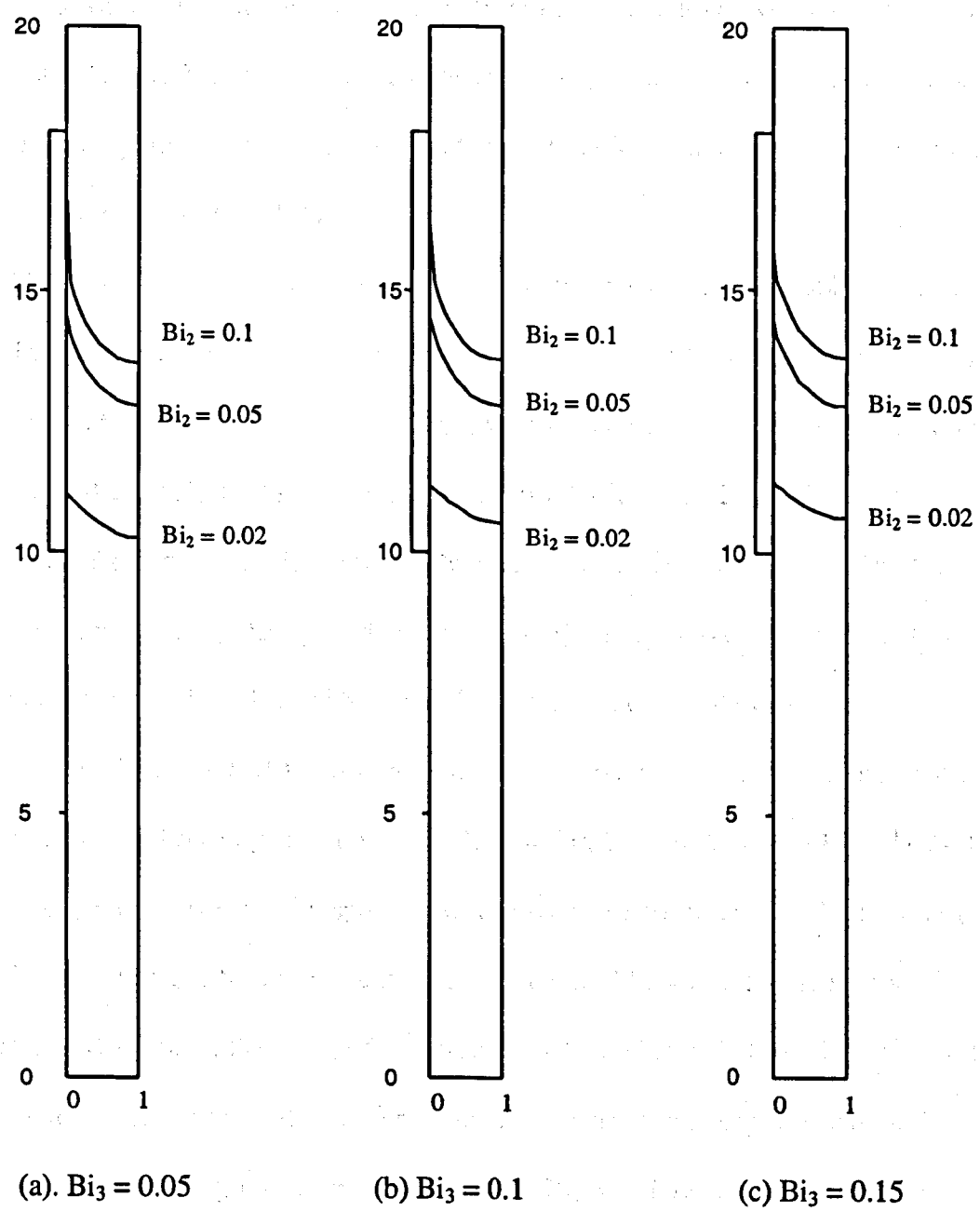

Figure 39. Effect of mold cooling rate on the solidification front locations at different post mold cooling rates for $\theta_0 = 1.2$, $Pe = 2.5$.

It was observed that the solidification front moves upstream with increase in mold cooling rate. This is because, with increase in the Bi_2 value, greater amount of heat is extracted leading to more solidified metal in the mold, which is manifested in the upstream movement of the solidification front.

The shape and slope of the solidification front were considerably affected by change in the mold cooling rate. The front is less steep and more uniform for lower cooling rate. This observation was consistent with different values of post mold cooling rates (Bi_3 = 0.05, 0.1, 0.15) and withdrawal speed (Pe = 2, 2.5). The shape of the solidification front plays an important role in the metallurgical properties of the cast material as reported by Kang and Jaluria (1993). They have reported that a flat solidification front is desirable for better uniformity in the cast material.

Figures 40 (a) and (b) show the variation of overall non-dimensional heat flux with respect to mold cooling rate, for $\theta_0 = 1.2$, Pe = 2.0, Bi_3 = 0.05, 0.1, 0.15 and $\theta_0 = 1.2$, Pe = 2.5, Bi_3 = 0.05, 0.1, 0.15 respectively. The overall non-dimensional heat flux (Q^*) ranged from 1.01 to 2.2 for the present cases. As the mold cooling rate is increased from $Bi_2 = 0.02$ to $Bi_2 = 0.05$, the value of Q^* increases which shows that mold cooling rate is the dominant factor for heat transfer despite interfacial air gap formation. Further increase in mold cooling rate from $Bi_2 = 0.05$ to $Bi_2 = 0.1$ results in a decrease in the value of Q^*. The maximum value of Q^* occurs at $Bi_2 = 0.05$ for the given process parameters as seen in Figures 40 (a) and (b). This is because, increase in mold cooling rate from $Bi_2 = 0.05$ to $Bi_2 = 0.1$ leads to upstream movement of the solidification front.

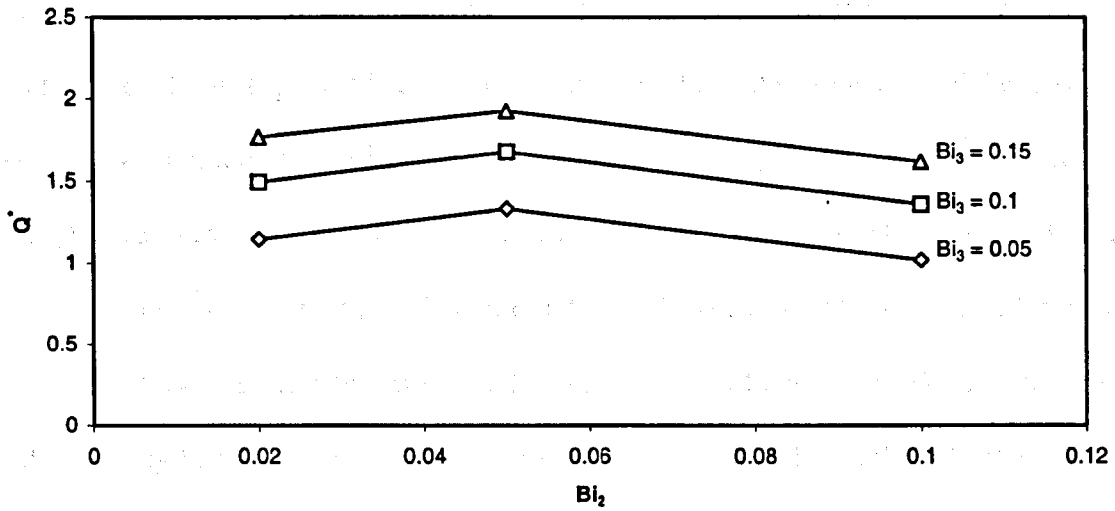

(a)

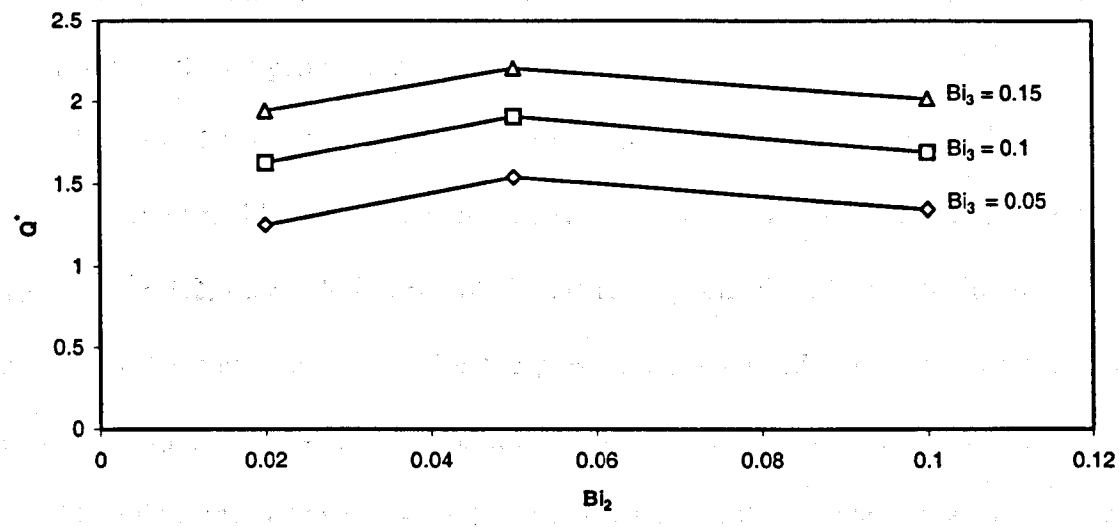

(b)

Figure 40. Overall heat flux variation with respect to mold cooling rate for $\theta_0 = 1.2$, $Bi_3 = 0.05, 0.1, 0.15$ for different withdrawal speeds.

(a) Pe = 2.0, (b) Pe = 2.5

This means more metal is solidified in the mold leading to more shrinkage and as such a higher value of air gap width and length. It is to be noted that overall heat flux is governed by both, the effective heat transfer coefficient ($H_{eff} << h_2$) and the mold cooling rate (h_2). Due to the upstream movement of the solidification front, H_{eff} is applied over a significant length on the surface of the mold due to the presence of the air gap. Hence the overall heat flux is dominated more by H_{eff} than h_2 (mold cooling rate). Higher air gap width critically hampers the heat transfer phenomenon due to low value of effective heat transfer coefficient which explains the decrease in the overall heat flux. Thus the value of the area of the solidified metal in the mold is crucial as it is directly related to the air gap width through shrinkage. The heat extraction efficiency of the mold is also affected in a similar way by the air gap formation.

Figures 41 (a) and 41 (b) shows the fraction of the total heat extracted in the mold against different mold cooling rates for the cases with $\theta_0 = 1.2$, Pe = 2.0, $Bi_3 = 0.05, 0.1, 0.15$ and $\theta_0 = 1.2$, Pe = 2.5, $Bi_3 = 0.05, 0.1, 0.15$ respectively. Most of the total heat was extracted in the mold region and for the present cases ranged from 60 to 85 %. It was again observed that the percent heat extracted in the mold initially increases with increase in mold cooling rate from $Bi_2 = 0.02$ to $Bi_2 = 0.05$ and then decreases with increase in mold cooling rate to $Bi_2 = 0.1$. As explained in the earlier section, the increase in the air gap width at the metal-mold interface is the cause of the drop in the fractional heat extracted in the mold. Thus, it can be stated that for a given set of process parameters, there exists a critical value of mold cooling rate which results in maximum value of overall heat flux and the fractional heat extracted in the mold. For the present cases with

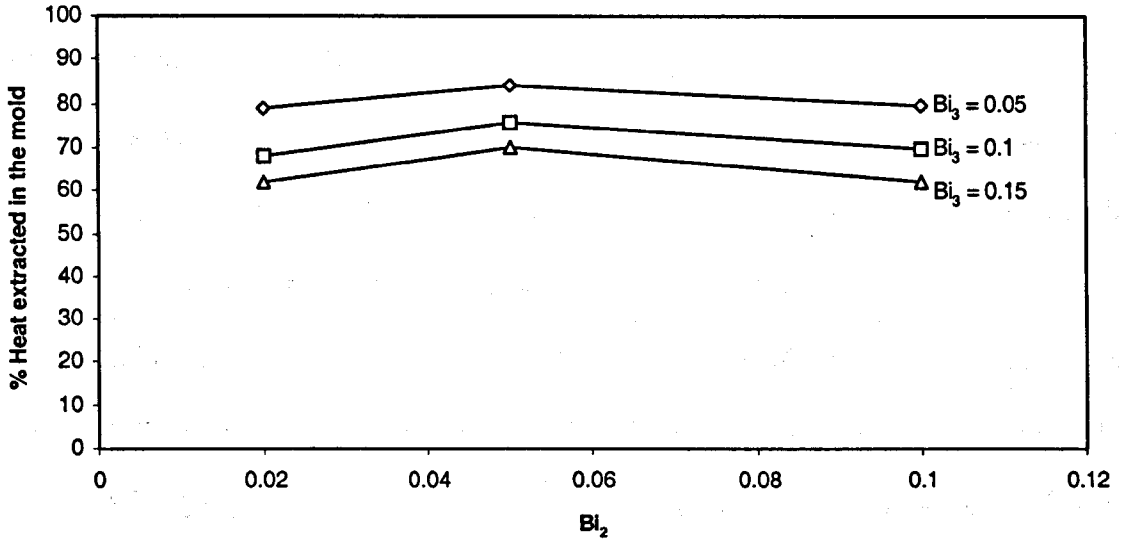

(a) Pe = 2.0

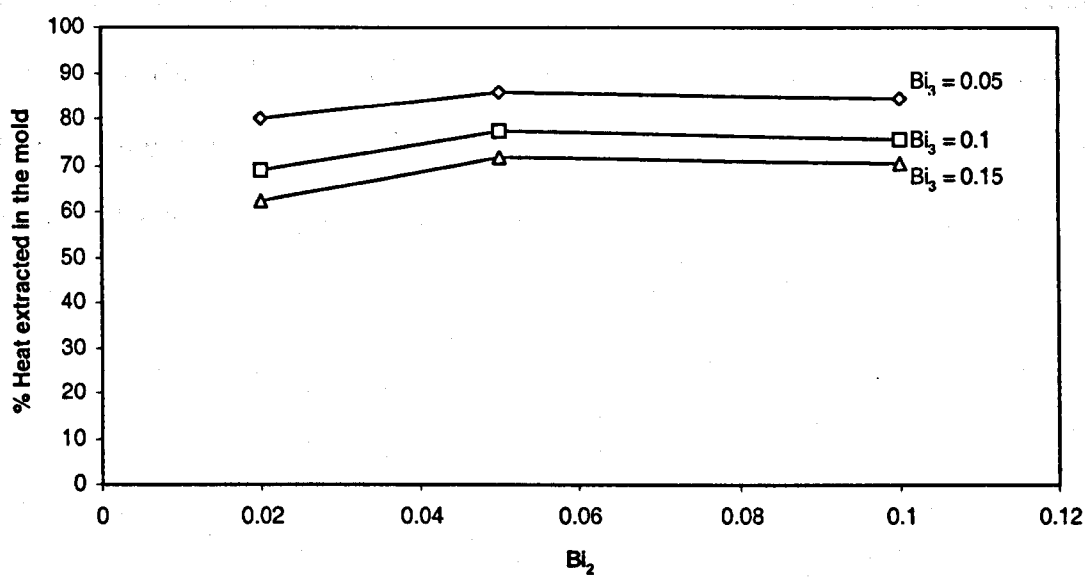

(b) Pe = 2.5

Figure 41. Percent of heat extracted in the mold versus mold cooling rates for $\theta_0 = 1.2$, $Bi_3 = 0.05, 0.1, 0.15$ at different withdrawal speeds.

$\theta_0 = 1.2$, Pe = 2.0,2.5, $Bi_3 = 0.05, 0.1, 0.15$, the overall heat flux and the fractional heat extracted in the mold was maximum at $Bi_2 = 0.05$.

Figures 42 and 43 shows the effect of mold cooling rate on the wall and the centerline temperature profile. Higher mold cooling rates leads to more cooling which leads to lower wall and centerline temperature throughout the domain.

Typical local heat flux variation for different values of mold cooling rates for $\theta_0 = 1.2$, Pe = 2.0, $Bi_3 = 0.1$ is shown in Figure 44. The local heat flux is zero in the pre-mold ($Y^* = 18$ to $Y^* = 20$) as it is insulated. In the upstream direction, from $Y^* = 18$ to $Y^* = 10$ (mold region), the local heat flux decreases from its maximum value at $Y^* = 18$. This drop in the local heat flux in the mold region exhibits the formation of the air gap. At the mold exit, $Y^* = 10$, the local heat flux shows a sudden rise as the air gap ceases to exist and then in the post-mold region ($Y^* = 10$ to $Y^* = 0$) the heat flux values continuously decreases till the exit of the post mold ($Y^* = 0$).

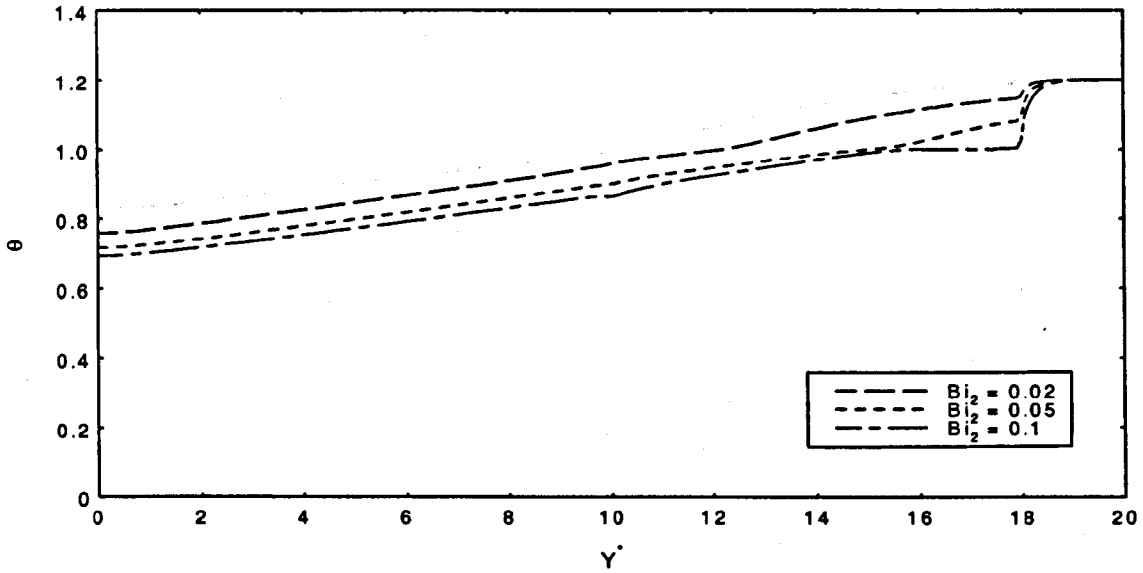

(a)

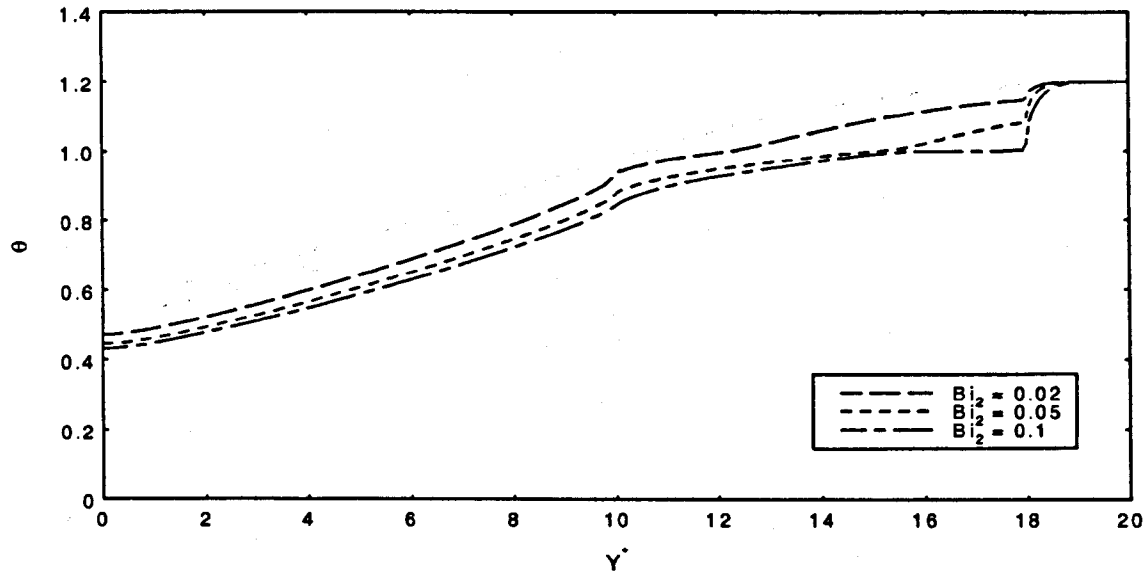

(b)

Figure 42. Effect of Bi_2 on wall temperature profiles for $\theta_0 = 1.2$, $Pe = 2.0$.

(a) $Bi_3 = 0.05$, (b) $Bi_3 = 0.15$

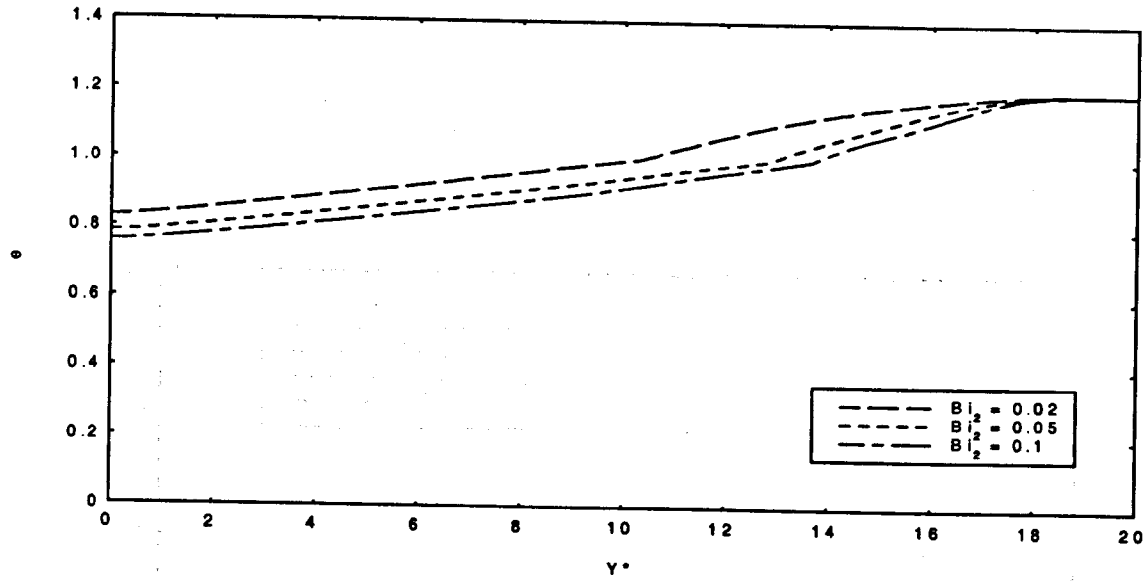

(a)

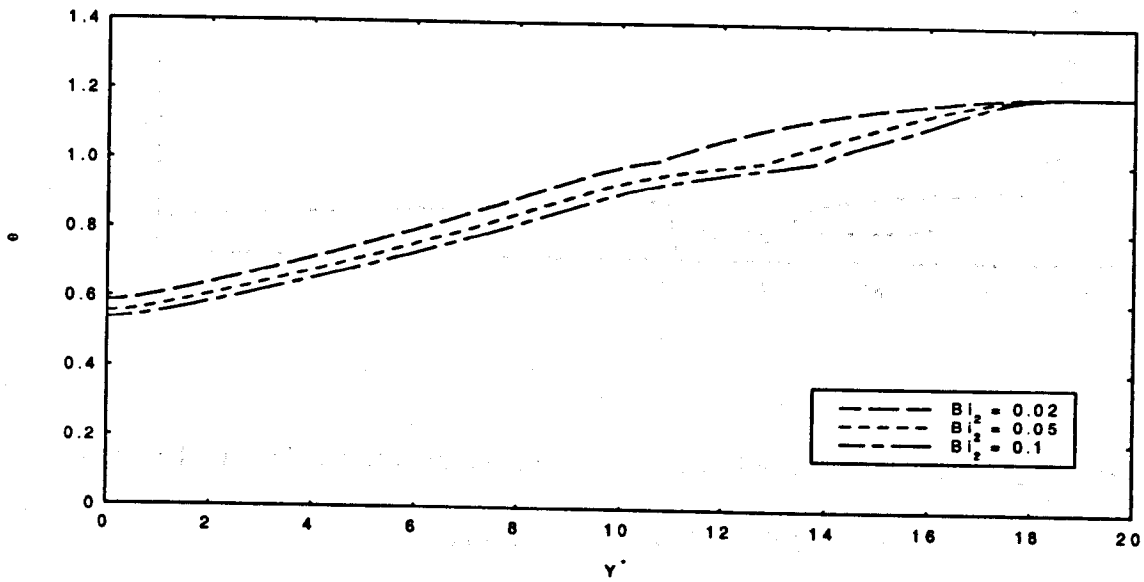

(b)

Figure 43. Effect of Bi_2 on centerline temperature profiles for $\theta_0 = 1.2$, $Pe = 2.5$.

(a) $Bi_3 = 0.05$, (b) $Bi_3 = 0.15$

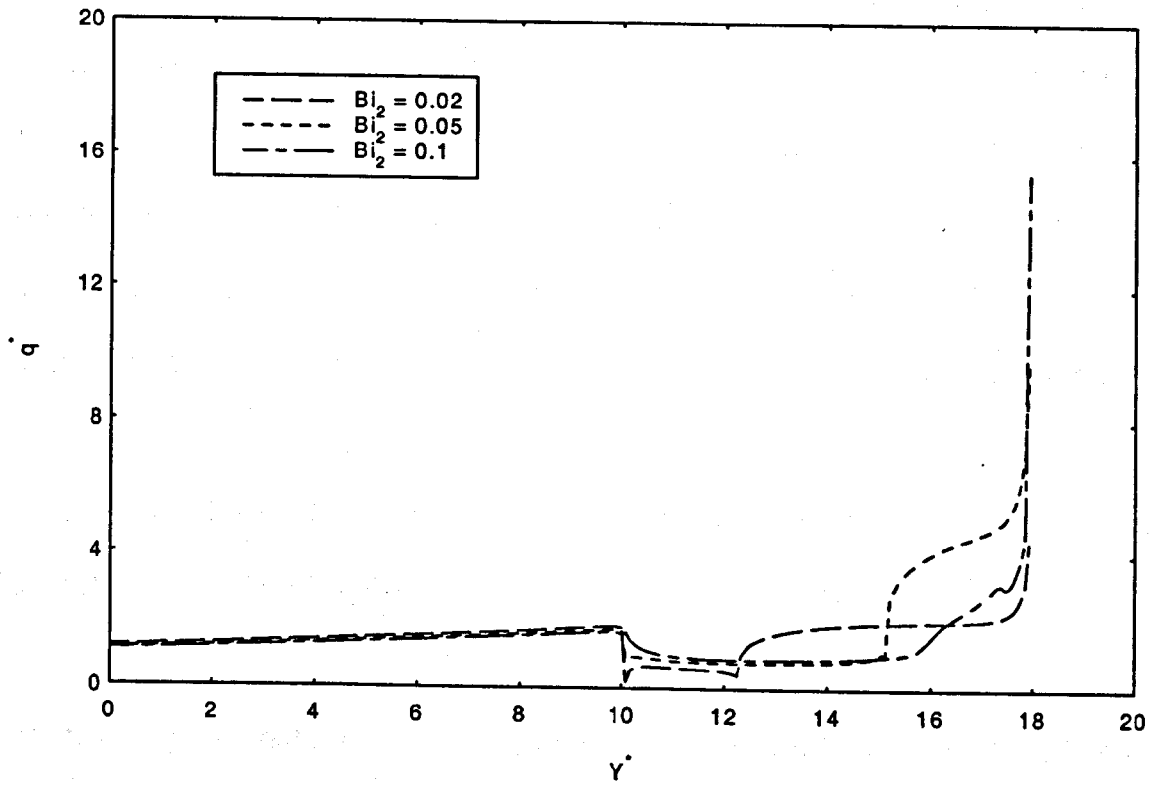

Figure 44. Local heat flux variation along the mold wall for different Bi_2 values for

$\theta_0 = 1.2$, $Pe = 2.0$, $Bi_3 = 0.1$.

Effect of post mold cooling rate

The solidified metal shell is subjected to water spray cooling after it exits from the mold. Present model takes into account the convective heat transfer at the surface of the shell as it is withdrawn. High cooling rates in the post mold zone may introduce residual stresses in the shell, which can result in surface cracks. On the other hand lower cooling rates may produce more volume of liquid pool, which may lead to breakouts. Brimacombe et al. (1984) have also reported that the sprays influence precipitation of secondary phases reducing ductility of the cast material.

The post mold cooling rate study with air gap modeling involved the following cases:

Case (a): $\theta_0 = 1.2$, Pe = 2.0, $Bi_2 = 0.02, 0{,}05, 0.1$, $Bi_3 = 0.05, 0.1, 0.15$

Case (b): $\theta_0 = 1.2$, Pe = 2.5, $Bi_2 = 0.02, 0{,}05, 0.1$, $Bi_3 = 0.05, 0.1, 0.15$

The effect of post-mold cooling rate was studied at different withdrawal speeds (Pe = 2.0, 2.5) and mold cooling rates ($Bi_2 = 0.02, 0{,}05, 0.1$). Influence of Bi_3 on the solidification front location is shown in Figure 45. Isotherm, $\theta = 1$, corresponds to the phase front.

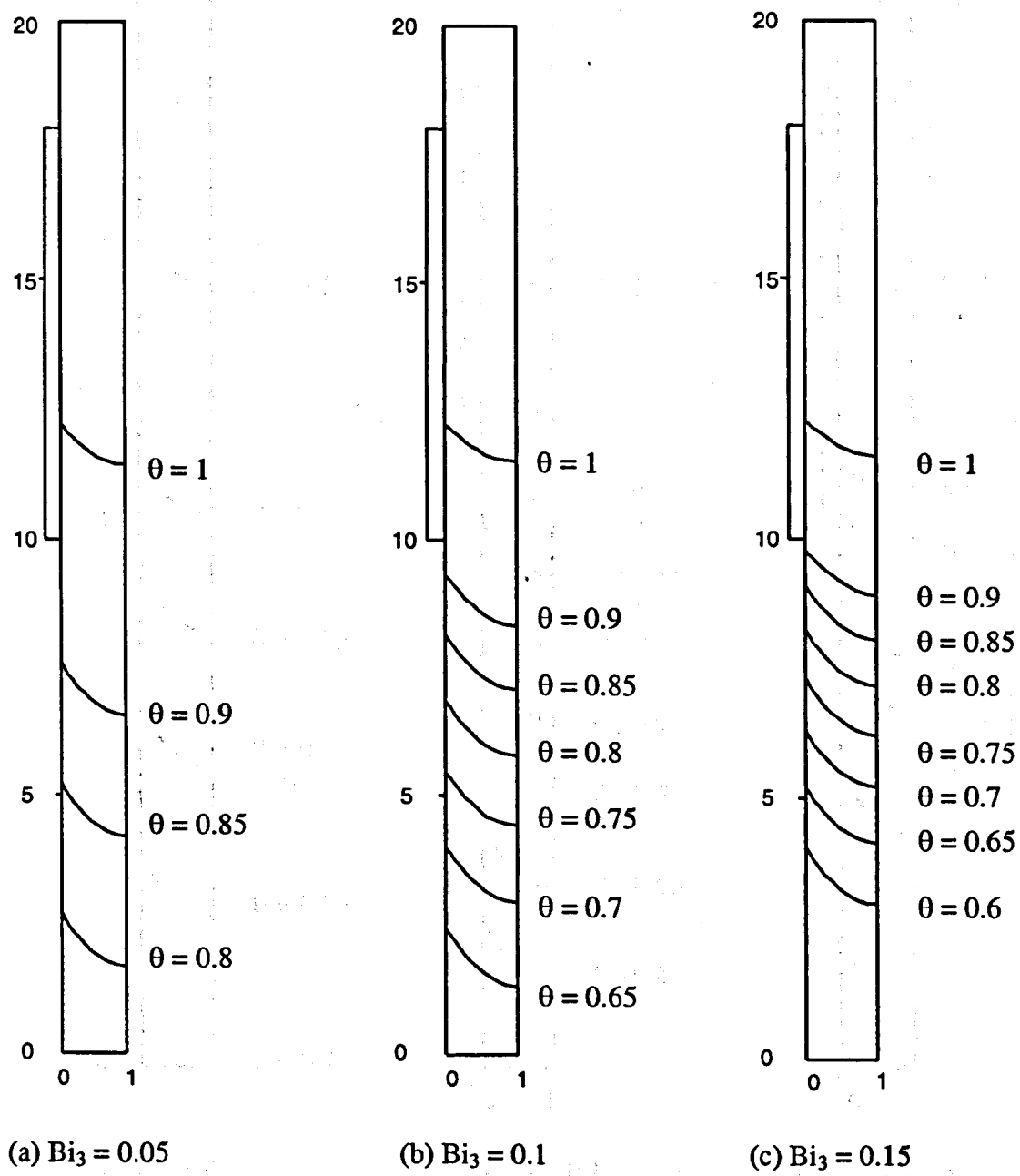

Figure 45. Effect of post mold cooling rates on the isotherms.

($\theta_0 = 1.2$, $Pe = 2.0$, $Bi_2 = 0.02$)

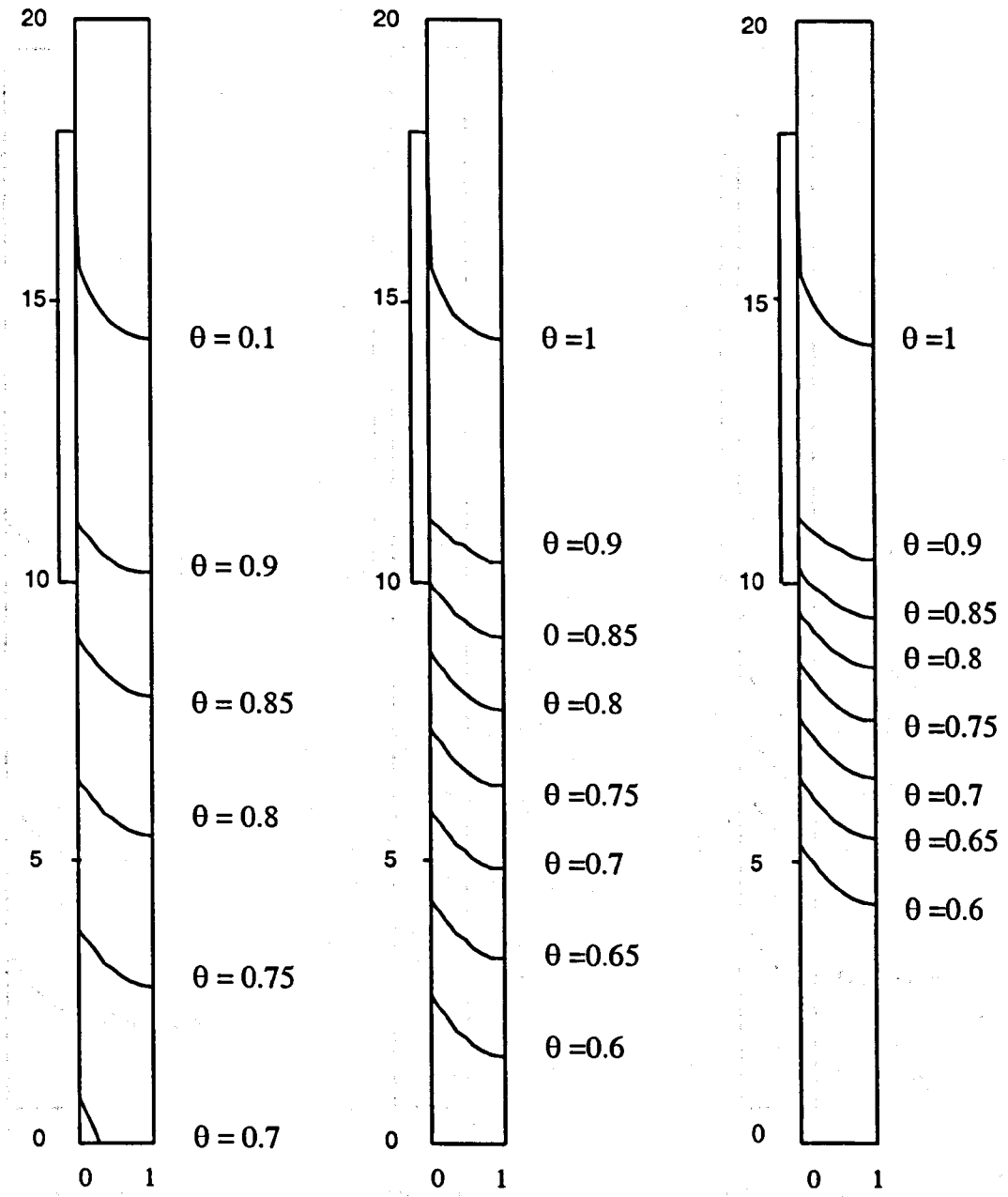

(d) $Bi_3 = 0.05$ (e) $Bi_3 = 0.1$ (f) $Bi_3 = 0.15$

Figure 45 contd.($\theta_0 = 1.2$, $Pe = 2.0$, $Bi_2 = 0.1$)

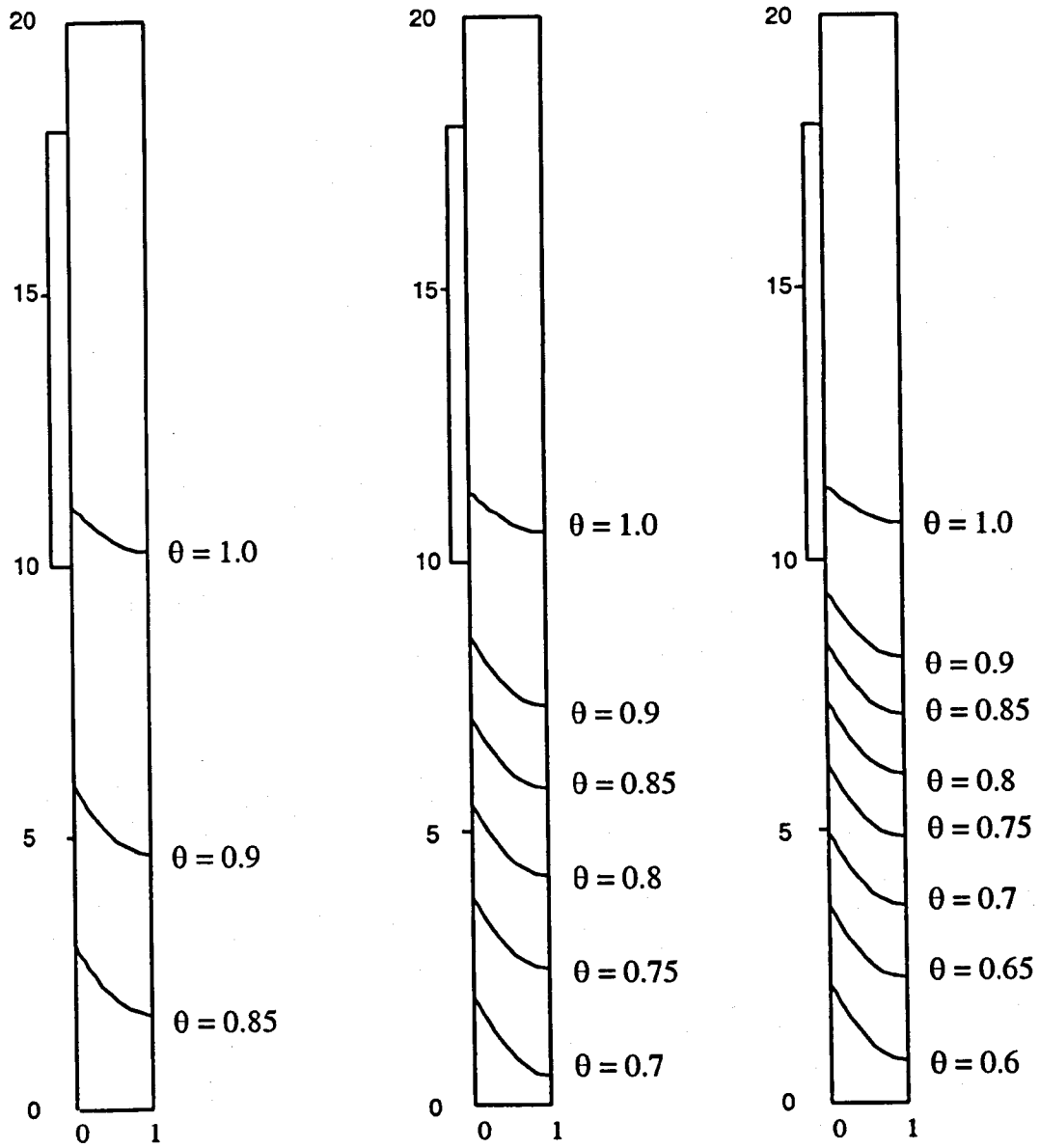

(g) $Bi_3 = 0.05$ (h) $Bi_3 = 0.1$ (i) $Bi_3 = 0.15$

Figure 45 contd. ($\theta_0 = 1.2$, $Pe = 2.5$, $Bi_2 = 0.02$)

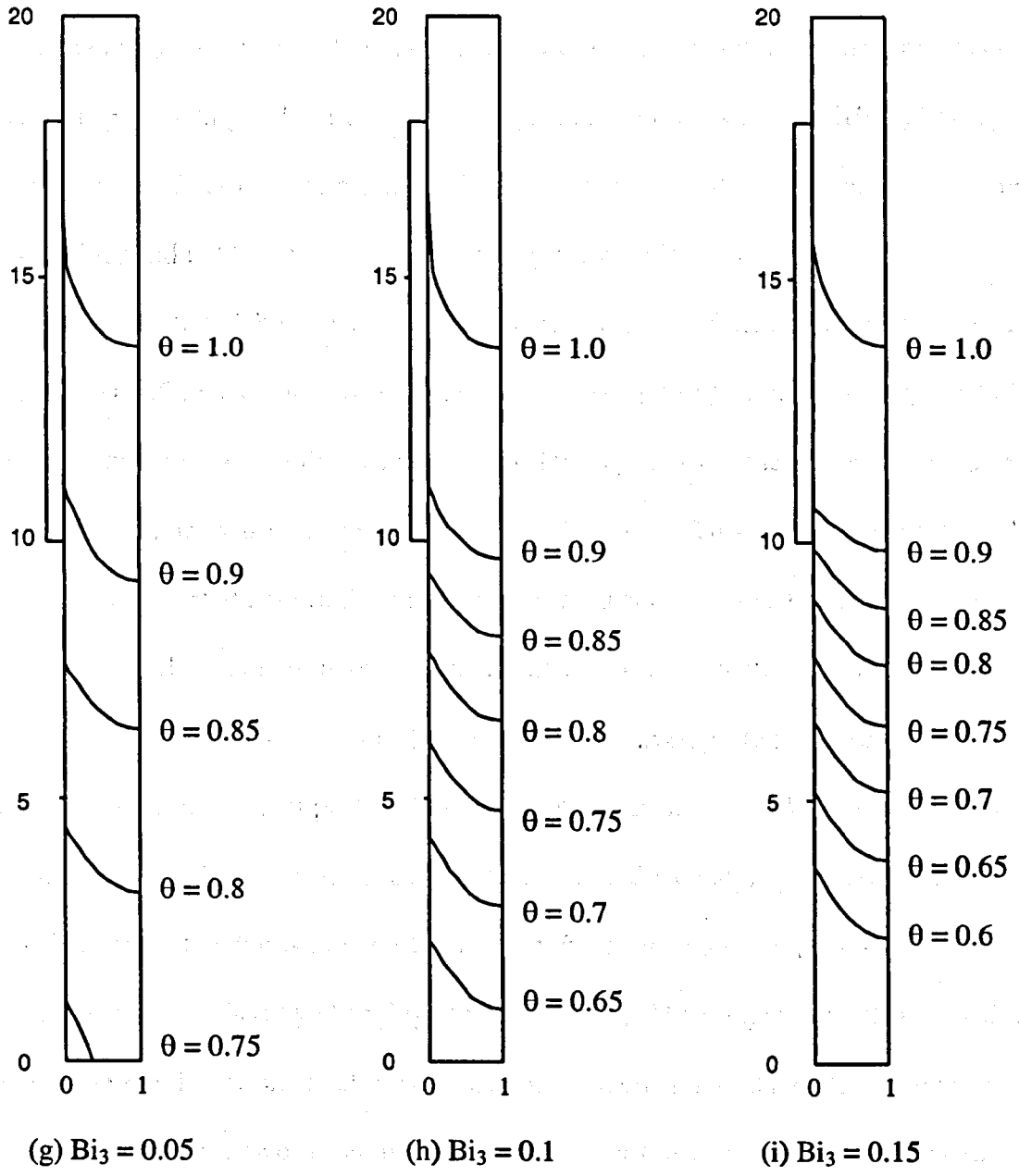

Figure 45 contd. ($\theta_0 = 1.2$, $Pe = 2.5$, $Bi_2 = 0.1$)

The solidification front location does not change significantly with change in post mold cooling rate. This is because most of the total heat is extracted in the mold and hence the mold cooling rate dominates the heat transfer rather than the post mold cooling. The air gap modeling did not change this aspect of the process. Greif (1998) has reported the negligible effect of post mold cooling rate on the solidification front position in his work, which did not take into account the air gap formation.

As illustrated by the isotherms, the temperature distribution in the post mold region is significantly affected by change in cooling rate as more heat is removed from the withdrawn metal with the increase in Bi_3. The isotherms in the post mold region move upstream with increase in the post mold cooling rate. This was the case for all the parameters presented here in the study of post mold cooling rate. The temperature profile provides useful information on the metallurgical transformation of the metal and is critical in case of alloys. It can also be stated that average temperature of the system decreases with increase in post mold cooling. As seen in Figure 45, the position and the shape of the solidification front cannot be controlled by varying the post mold cooling rate. However, the temperature of the solid metal leaving the post mold region can definitely be controlled by changing the value of Bi_3. The temperature of the solid metal exiting the mold is of practical importance for subsequent metal handling operations. The overall heat flux for two different casting speeds was also investigated and is shown in Figure 46. The overall non-dimensional heat flux increases with increases with increase

in the post mold cooling rate. Q^* ranged from 1 to 2.2 for $\theta_0 = 1.2$, Pe = 2.0,2.5, Bi_2 = 0.02, 0,05, 0.1 for the post mold cooling rates of Bi_3 = 0.05, 0.1, 0.15.

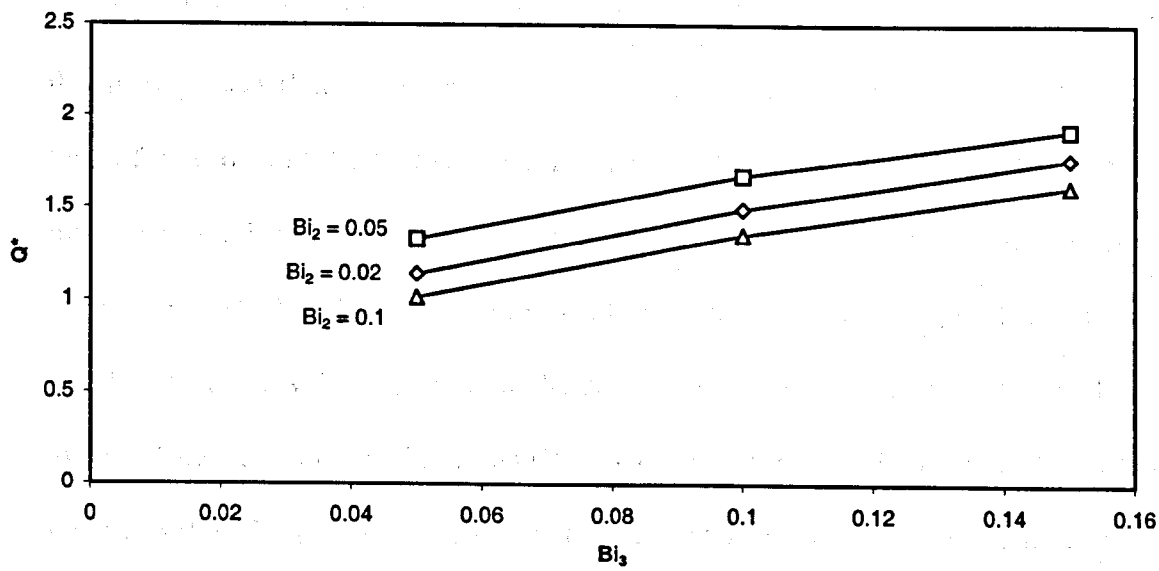

(a) Pe = 2.0

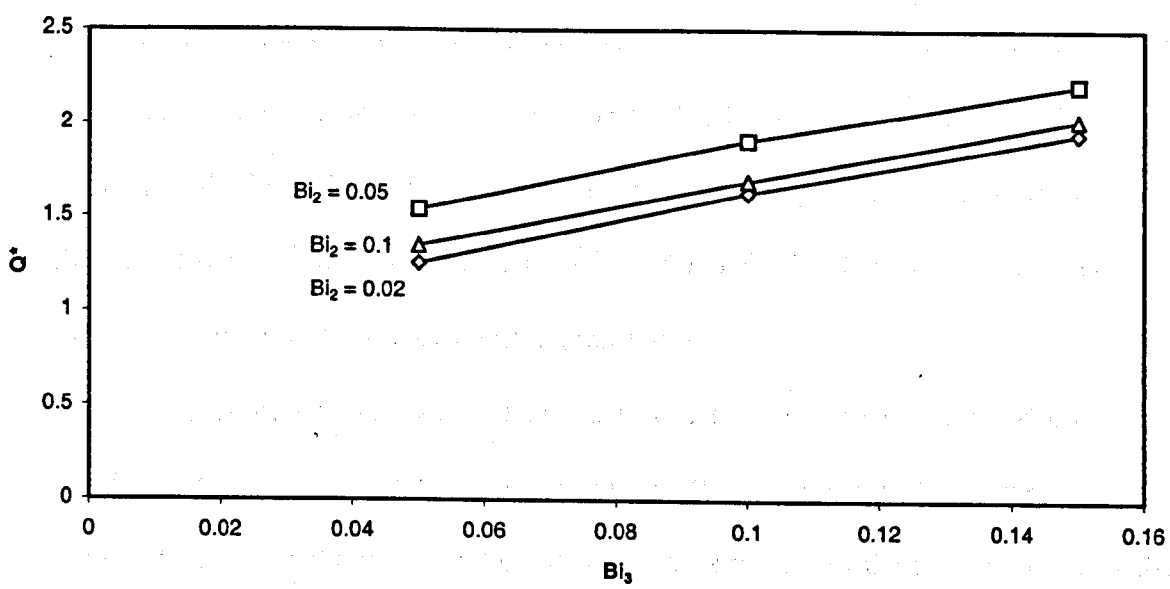

(b) Pe = 2.5

Figure 46. Effect of Bi_3 on overall heat flux for $\theta_0 = 1.2$, Bi_2 = 0.02, 0,05, 0.1.

Figure 47 shows the percent of total heat extracted in the mold with different post mold cooling rates. The fractional heat extracted in the mold decreases with increase in the Bi_3 value. The percent heat extracted in the mold was earlier defined as the ratio of the average heat flux in the mold region, i.e. the heat extracted by the copper mold, to that of the overall heat flux. The average heat flux was obtained by numerically integrating the local heat flux values in the mold region ($Y^* = 10$ to 18). It was found that there was negligible difference in the wall temperatures in the mold region ($Y^* = 10$ to 18) for different values of post mold cooling rates. Hence, it can be stated that the average heat flux in the mold region ($Y^* = 10$ to 18) is more or less constant for change in the Bi_3 value. It is to be noted that, the percent heat extracted in the mold region is directly proportional to the average heat flux in the mold region and is inversely proportional to the overall heat flux Q^*. Therefore, as the average heat flux in the mold region is constant irrespective of the value of Bi_3, the percent heat extracted in the mold region is only dependent on and as stated here is inversely proportional to the overall heat flux Q^*. Since Q^* increases with increase in Bi_3 (Refer Figure 46), the percent heat extracted in the mold decreases with increase in Bi_3.

The centerline temperature and the wall temperature profiles for different post mold cooling rates can be seen in Figures 48, 49 and Figures 50, 51 respectively. It is seen that change in the post mold cooling rate does not affect the temperature distribution (both wall and centerline) in the pre-mold and the mold region ($Y^* = 10$ to 20). However, increasing the post mold cooling rate increases the cooling of the metal in the post mold

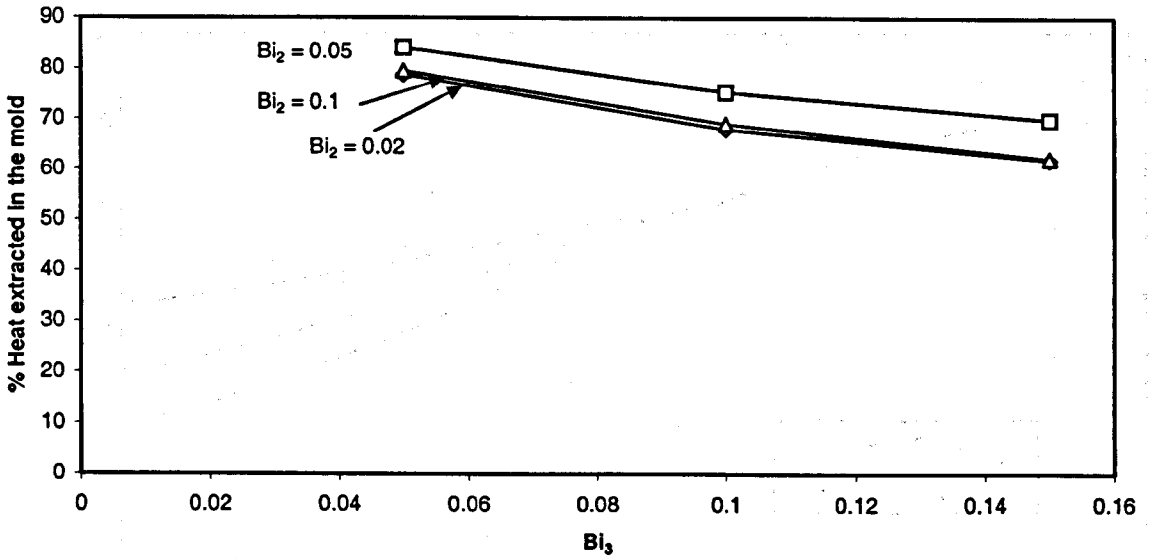

(a)

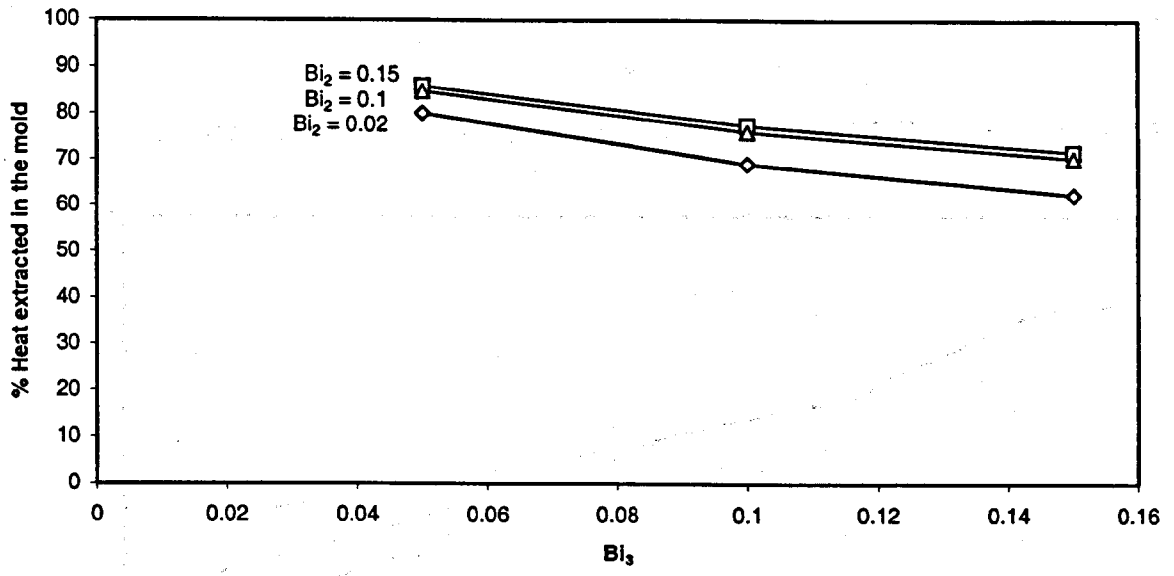

(b)

Figure 47. Variation of fractional heat extracted in the mold with Bi_3.

(a) $\theta_0 = 1.2$, $Pe = 2.0$, $Bi_2 = 0.02, 0{,}05, 0.1$

(b) $\theta_0 = 1.2$, $Pe = 2.5$, $Bi_2 = 0.02, 0{,}05, 0.1$

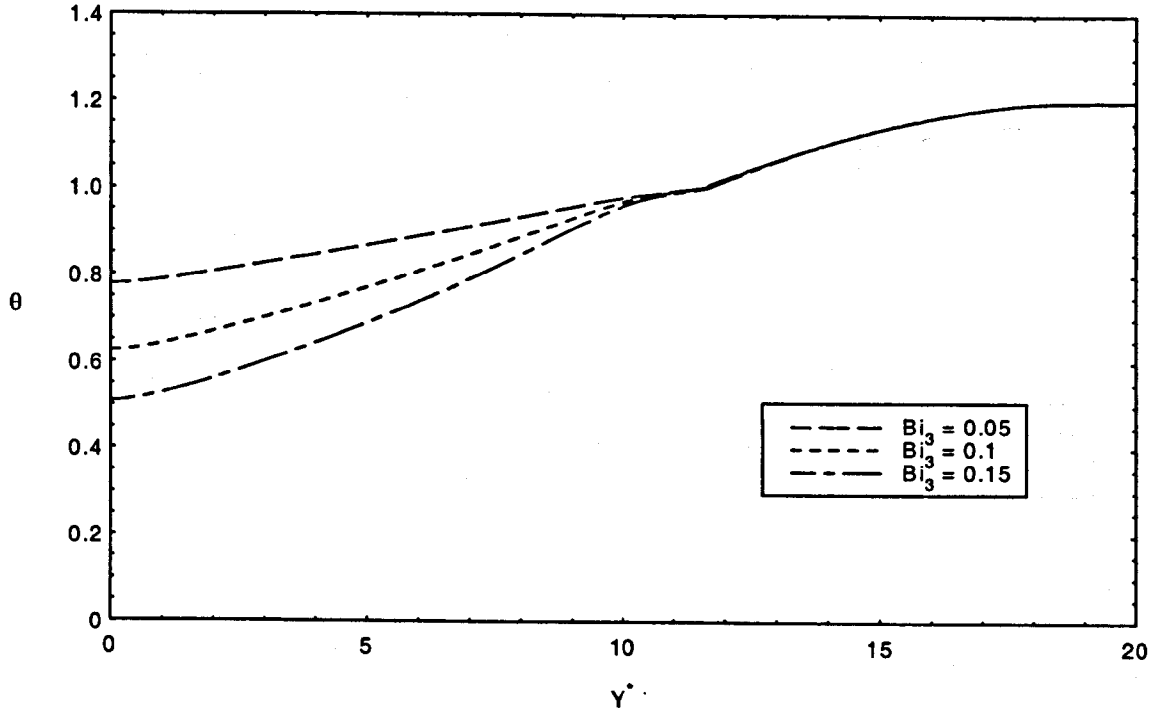

Figure 48. Centerline temperature for $\theta_0 = 1.2$, Pe = 2.0, $Bi_2 = 0.02$, $Bi_3 = 0.05, 0.1, 0.15$.

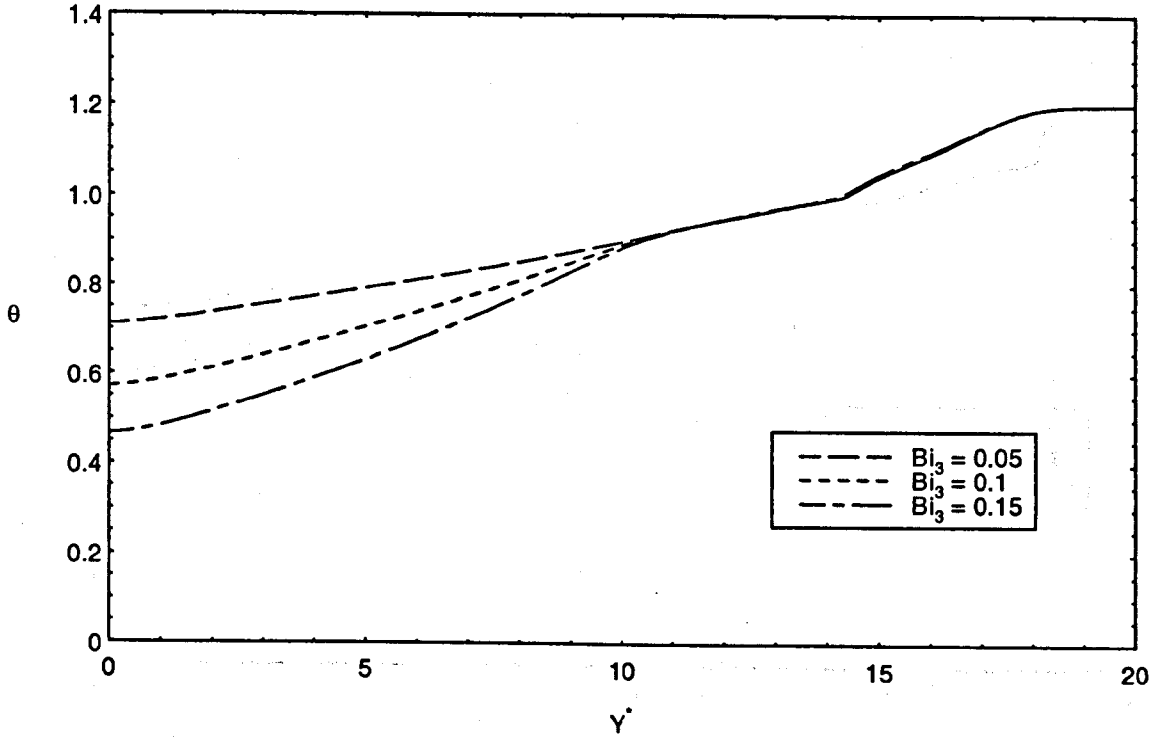

Figure 49. Centerline temperature for $\theta_0 = 1.2$, Pe = 2.0, $Bi_2 = 0.1$, $Bi_3 = 0.05, 0.1, 0.15$.

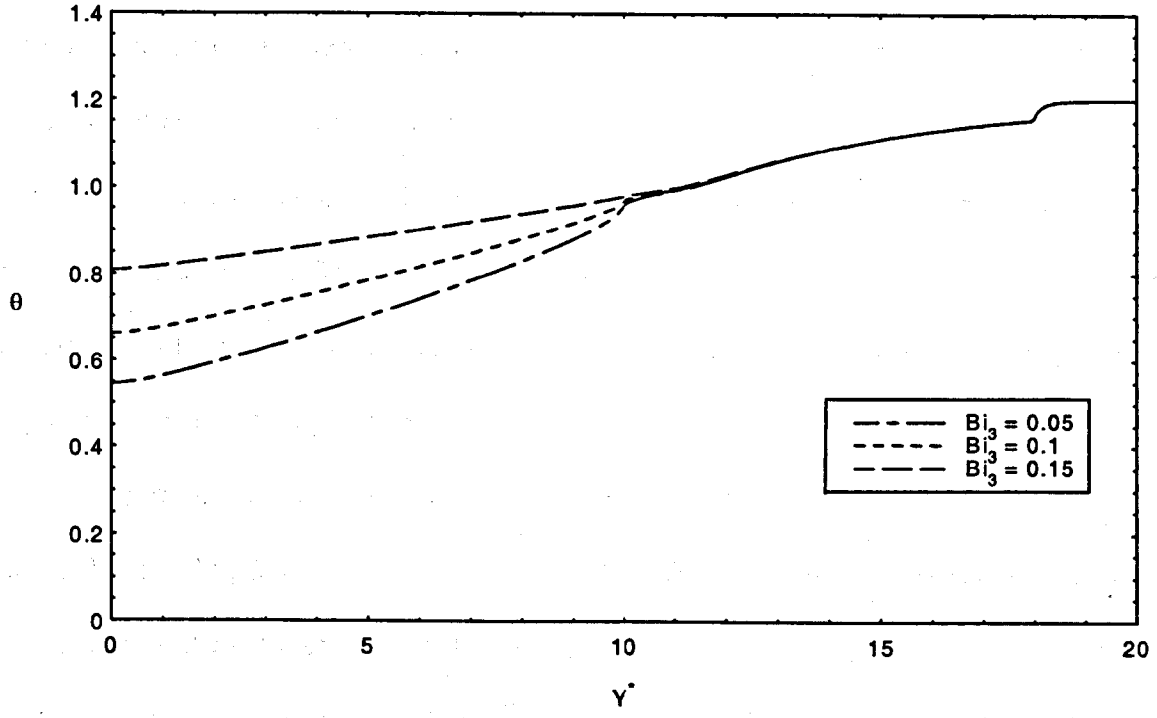

Figure 50. Wall temperature for $\theta_0 = 1.2$, Pe = 2.5, $Bi_2 = 0.02$, $Bi_3 = 0.05, 0.1, 0.15$.

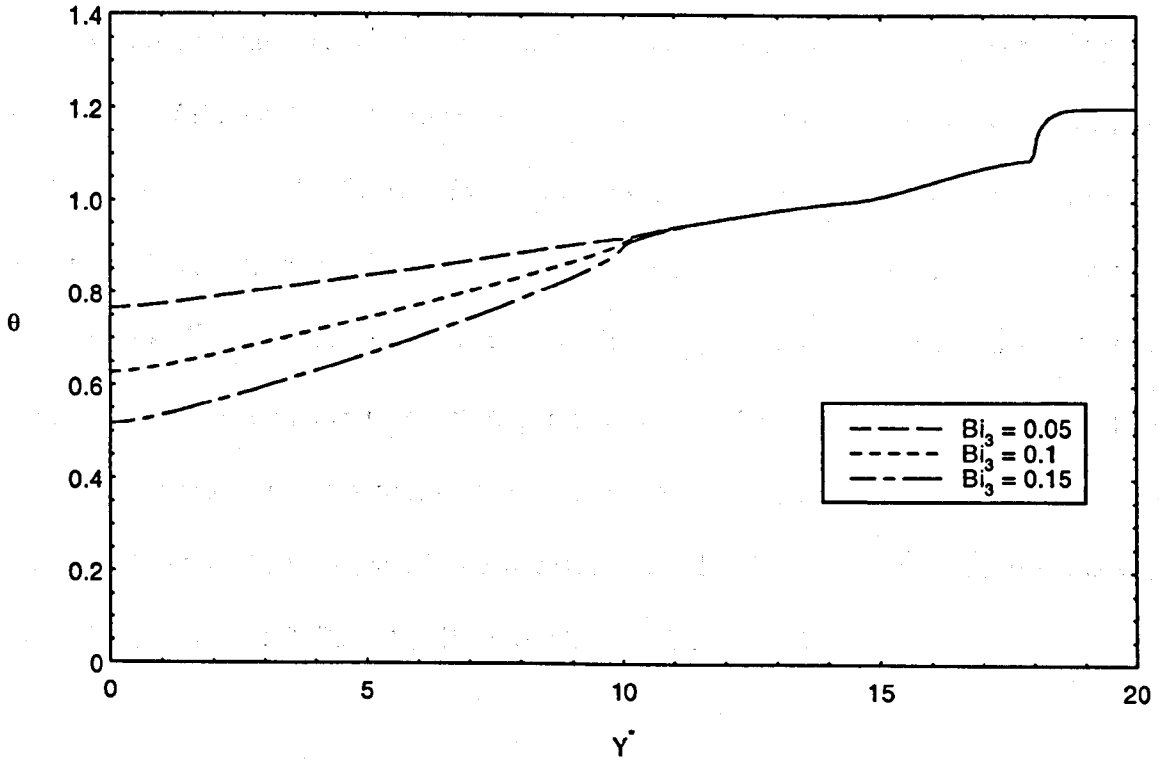

Figure 51. Wall temperature for $\theta_0 = 1.2$, Pe = 2.5, $Bi_2 = 0.1$, $Bi_3 = 0.05, 0.1, 0.15$.

region leading to lower temperatures in the post mold region ($Y^* = 0$ to 10). Again, this effect was due to the fact that most part of the total heat is extracted in the mold which is dictated by the Bi_2 value. Mold cooling rate is a dominant factor as far as mold heat transfer is concerned, Thus, it can be summarized that, the effect of Bi_3 on the solidification front position as well as the temperature distribution in the mold region was negligible in spite of air gap formation.

Figure 52 shows the effect of post mold cooling rate on the percent drop in Bi_2 for $\theta_0 = 1.2$, Pe = 2.0, 2.5, $Bi_2 = 0.02$, 0,05, 0.1. The percent drop in Bi_2 was earlier defined as the ratio of the difference of mold cooling rate (Bi_2) and the non-dimensional effective heat transfer coefficient (H^*) to the mold cooling rate (Bi_2). It can be seen that there is very little change in the value of the parameter, percent drop in Bi_2, with change in the post mold cooling rate. This is because the mold heat transfer is strongly governed by Bi_2 irrespective of the post mold cooling rate. Also, since there is little or no effect of post mold cooling on the solidification front positions, the solidified metal area in the mold is almost equal for different values of Bi_3. Consequently, the change in the values of the air gap width or H^* with change in Bi_3 is small. Hence, Figure 52 demonstrates small or no change in the value of the parameter, percent drop in Bi_2, for different values of post mold cooling rate. The maximum value of the parameter, percent drop in mold cooling rate, was about 70 % for $\theta_0 = 1.2$, Pe = 2.0, $Bi_2 = 0.1$, whereas the minimum value was around 3 % for $\theta_0 = 1.2$, Pe = 2.5, $Bi_2 = 0.02$, $Bi_3 = 0.05$.

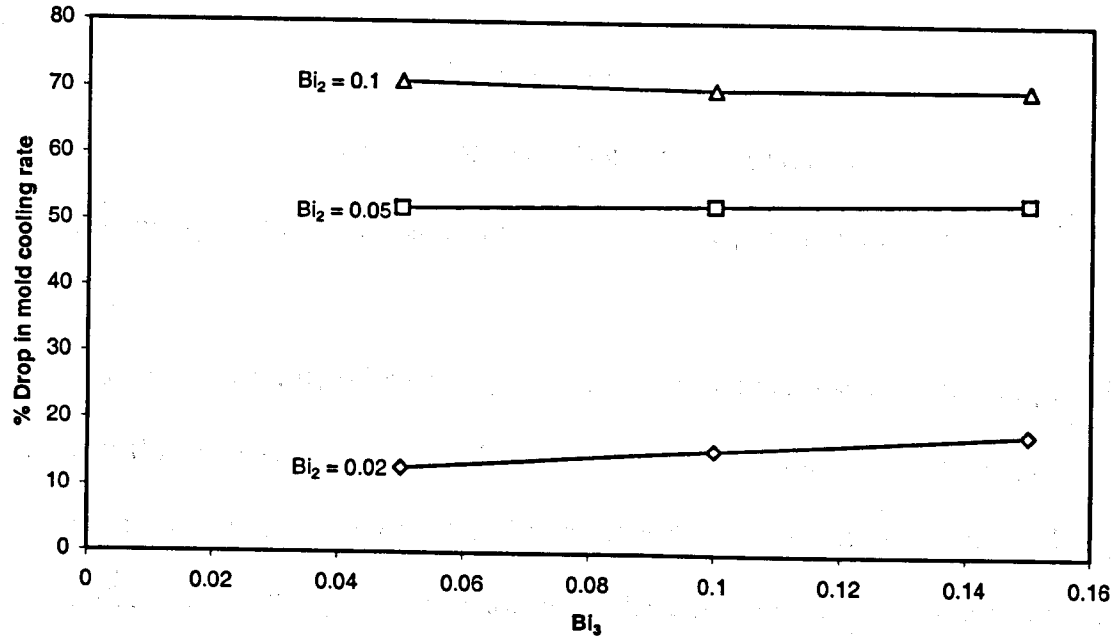

(a)

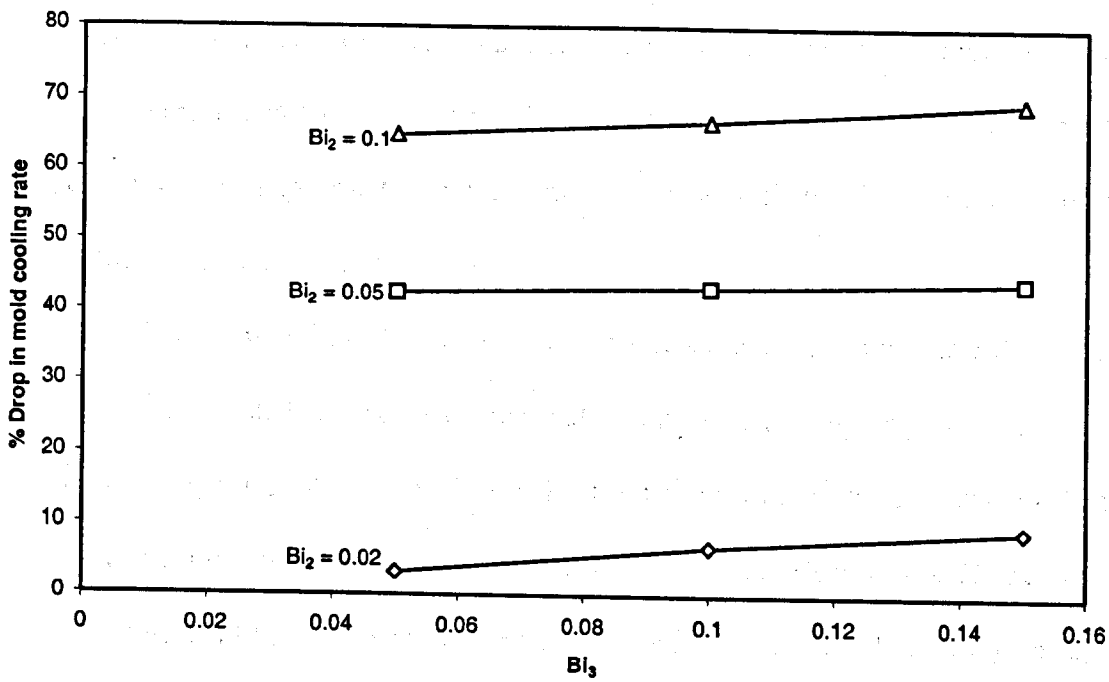

(b)

Figure 52. Percentage drop in mold cooling rate.

(a) $\theta_0 = 1.2$, Pe = 2.0, $Bi_2 = 0.02, 0{,}05, 0.1$, $Bi_3 = 0.05, 0.1, 0.15$

(b) $\theta_0 = 1.2$, Pe = 2.5, $Bi_2 = 0.02, 0{,}05, 0.1$, $Bi_3 = 0.05, 0.1, 0.15$

CHAPTER 6

CONCLUSIONS / RECOMMENDATIONS

Following are the conclusions drawn based on the present numerical investigation:

1. The overall heat transfer was strongly affected by small values of the air gap. The fact that air has very low conductivity validates this finding. The comparison of the results of cases run with and without air gap modeling demonstrated major differences in the phase front locations, heat flux and temperature distribution. Higher temperatures in the mold region as well as a sharp drop in the heat flux was observed due to increased heat resistance at the metal mold interface. However, in some cases, that is with higher superheat and withdrawal speed, the effect of air gap resistance was minor and was dictated by the area of the solidified metal in the mold.
2. The effect of withdrawal speed on the phase front and the temperature distribution was significant. Increase in withdrawal speed leads to steeper phase front in the case of higher cooling rates. The solid front moves downstream but the effect is more prominent at lower cooling rates ($Bi_2 = 0.02$, $Bi_3 = 0.05$). Higher Peclet numbers lead to more superheated fluid flowing in the mold resulting in higher heat fluxes. The effect of air gap decreases with increasing Peclet numbers as smaller air gap leads to lesser heat resistance. Increase in Pe number leads to downstream movement of the solidification front leading to smaller air gap width.

Smaller air gap width has negligible effect on the heat transfer. There exists a limiting value of Pe beyond which the air gap does not affect the solidification front location and the local heat flux. For the ranges of parameters investigated in the current study, this was observed for Pe = 2.5, $\theta_0 = 1.2$, $Bi_2 = 0.02$, $Bi_3 = 0.05$.

3. The superheat temperature strongly influences the position of the phase front but its effect on the slope was minimal. The metal should not be poured at higher superheat temperature because if the withdrawal speed is high as it leads to breakout. The heat flux increases with increase in superheat, as there is an overall increase in the domain temperature. The fractional heat extracted in the mold increases with increase in superheat as the air gap induces a significant heat resistance at lower superheat temperatures. The effect of air gap diminishes at higher superheat temperature as it leads to smaller air gap widths.
4. Mold cooling rate was significant in terms of the heat extraction efficiency. It was found that the heat extraction in the mold increases with increase of Bi_2 from 0.02 to 0.05 and then decreases at $Bi_2 = 0.1$. This was due the increased resistance offered by the air gap which increases in width with increase in mold cooling rate from $Bi_2 = 0.05$ to $Bi_2 = 0.1$. Thus, a critical value of Bi_2 exists for a given set of parameters, which gives the maximum heat extraction rate. The effect of mold cooling rate on the heat flux was similar. For the ranges of parameters investigated in the current study, this critical value of Bi_2 was equal to 0.05 for $\theta_0 = 1.2$, Pe = 2.0, 2.5, $Bi_3 = 0.05, 0.1, 0.15$.

5. The effect of post mold cooling rate was minor. Since most of the heat is extracted in the mold, the post mold cooling rate only affects the temperature distribution in the post mold region. The post mold cooling rate cannot used to control the shape and the location of the solidification front.

RECOMMENDATIONS:

Future work can be concentrated on the following aspects:

1. Different geometries and materials should be explored. Since alloys solidify over a range of temperature, the adequacy of the present method to the solidification of alloys can be studied. The code used in the present study Ansys (1999) also provides with porous media modeling which could be accurate for continuous casting of alloys.
2. The effect of turbulence on the interface modeling requires further research.
3. Lubricating mold flux can be included at the interface which could be modeled using porous media.
4. The effect of mold oscillation on the size of the air gap could be coupled with the interfacial air gap formation.
5. Mold distortion in three dimensions should be explored. This involves thermo-mechanical coupled modeling which is available in the present software [Ansys (1999)].

LIST OF REFERENCES

Ansys, *Commands Reference Manual*, Version 5.6, Eight Edition, SAS IP Inc., 1999.

Beck, J. V., Nonlinear estimation applied to the non-linear inverse heat conduction problem, *International Journal Heat Mass Transfer*, Vol. 13, pp. 703-716, 1970.

Berry, J. T., Piwonka, T. S., Heat transfer at the mold/metal interface in investment castings, *41st Annual Technical Meeting: Investment Casting Institute*, pp. 15:1-15:17, 1993.

Biloni, H., and Prates, M., *Metallurgical Transactions*, Variables affecting the nature of chill zone, Vol. 3A, pp. 1501-1510, 1972.

Brimacombe, J. K., Hawbolt, E. B., and Hernandez-Morales, B., Application of inverse techniques to determine heat-transfer coefficients in heat-treating operations, *Journal of Materials Engineering and Performance*, Vol. 1(6), pp. 763-772, 1992.

Brimacombe, J. K., Mahapatra, R. B., Paterson, E. A. Samarasekara, I. V., Walker, N., and Young, J. D., Mold behavior and its influence on quality in the continuous casting of steel slabs: Part I. Industrial trials, mold temperature measurements, and mathematical modeling, *Metallurgical Transactions B*, Vol. 22B, pp. 861-874, 1991 a.

Brimacombe, J. K., Mahapatra, R. B., Samarasekara, I. V., Mold behavior and its influence on quality in the continuous casting of steel slabs: Part II. Mold heat transfer, mold flux behavior, formation of oscillation marks, longitudinal off-corner depressions and subsurface cracks, *Metallurgical Transactions B*, Vol. 22B, pp. 875-888, 1991 b.

Brimacombe, J. K., Muojekwu, C. A., and Samarasekara, I. V., Heat transfer and microstructure during early stages of solidification, *Metallurgical and Materials Transactions B*, Vol. 26B, pp. 361-382, 1995.

Brimacombe, J. K., Samarasekara, I. V., Chandra, S., Bakshi, I. A., and Walker, B. N., On line monitoring of mould shell interaction during continuous casting of steel billets, *Ironmaking and Steelmaking*, Vol. 23, No. 6, pp. 512-521, 1996.

Choudary, S. K., and Mazumdar, D., Mathematical modeling of transport phenomena in continuous casting of steel, *ISIJ International*, Vol. 34, No. 7, pp. 584-592, 1994.

Choudary, S. K., and Mazumdar, D., and Ghosh, A., *ISIJ International*, Vol. 33, pp. 764, 1993.

Cubberly, W. H., *Metal Handbook, Properties and Selection: Non-ferrous alloys and pure metals*, 9th edition, ASM, Metal Park, Ohio, 1979.

References –Continued

Dalhuijsen, A. J., and Segal, A., Comparison of finite element techniques for solidification problems, *International Journal for Numerical Methods in Engineering*, Vol 23, pp. 1807-1829, 1986.

Droste, W., Engler, S., and Nishida, Y., The air gap formation process at the casting mold interface and the heat transfer mechanism through the gap, *Metallurgical Transactions B*, Vol. 17b, pp. 833-844, 1986.

Greif, D., Numerical study of conjugate heat transfer in a continuously moving metal during solidification, *M. S. Thesis, Montana State University, Bozeman, Montana*, 1998.

Ho, B., Characterization of Interfacial Heat Transfer in the Continuous Slab Casting Process, *MS Thesis, University of Illinois*, 1992.

Ho, K., and Pehlke, R. D., Metal-mold interfacial heat transfer, *Metallurgical Transactions B*, Vol. 16b, pp. 584-594, 1985

Ho, K., and Pehlke, R. D., Mechanisms of heat transfer at a metal-mold interface, *AFS Transactions*, Vol. 92, pp. 587-598, 1984.

Huang, C. H., Ozisik, M. N., and Sawaf, B., Conjugate gradient method for determining unknown contact conductance during metal casting, *International Journal of Heat Mass Transfer*, Vol. 35, No. 7, pp. 1779-1786, 1992 a.

Huang, X., Thomas, B.G., and Najjar, F. M., Modeling superheat removal during continuous casting of steel slabs, *Metallurgical Transactions B*, Vol 23b, pp. 339-356, 1992.

Irwing, W. R., *Journal of Iron and Steel Institute*, Vol. 205, pp. 271-277, 1967.

Isaac, J., Reddy, G. P., and Sharma, G. K., Variations of heat transfer coefficients during solidification of castings in metallic moulds, *The British Foundryman*, Vol. 78, pp. 465-468, 1985.

Jaluria, Y., Transport from continuously moving materials undergoing thermal processing, *Annual Review of Heat Transfer*, ed. C. L. Tien, Vol. 4, pp. 187-245, 1992.

Kang, B. H., and Jaluria, Y., Thermal modeling of continuous process, *Journal of Thermophysics and Heat Transfer*, Vol. 7, No. 1, pp. 139-147, 1992.

References - Continued

Kim, W. S., and Ozisik, M. N., Inverse problem of 1D solidification for determining air-gap resistance to heat flow during metal casting, *XXII International Centre of Heat and Mass Transfer, International Symposium on Manufacturing and Materials Processing, Dubrovnik, Yugoslavia*, pp. 1-18, August 1990.

Nakato, B. H., Ozawa, M., Kinoshita, K., Habu, Y., and Emi, T., Factors affecting the formation of shell and longitudinal cracks in mold during continuous casting of slabs, *Transactions ISIJ*, Vol. 24, pp. 957-965, 1984.

Namburu, R. R., and Tamma, K. R., Recent advances, trends and new perspectives via enthalpy-based finite element formulations for applications to solidification problems, *International Journal for Numerical Methods in Engineering*, Vol. 30, pp. 803-820, 1990.

Nishida, Y., and Matsubara, H., Effect of pressure on heat transfer at the metal mold castings interface, *The British Foundryman*, Vol. 69, pp. 274-278, 1976.

Patankar, S. V., and Spalding, D. B., *International journal of heat and mass transfer*, Vol. 15, pp. 1787, 1972

Royzman, S. E., Coefficient of friction between strand and mould during continuous casting: mathematical model, *Ironmaking and Steelmaking*, Vol. 24, No. 6, pp. 484-488, 1997

Sahai, V., Predicting interfacial contact conductance and gap formation of investment cast alloy 718, *Journal of Thermophysics and Heat Transfer*, Vol. 12, No. 4, pp. 562-566, October-December 1998.

Seyedein, S. H., and Hasan, M., A three-dimensional simulation of coupled turbulent flow and macroscopic solidification heat transfer for continuous slab casters, *International Journal of Heat and Mass Transfer*, Vol. 40, No. 18, pp. 4405-4423, 1997.

Samarasekera, I. V., and Brimacombe, J. K., The thermal field in continuous casting moulds, *Canadian Metallurgical Quarterly*, Vol. 18, pp. 251-266, 1979

Samarasekera, I. V., and Brimacombe, J. K., Thermal and mechanical behavior of continuous-casting billet moulds, *Continuous Casting*, BookCrafters, Inc., Chelsea, MI, Vol. 2, pp. 59-72, 1984.

Siegel, R., Two-region analysis of interface shape in continuous casting with superheated liquid, *Journal of Heat transfer*, Vol. 106, pp. 506-511, 1984.

References - Continued

Srinivasan, M. N., and Vanaparthy, N. M., Simulation of solidification in continuous cast steel using finite element method, *Thermal Processing of Materials: Thermo-Mechanics, Controls and Composites*, HTD-Vol. 289, pp. 131-138, 1994.

Thomas, B. G., Mathematical modeling of the continuous slab casting mold: A state of the art review, *Steelmaking Conference*, Proceedings of the Steelmaking conference, Iron and Steel Society, Warrendale, PA, pp. 105-118, 1991.

Thomas, B. G., Mika, L. J., and Najjar, M. F., Simulations of fluid flow inside a continuous slab-casting machine, *Metallurgical Transactions B*, Vol 21b, pp. 387-400, 1990

Thomas, B. G., Najjar, M. F., and Mika, L. J., The removal of superheat from continuous casting moulds, *F. Weinberg International Symposium on Solidification Processing, 29th CIM Conference, Hamilton*, pp. 131-145, 1990.

Thomas, B. G., and Ho B., Spreadsheet model of continuous casting, *Journal of Engineering for Industry*, Vol. 118, pp. 37-44, 1996.

Vanaparthy, N. M., and Srinivasan, M. N., Simulation of solidification in continuous cast steel using finite element method, *Thermal Processing of Materials*, Thermo-Mechanics, Controls and Composites, ASME, HTD-Vol. 289, pp. 131-138,1994.

Wolff, F., and Viskanta, R., Solidification of a pure metal at a vertical wall in presence of liquid superheat, *International Journal of Heat and Mass Transfer*, Vol 31., No. 8, pp. 1735-1744, 1988.